SUBSAMPLING GPS RECEIVER FRONT-END

A DISSERTATION
SUBMITTED TO THE DEPARTMENT OF ELECTRICAL
ENGINEERING
AND THE COMMITTEE ON GRADUATE STUDIES
OF STANFORD UNIVERSITY
IN PARTIAL FULFILLMENT OF THE REQUIREMENTS
FOR THE DEGREE OF
DOCTOR OF PHILOSOPHY

Carsten Barth
August 2011

Acknowledgement

and productive discussions with some of the best minds at Stanford. My appreciation goes out to Ben Mossawir, Charles Wang, Kelin Lee, Ben Cotts, and Andrew Tronson. I would further like to thank Shaolan Min and Helen Niu for their help on administrative tasks. I am honored to have worked with you and wish you all the best for your future endeavors, for you truly are great!

Thank you to David DeLorenzo from the Stanford GPS Research Laboratory for providing the Matlab GPS receiver back-end. My thanks go out to Shankar Ramakrishnan from the Stanford GPS Research Laboratory and to Dennis Akos from the University of Colorado in Boulder for several invaluable discussions.

Finally, for all of their patience and support, I would like to bestow my gratitude to my parents: Elisabeth and Gerold Barth. They always encouraged me to do my best, but never pressured me to be the best. I hope to bestow the same balance of work ethic and sensibility in my children. And finally, thank you to my beautiful wife, who always believed in my potential for academic excellence. She supported me with an unfaltering faithfulness and dedication.

CARSTEN BARTH

Stanford, California
January 30, 2007

Contents

List of Tables

List of Figures

Chapter 1

Introduction

1.1 Project Overview

The super-het receiver invented by Edwin Howard Armstrong in 1917 is likely the most popular wireless transceiver architecture and is used in most modern day Radio Frequency Integrated Circuits (RFICs). Recently, however, interest in direct RF sampling receivers as an alternative to the conventional super-het architecture has been growing. Replacement of much of the analog circuitry of the RF front-end with digital logic is driven by the desire for highly integrated, digitally scalable receivers with low power consumption. Direct RF sampling receivers have been demonstrated for GSM [*Staszewski et al.*, 2008], the 802.15.4 standard for 900 MHz [*DeVries and Mason*, 2008] and Software-Defined Radio for the 300 − 800 MHz band [*Ru et al.*, 2010]. The RF signal is either sampled at or above the rate of the carrier frequency [*Staszewski et al.*, 2008], [*Ru et al.*, 2010], or subsampled at a lower rate [*Yuce and Liu*, 2004], [*DeVries and Mason*, 2004, 2008], [*Pekau and Haslett*, 2005, 2007], [*Jakonis and Svensson*, 2003]. Subsampling architectures potentially exhibit several advantages over super-het architectures and other direct RF sampling architectures.

The complexity of subsampling architectures is significantly lower and RF to IF downconversion is achieved with less RF building blocks, potentially leading to significant power savings. Another significant benefit of the subsampling architecture is the capability to downconvert several distinct RF frequency bands with only one

sampling clock signal. Thus, subsampling architectures are particularly suited for Global Navigation Satellite System (GNSS) applications where downconversion of multiple frequency bands is required: With the advent of the new civilian GPS signal L2C and L5 in 2007 and 2009 [*Fontana*, 2001], [*Van Dierendonck*, 2001], respectively, and the anticipated onset of the new Galileo signal [*Issler et al.*, 2003], a receiver that can process multiple signals simultaneously without adding complexity, is highly desired. In fact, a subsampling GNSS receiver front-end made of discrete components was proposed and investigated by *Akos et al.*, [1999, 2003] and by *Prades and Rubio*, [2004]. A strategy for determining the optimum sampling frequency for such a GNSS receiver was found by *Psiaki et al.*, [2005]. As Psiaki showed, it is possible to down-convert the GPS frequencies L1, L2 and L5 and the Galileo signals simultaneously using a sampling frequency of 99.23 MHz.

Several comparative studies of the super-heterodyne and the subsampling architecture have been undertaken [*Tsui and Akos*, 1996], [*DeVries and Mason*, 2008], [*Psiaki et al.*, 2003]. It is evident that subsampling receivers, in theory, do not deliver subpar performance when compared to super-heterodyne receivers. Subsampling architectures, however, have in the past demonstrated high Noise Figures (NFs) due to the difficulty of building narrowband RF anti-aliasing filters. To achieve low NFs, subsampling architectures require good bandpass filtering before the digitization to prevent noise and interference aliasing. As explained by *Lee*, [1998, Chapter 19.3], it is difficult to build good bandpass filters in RFICs. In typical RF CMOS processes, on-chip inductors with high quality factors Q are hard to obtain, a critical prerequisite for a bandpass filter with sharp magnitude response. Commonly, a technique called Q-enhancement is applied to the lossy spiral inductors. By creating a negative parallel resistance, the loss of the inductors is partially canceled and the effective Q is increased, leading to a so-called Q-enhanced resonator [*Kuhn et al.*, 1998], [*Ahmed et al.*, 2003], [*Wiser*, 2008]. It was shown by *Wiser*, [2008] that Q-enhancement can be successfully implemented to achieve even multi-stage bandpass filters in RF CMOS with arbitrary filter response.

Using Q-enhanced bandpass filters, there have been some successful attempts to develop subsampling architectures on-chip, and progress has been made to reduce the

NF of subsampling architectures in RFICs. *DeVries and Mason*, [2008] reported a NF of 8 dB using RF filters with highly Q-enhanced LC resonators and theoretically showed that subsampling architectures can achieve similar performance as conventional receivers. *Pekau and Haslett*, [2005, 2007] achieved a simulated NF of 8 dB. Such NFs might be acceptable in many applications; however, a GNSS receiver typically requires a NF of less than 5 dB [*Cheng et al.*, 2009], [*Liscidini et al.*, 2006], [*Gramegna*, 2006], [*Ko*, 2005].

In this dissertation, a low noise GPS subsampling receiver is demonstrated for the GPS L1 signal. The power consumption and the NF is comparable to state-of-the-art heterodyne GPS receivers. The front-end was fabricated in a 130 nm BiCMOS process from National Semiconductor and occupies 1x2 mm^2. The total power consumption is 9 mW, the supply voltage is 1.2 V. The NF before subsampling is 3.2 dB at the filter output. After subsampling, the total receiver NF is 3.8 dB making it suitable for GPS. The NF penalty due to subsampling is less than 1 dB. The dissertation is rounded off by the theoretical investigation and derivation of the NF of a subsampling architecture with bandpass filter.

1.2 Dissertation Organization

Chapter 2 presents an introduction to the various GPS segments and the GPS signal structure. A typical GPS receiver front-end design based on the super-heterodyne architecture is illustrated and the design challenges are discussed. Relevant figures of merit for a GPS receiver such as NF and 1 dB compression point are defined and derived in Chapter 2.

In Chapter 3, the proposed subsampling architecture is presented. The theoretical NF of a subsampling architecture with bandpass filter is derived and the fundamental differences to the super-heterodyne architecture are highlighted. Moreover, the effects of sampling clock jitter on the receiver NF are investigated. The discussion is continued with the effects of quantization noise on the receiver performance. A study of the linearity of the proposed subsampling architecture rounds off the discussion in Chapter 3.

Chapter 4 describes the circuit implementation of the receiver. The low noise amplifier (LNA) is discussed and the design trade-offs are briefly reviewed. A detailed study of the RF filter, the sample and hold (S/H) stage, the variable gain amplifier (VGA) and the other RF building blocks is presented on a transistor level basis. Finally, at the end of Chapter 4, the layout of the IC is discussed.

In Chapter 5, measurement results of the front-end are presented. A total receiver NF of less than 3.8 dB is achieved, comparable to the NFs of many super-heterodyne GPS receiver front-ends.

Finally, in Chapter 6, a conclusion is drawn by comparing and interpreting measurement results. A section about future work still necessary to make the subsampling receiver a viable and robust solution rounds off the dissertation.

1.3 Contributions

The primary contribution of this thesis is:

- Design of an integrated subsampling GPS receiver front-end for the GPS L1 signal in a 130nm BiCMOS process. The receiver achieves a noise figure of less that 3.8 dB, the lowest ever recorded noise figure of a subsampling based receiver.

Other contributions made during the design of the GPS receiver front-end are:

- Development of a new on-chip double notch RF filter architecture, serving as a noise and interference rejection filter in the GPS receiver front-end.

- Extension of the Friis Formula for noise figure calculations to include noise aliasing and noise folding in cascaded RF systems.

- Investigation of the oscillation stability of various subsampling receiver architectures.

Chapter 2

The Global Positioning System

GPS is comprised of the User Segment, the Space Segment and the Operational Control Segment as explained by *Misra and Enge* [2006, pp. 29-66, Chapter 2]. The Space Segment consists of the satellites that transmit the ranging and navigation signals. The ranging and navigation signals are received by the User Segment which determines position and time of the user. The Space Segment is constantly monitored by the Operational Control Segment which is comprised of several monitoring stations distributed around the globe. The Operational Control Segment is operated by the U.S. Department of Defense which ensures proper operation of the GPS. The U.S. Department of Defense, for instance, performs minor adjustments to the location of the satellites and updates the ranging and navigation signals of the satellites.

This chapter presents a review of the Global Positioning System and its various segments. It is intended to give the necessary background for the following chapters, and primarily a review of contemporary GPS literature such as [*Misra and Enge*, 2006] and [*Parkinson and Spilker*, 1996]. In the first section of this chapter, a detailed description of the GPS Space Segment and Operational Control Segment (OCS) is provided. In the next section, the GPS signal structure is investigated and analyzed in detail. Then, the relevant and important figures of merit of a GPS receiver are discussed; namely the 1 dB compression point, the signal-to-noise ratio (SNR) and the NF. The formula for the NF of a cascaded RF system — the well-know Friis equation — is derived during the discussion of the NF. Finally, in the last section,
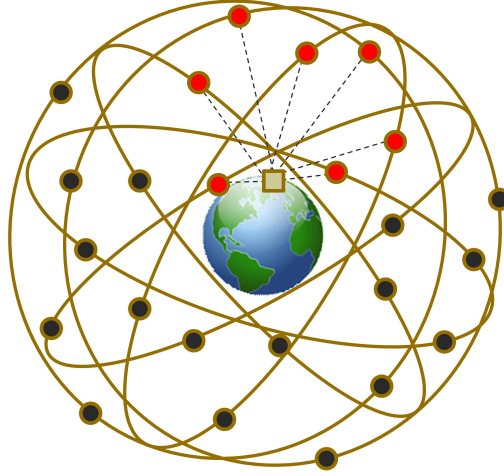
Figure 2.1: GPS Space Segment: 24 satellites in 26,550 km orbits provide the ranging signal and the navigation message to the GPS User Segment.

the design and implementation challenges of a super-heterodyne based GPS receiver front-end are presented.

2.1 GPS Space and Operational Control Segment

The Space Segment is illustrated in Figure 2.1 and consists of a configuration of more than 24 satellites orbiting the Earth at a speed of 4 km/sec in six different circular orbits with 26,600 km radius [*Misra and Enge*, 2006, pp. 33-34, Chapter 2]. The satellites are unevenly distributed in each one of the six orbital planes. The orbits are inclined at an angle of 55° relative to the equatorial plane. In GPS terminology, the satellites are referred to as space vehicles and are distinguished by a two character code. Each satellite transmits a navigation signal with a unique satellite specific ranging code and the navigation message. From the ranging code and the navigation message, the user can determine his distance to each one of the satellites. By making several range measurements to distinct satellites the user can ultimately calculate his position very precisely. At least four range measurements are necessary to accurately determine position. Under typical conditions, the user has 5 to 8 satellites in view as depicted in Figure 2.1.
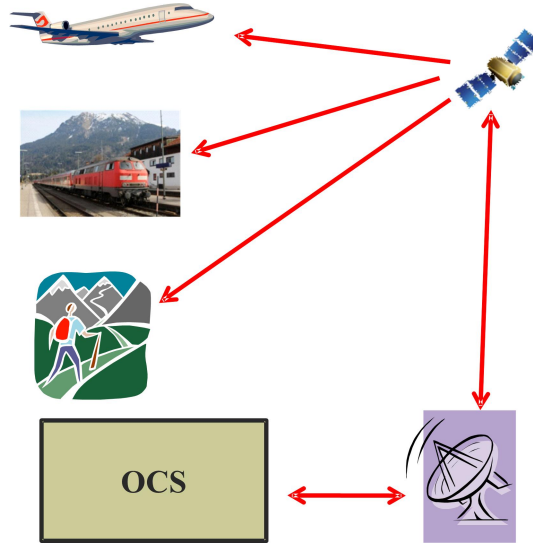
Figure 2.2: The GPS Operational Control Segment (OCS) continuously monitors the Space Segment.

The Operational Control Segment (OCS) is illustrated in Figure 2.2. The OCS is comprised of several control stations operated by the U.S. Department of Defense, including the Master Control Station (MCS) located at the Schriever Air Force base in Colorado. Other monitoring stations are located in Hawaii, Cape Canaveral, Ascension Island, Diego Garcia and Kwajalein [*Misra and Enge*, 2006, p. 35, Chapter 2]. Also, the National Geospatial-Intelligence Agency (NGA) controls a globally distributed network of several monitoring stations. Communication between the Space Segment and the OCS is performed via ground antennas. The location of the control stations and the location of the ground antennas can be determined from Figure 2.3. The OCS monitors and corrects the satellite orbits by performing small satellite maneuvers; it also updates the GPS time and navigation message and performs other vital functions necessary for the proper operation of the GPS.

2.2 GPS Signal Structure

The GPS satellites provide at least two different signals, the GPS L1 signal and the GPS L2 signal. The GPS satellites continuously transmit the GPS L1 signal with a

Figure 2.3: Location of the OCS monitor stations, [*Russo*, 2008].

carrier frequency of 1575.42 MHz and the GPS L2 signal with a carrier frequency of 1227.60 MHz. Additional signals and satellites were added in recent years to further enhance the capabilities of GPS. A new civilian signal, the GPS L2C, was added to the GPS L2 carrier with the launch of new satellites in 2005. Also, starting in 2007, satellites were launched broadcasting the new GPS L5 signal at 1176.45 MHz in a protected frequency band for so-called safety-of-life applications. A complete discussion of the GPS signal structure is given by *Parkinson et al.*, [1996, Chapter 3] and *Misra and Enge*, [2006, pp. 37-43, Chapter 2, pp. 71-77, Chapter 9] for the interested reader.

The discussion in this text is focused on the ubiquitous GPS L1 signal for civil users which has found its way into numerous applications. The GPS L1 signal is described in [*IS-GPS-200D*, 2004] and consists of three components [*Misra and Enge*, 2006, pp. 37-43, Chapter 2]: (i) the RF carrier located at the carrier frequency of 1575.42 MHz, (ii) the satellite specific ranging codes — also referred to as pseudo random noise (PRN) codes — which are different for every satellite and which are uncorrelated with each
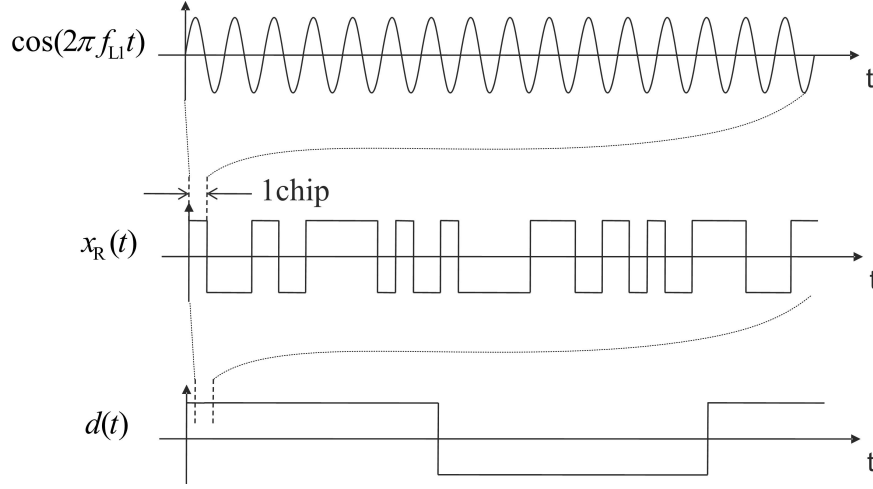
Figure 2.4: GPS L1 signal: RF carrier signal, PRN code $x_R(t)$ and the navigation message $d(t)$ — not drawn to scale.

other, (iii) the GPS L1 carrier that is modulated by two distinct ranging codes; one that is accessible by civil users and one that is accessible by authorized military users, only. The ranging codes for civil users are referred to as C/A (coarse/acquisition) codes and for military users as P(Y) (precision) codes. Each C/A code is comprised of a unique sequence of 1023 bits — also referred to as chips in GPS terminology — and repeated every 1 ms. Hence the bit rate of the C/A codes, the so-called chipping rate, is 1.023 MHz. The P(Y) codes possess a significantly longer bit sequence and duration than the C/A codes which allows for a higher ranging precision. Due to their restricted access, the P(Y) codes are not part of the discussion in this text. The C/A ranging codes allow to make precise measurements of the distance or range to each one of the satellites in view. The last component modulated on the L1 carrier is the navigation message which is transmitted at 50 bits per second, hence every bit has a duration of 20 ms. The navigation message contains critical satellite parameters such as satellite location and velocity, information about the bias of the satellite clock and other crucial parameters. Ultimately, the GPS receiver calculates its position from the measured range to the satellites and the extracted navigation message.

The RF carrier, the PRN code and the navigation message are illustrated in
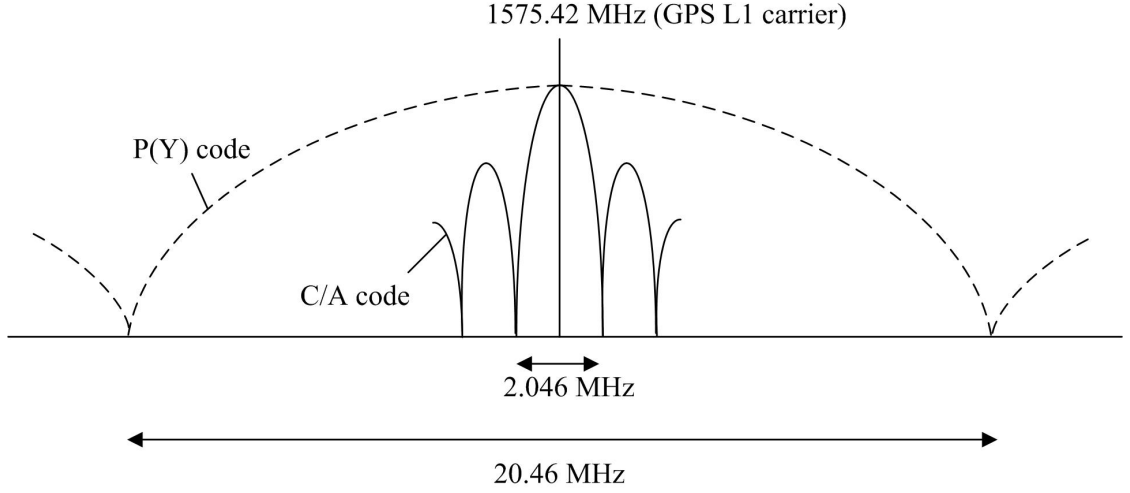
Figure 2.5: GPS L1 signal spectrum. P(Y) code spectrum (dashed line) and C/A code spectrum (solid line), from [*Misra and Enge*, 2006, p. 41, Chapter 2].

Figure 2.4. The GPS L1 signal with the carrier frequency f_{L1} can be modeled by

$$s(t) = \sqrt{2P_S}\, x_R(t)\; d(t)\;\; \cos(2\pi f_{L1} t) \tag{2.1}$$

where P_S is the signal power, $d(t)$ is the navigation message and $x_R(t)$ the ranging code. The minimum signal power measured on ground in a location with unobstructed view to a GPS satellite is -130 dBm. Often the actual received signal power P_S is several dB higher and dependent on the satellite constellation, atmospheric conditions and other factors. On the other hand, it is easy to lose 10 dB to 20 dB of signal power in locations with obstructed view to the satellites such as in urban canyons or indoor environments.

Modulation of the L1 carrier with the 1023 bit long C/A code and the much longer P(Y) code causes the signal spectrum to spread out around the carrier frequency. Hence, the ranging codes are sometimes also called spread-spectrum codes. The signal spectrum of the L1 carrier (modulated with the P(Y) and C/A code) is displayed Figure 2.5. The main lobe of the C/A code has a bandwidth of 2.046 MHz; the main lobe of the P(Y) code has a bandwidth of 20.46 MHz. Spreading has no influence on the transmitted signal power P_S which remains still at approximately -130 dBm.

Thus, spreading causes the power spectral density to drop.

In the following, the cross- and autocorrelation properties of the C/A code sequences transmitted by the different satellites are presented. Assume $x_{\mathrm{R}}^{k}(q)$ is the C/A code transmitted by the k-th satellite and q is the q-th chip of the 1023 bit long C/A code sequence. Then, the autocorrelation and crosscorrelation function of $x_{\mathrm{R}}^{k}(q)$ is given by [*Misra and Enge*, 2006, pp. 40-41, Chapter 2]

$$\sum_{i=0}^{1022} x_{\mathrm{R}}^{k}(i)x_{\mathrm{R}}^{l}(i+n) \simeq 0 \quad for\ all\ n,\ \ if\ k \neq l \tag{2.2}$$

$$\sum_{i=0}^{1022} x_{\mathrm{R}}^{k}(i)x_{\mathrm{R}}^{k}(i+n) \simeq 0 \quad for\ n > 0 \tag{2.3}$$

Since the sequence repeats after 1023 bits, it is clear that $x_{\mathrm{R}}^{k}(q) = x_{\mathrm{R}}^{k}(q + 1023)$. From the crosscorrelation function (2.2) it can be concluded that the C/A codes from different satellites are approximately orthogonal to each other. On the other hand, the autocorrelation function (2.3) of any C/A code is only zero for non-zero time shift, a property of the C/A codes which is illustrated in Figure 2.6. The GPS receiver back-end creates a replica of the GPS C/A code and correlates it with the received signal from the antenna. Back-end receivers rely on the crosscorrelation properties of the C/A codes from different satellites to separate the satellites in view. The autocorrelation properties allow to precisely align and synchronize the replica signal with received signal from the antenna, a property required for making precise range measurements.

2.3 GPS Receivers

2.3.1 Thermal Noise, Signal-to-Noise Ratio, C/N_0 Ratio

Thermal noise, the signal-to-noise ratio SNR and the carrier-to-noisefloor ratio C/N_0 are discussed in the following section. The term noise can be defined broadly to include every undesired signal component present in the signal spectrum. It certainly
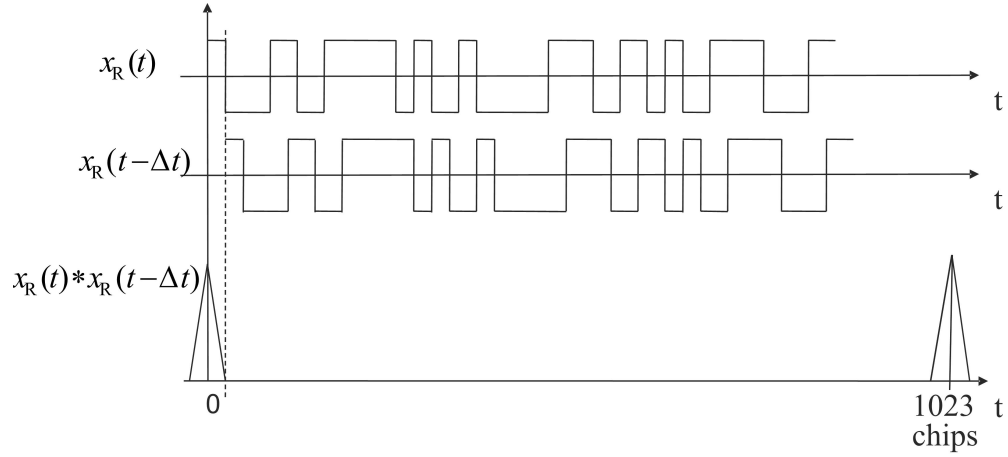
Figure 2.6: Autocorrelation properties of the C/A code — not drawn to scale.

includes random noise from thermal sources — also referred to as Johnson noise — which was first reported by *Johnson*, [1928]. Another important source of random noise is shot noise originating from the granular nature of electronic charge. Shot noise was first described by *Schottky*, [1918]. Other sources of random noise include Flicker noise and burst noise which are well-described by *Lee*, [1998]. Noise from deterministic sources include quantization noise introduced by analog-to-digital (A/D) conversion or supply and ground bounce induced by supply current transients, for instance, from switching digital gates. Due to the wide range of different types of noise, the derivation of the NF in this chapter is limited to noise from thermal sources, the most important type of noise for GPS. The interested reader is referred to [*Lee*, 1998] for an extended discussion of various sources of noise in RF systems.

The available thermal noise power generated by the source load is proportional to the absolute temperature T and given by [*Gonzalez*, 1997, p.295, Chapter 4]

$$P_{\text{Noise}} = kTB \tag{2.4}$$

where k is the Boltzmann's constant and B the bandwidth over which the measurement is made. The SNR, one of the most frequently used concepts in RF circuit design, is essentially a measure by how much the signal is corrupted by noise. The
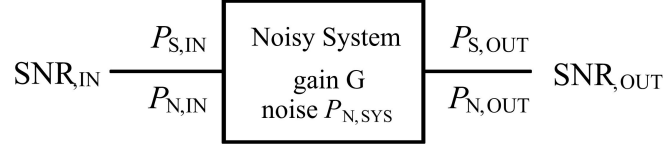
Figure 2.7: Noisy RF system

SNR is defined as the ratio of signal power P_Signal to noise power P_Noise

$$\text{SNR} = \frac{P_\text{Signal}}{P_\text{Noise}} \tag{2.5}$$

The SNR is commonly expressed in decibels. The higher the SNR, the less the signal is corrupted by undesired noise components. Often, for GPS receivers the C/N_0 ratio is stated instead of the SNR. The C/N_0 ratio is closely related to the SNR and is defined as the ratio of the signal power $C = P_\text{Signal}$ (in Watts) to the noise power density N_0 (in Watts/Hertz). The relationship between the SNR and the C/N_0 ratio is straightforward. Assuming the bandwidth of interest is given by B, the SNR and the C/N_0 ratio are related by:

$$\text{SNR} = \frac{C}{BN_0} \tag{2.6}$$

2.3.2 Noise Factor, Noise Figure

The thermal noise factor measures the degradation of SNR from the input of a noisy RF system to the output. As depicted in Figure 2.7, a signal with available power $P_\text{S,IN}$ applied to the input of the RF system produces a signal at its output with available power $P_\text{S,OUT}$. The noise power at the input and output of the system are given by $P_\text{N,IN}$ and $P_\text{N,OUT}$, respectively. The noise factor F is defined as the ratio of the input signal-to-noise ratio SNR_IN to the output signal-to-noise ratio SNR_OUT

$$F = \frac{\text{SNR}_\text{IN}}{\text{SNR}_\text{OUT}} \tag{2.7}$$

The larger the SNR degradation from the input to the output, the larger the noise factor F. The thermal signal-to-noise ratios SNR_IN and SNR_OUT are measured at the

input and output of the RF system under the condition that the input of the RF system is connected to a source at a temperature T_0 of 290 K. A more generalized but perfectly valid definition for the noise factor F is given by

$$F = \frac{\text{total output noise power}}{\text{output noise power due to the source (at a temperature of 290K)}} \qquad (2.8)$$

The available thermal noise power from the source load is given by

$$P_{\text{N,IN}} = kT_0B \qquad (2.9)$$

The available noise power at the output of the RF system with available power gain G is

$$P_{\text{N,OUT}} = P_{\text{N,IN}}G + P_{\text{N,SYS}} \qquad (2.10)$$

$P_{\text{N,SYS}}$ is the system noise power generated by the RF system itself and is added to the amplified thermal noise power from the source. $P_{\text{N,SYS}}$ can be related to the noise factor F in the following fashion: With the available signal power at the input of the RF system $P_{\text{S,IN}}$ and the available signal power at the output $P_{\text{S,OUT}} = GP_{\text{S,IN}}$ the noise factor F can be written as

$$F = \frac{\text{SNR}_{\text{IN}}}{\text{SNR}_{\text{OUT}}} = \frac{\dfrac{P_{\text{S,IN}}}{P_{\text{N,IN}}}}{\dfrac{P_{\text{S,OUT}}}{P_{\text{N,OUT}}}} = \frac{P_{\text{N,IN}}G + P_{\text{N,SYS}}}{P_{\text{N,IN}}G} = 1 + \frac{P_{\text{N,SYS}}}{kT_0BG} \qquad (2.11)$$

Note, that exactly the term $P_{\text{N,SYS}}$ causes the degradation of SNR from the input to the output of the RF system.

Noise temperature is an alternative way to express the noise contribution of any RF building block. The noise temperature T_e of the system is defined as [*Misra and Enge*, 2006, p. 403, Chapter 10]

$$T_e = \frac{P_{\text{N,SYS}}}{kBG} \qquad (2.12)$$

The relationship between the noise factor and the noise temperature is readily found

from (2.11) and (2.12) and is given by

$$F = 1 + \frac{T_e}{T_0} \tag{2.13}$$

If the RF system did not produce any thermal noise ($P_{N,SYS} = 0$) the effective noise temperature vanished and the noise factor became one ($F = 1$). Most practical RF systems, however, produce noise.

The noise figure NF is related to the noise factor F by

$$F = 10\log\frac{SNR_{IN}}{SNR_{OUT}} \tag{2.14}$$

Hence, the NF is the noise factor F in dB. The NF is one of the most important figures of merit of a GPS receiver. It can be shown that it directly affects the ranging precision of the receiver. In fact, the ranging precision of a GPS receiver is given by [*Misra and Enge*, 2006, p. 416]

$$\sigma = cT_C\sqrt{\frac{1}{4TC/N_0}} \tag{2.15}$$

where c is the speed of light, T_C the average chip duration ($T_C = 1\mu$sec for the C/A code) and T the averaging time of the correlator used in the receiver back-end. The carrier-to-noise ratio C/N_0 measured by the receiver back-end is closely related to SNR as explained in Section 2.3.1.

The importance of achieving a low NF in the GPS receiver front-end can be understood by calculating the signal power and the noise power at the receiver input. The received noise power within the 2 MHz bandwidth of the C/A code (the main lobe of the C/A code) is approximately -111 dBm. The GPS signal power received by the antenna is about -130 dBm which is 20 dB below the noise floor. The signal experiences a processing gain from noise averaging during the correlation process in the receiver back-end which brings it above the noise floor for detection. Assuming a chipping rate of 1.023 MHz for the C/A code and a symbol rate of 50 Hz for the navigation message, the processing gain is 10 log(1023000/50) = 43 dB [*Lee*, 1998,
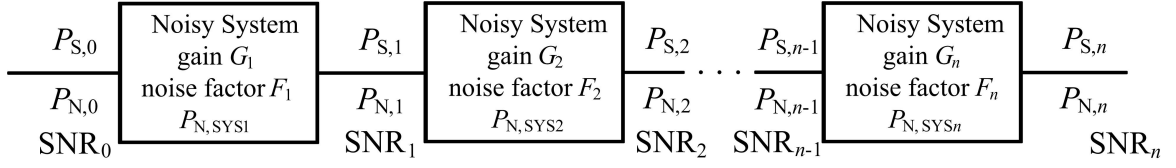
Figure 2.8: Cascaded noisy RF system: A cascade of several noisy RF building blocks with individual noise factors and gains.

Chapter 19]. Thus, the SNR is about 23 dB after processing and is further degraded by the NF of the receiver front-end. Assuming that 10 dB of SNR is required for detection, it is all too easy to understand why commercial GPS receivers have single-digit NFs.

2.3.3   Noise Figure of a Cascaded RF System – the Friis Equation

In this section the equation for the total system NF of the cascaded RF system depicted in Figure 2.8 is derived. The cascaded system consists of n stages with individual gains $G_1,\ldots,G_n$ and individual noise factors $F_1,\ldots,F_n$. The available signal power at the input of the cascaded system is $P_{S,0}$ and the noise power $P_{N,0} = kT_0B$. On the other hand, the available signal power at the output of the cascaded system is $P_{S,n}$ and the noise power $P_{N,n}$. Using the generalized definition from (2.8), the noise factor F of the cascaded system is given by

$$F = \frac{P_{N,n}}{G_1G_2..G_nkT_0B} \tag{2.16}$$

The available signal power at the output of stage q is $P_{S,q}$ and the available noise power is $P_{N,q}$ with a signal-to-noise ratio of SNR_q. Stage q internally generates the noise power $P_{N,\text{SYS}q}$ that is added to its output. The output noise power $P_{N,1}$ of stage 1 is given by

$$P_{N,1} = P_{N,0}G_1 + P_{N,\text{SYS1}} = kT_0BG_1(1 + (F_1 - 1)) \tag{2.17}$$

where use of equation (2.11) has been made. Similarly, the output noise power $P_{N,2}$ of stage 2 is given by

$$P_{N,2} = P_{N,1}G_2 + P_{N,SYS2} = kT_0BG_1G_2\left(1 + (F_1 - 1) + \frac{1}{G_1}(F_2 - 1)\right) \qquad (2.18)$$

The output noise power $P_{N,n}$ is thus given by

$$P_{N,n} = P_{N,n-1}G_n + P_{N,SYSn} = kT_0BG_1G_2\cdots G_n$$

$$\times \left(1 + (F_1 - 1) + \frac{1}{G_1}(F_2 - 1) + \cdots + \frac{1}{G_1G_2\cdots G_{n-1}}(F_n - 1)\right)$$

$$(2.19)$$

Combining (2.16) and (2.19) the total cascaded spot noise factor is given by

$$F = F_1 + \frac{1}{G_1}(F_2 - 1) + \cdots + \frac{1}{G_1G_2\cdots G_{n-1}}(F_n - 1) \qquad (2.20)$$

which was derived by *Friis*, [1944]. Hence, the equation is commonly referred to as *Friis equation*. Equation (2.20) highlights the well-know result that the noise factor of the first stage in a cascaded RF system fully contributes to the overall noise factor of the system while the noise factors of the subsequent stages are divided by the gain of the preceding stages and have a much smaller impact on the total system noise factor. To achieve a low overall noise factor or NF, it is very important to use an amplifier with a low NF and a high gain as first stage.

2.3.4 1 dB Compression Point

Another important figure of merit for the linearity of a GPS receiver is the 1 dB compression point. At low RF input power levels the RF system behaves linearly and the RF output power is equal to the small signal power gain times the RF input power. At higher RF input power levels, higher order harmonics appear in the signal spectrum effectively causing a reduction of power gain. The 1 dB compression point of a RF building block is defined as the RF input power where the actual measured power gain is 1 dB smaller than the small signal power gain. The 1 dB compression
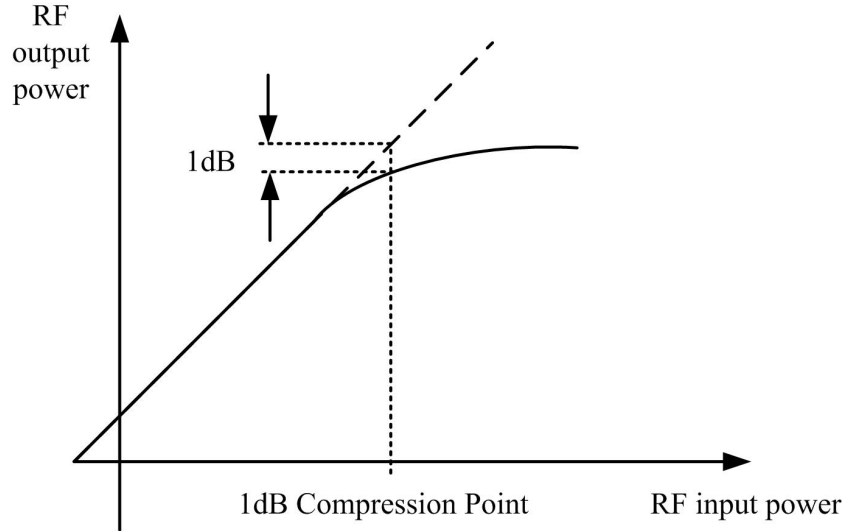
Figure 2.9: The 1 dB compression point is the point where the actual measured power gain is 1 dB smaller than the small signal power gain.

point is illustrated in Figure 2.9. A good discussion of the 1 dB compression point can be found in [*Lee*, 1998].

Receiver linearity is an important figure of merit for a GPS receiver. Out-of-band interference can saturate the LNA and create spurious harmonic mixing products which ultimately lead to jamming of the receiver. Therefore, the 1 dB compression point of the receiver has to be sufficiently high to accommodate these signals while remaining in the linear region. Out-of-band interference is filtered out by the IF filter if the receiver is not saturated. While the receiver can be made more resilient against out-of-band interference by increasing the linearity of the front-end, other measures need to be taken in order to improve the jamming performance against in-band interference. In-band interference is passed right through the IF filter and can jam the receiver back-end. Jamming sometimes occurs at signal level as low as -110 dBm. Higher bit quantization improves the resilience of the receiver against in-band interference. It is worth mentioning that the closely related third order input referred intercept point (IIP3) is often used as measure of linearity for GPS receivers. The IIP3 is typically about 10 dB above the 1 dB compression point.

2.3.5 Receiver Overview

The GPS receiver can be split up into an analog receiver front-end and a digital receiver back-end: The GPS receiver front-end captures the RF carrier signal via its antenna and downconverts the signal to a much lower IF. The GPS receiver front-end consists of the RF and IF section of the receiver and includes the RF bandpass filter, the LNA, the downconverter, the IF bandpass filter and the IF amplifier.

The GPS receiver back-end performs the digital signal processing. The back-end extracts the navigation message and determines the range to the satellites in view from which it calculates the position of the user. It performs an acquisition step to find an estimate for the time of arrival and the doppler shift of the received signal. After signal acquisition, the back-end switches into signal tracking mode during which more accurate estimates of the time of arrival and doppler shift are obtained. The correct estimation of both quantities is necessary to accurately determine the range to the various satellites in view. Also, during signal tracking mode, the 50 Hz and the navigation message is extracted. The precise position of the user is determined from the range measurements and the information obtained from the navigation message. The digital receiver back-end is beyond the scope of this dissertation. The interested reader is referred to [*Misra and Enge*, 2006, Chapter 11-13] and [Parkinson et al., 1996, Chapter 8] for a more detailed discussion of the digital back-end.

2.3.6 Superheterodyne Receivers

The RF front-end of a typical GPS receiver is typically based on the well-know heterodyne architecture [*Cheng et al.*, 2009], [*Liscidini et al.*, 2006], [*Gramegna*, 2006], [*Ko*, 2005]. A picture of the architecture is depicted in Figure 2.10. The RF signal is captured by the antenna and low-noise amplified by the LNA. The NF and the gain of the LNA approximately set the total NF of the GPS receiver. It is thus important to design a LNA with a low NF and a large gain to overcome the NF of the subsequent RF mixer. After passing the LNA, the RF signal is downconverted to IF by the mixer. A precise clock signal generated by the local oscillator is multiplied with the incoming GPS L1 input signal. Assuming the frequency of the local oscillator is
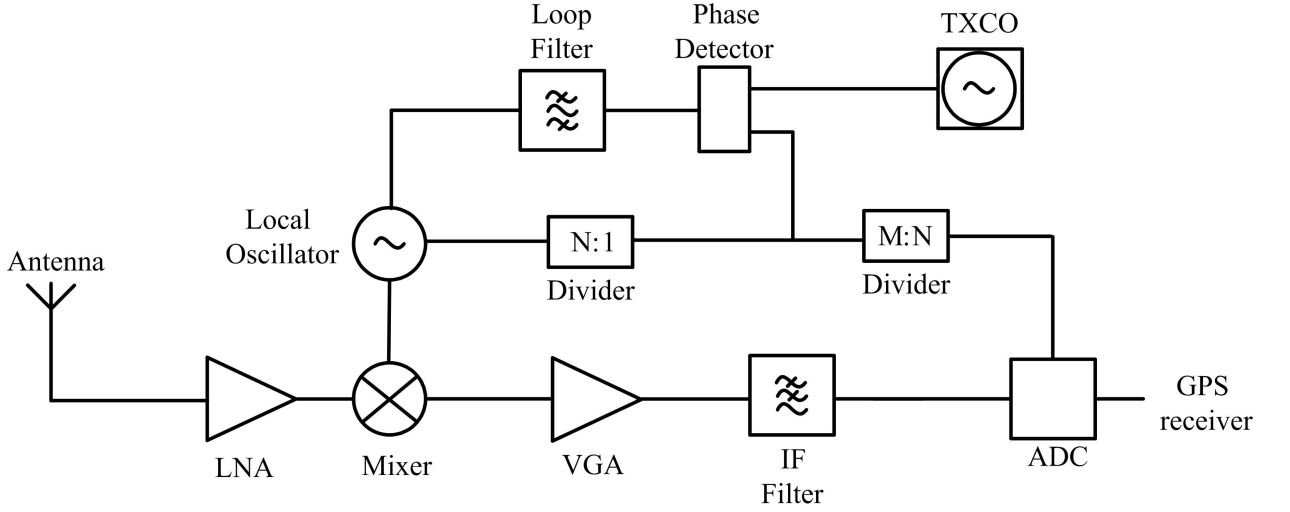
Figure 2.10: The super-heterodyne based GPS receiver front-end relies on classical mixing to downconvert the RF signal. The super-het requires a PLL to synchronize local oscillator with the external crystal oscillator.

f_{LO}, the output signal of the RF mixer is given by

$$
\begin{aligned}
s_{\text{IF}}(t) &= \sqrt{2P_{\text{S}}}\, x_{\text{R}}(t)\, d(t)\,\cos(2\pi f_{\text{L1}}t)\,\cos(2\pi f_{\text{LO}}t) \\
&= \sqrt{2P_{\text{S}}}\, x_{\text{R}}(t)\, d(t)\,(\cos(2\pi(f_{\text{L1}} + f_{\text{LO}})t) + \cos(2\pi(f_{\text{L1}} - f_{\text{LO}})t))
\end{aligned}
\tag{2.21}
$$

and has two frequency components. The higher frequency component $f_{\text{L1}} + f_{\text{LO}}$, which is filtered out by the subsequent IF filter and the lower frequency component $f_{\text{L1}} - f_{\text{LO}}$, which is the desired IF. To achieve a low IF, the local oscillator frequency needs to be close to the incoming L1 frequency. It is interesting to note from (2.21) that both the signal located at the frequency f_{L1} and the signal located at the image frequency $2f_{\text{LO}} - f_{\text{L1}}$ are aliased down to the same IF. Hence, any interfering signal located at the image frequency can potentially corrupt the signal and a preselector filter is sometimes added to filter out the image frequency. The image frequency problem can be partially mitigated by canceling the undesired image during the mixing process. The Weaver architecture is one of the possible candidates for image rejection that has been proposed in literature [*Weaver*, 1956]. The image frequency also plays an important role for NF calculations: Noise located at the RF frequency and its image

frequency is downconverted to IF. This effect increases the NF of a RF mixer by 3 dB.

After downconversion, a VGA amplifies the IF signal to meet the input requirements of the analog-to-digital converter (ADC). The gain of the VGA is often dynamically adjusted to account for signal strength variations resulting from atmospheric conditions or change of the user environment. The IF filter is usually of higher order, serving as image rejection filter and anti-aliasing filter. The number of ADC bits not only determine the jamming performance of the receiver but also the amount of quantization noise. For example, a 1-bit ADC introduces about 2 dB of quantization SNR loss that needs to be taken into account when calculating the total receiver NF. The quantization loss can be added to the cascaded NF of the LNA, the mixer, the VGA and the IF filter. In general, the quantization loss depends on the number of quantization bits as well as the pre-sampling bandwidth (see Section 3.5 for further analysis).

The local oscillator needs to be synchronized with an off-chip crystal oscillator to achieve the clock precision necessary for GPS. Both frequency stability as well as superior phase noise performance are important. Any frequency offset of the local oscillator ends up as frequency offset of the IF, conceptually similar to the Doppler shift. To ensure rapid signal acquisition, this frequency offset should not be too large. Hence, the 1.57542 GHz L1 carrier needs to be relatively stable over time with respect to frequency variations. Another concern is phase noise which directly degrades receiver NF as it will be shown in Section 3.3. A good external oscillator such as a temperature compensated crystal oscillator (TCXO) provides the necessary frequency stability and phase noise performance. A phase-locked loop (PLL) consisting of a divider structure, a phase detector and a loop filter synchronizes the TXCO with the local oscillator. Often, for GPS a 16.368 MHz crystal is used whose frequency is 16 times the chipping rate of 1.023 MHz. Also note that the RF carrier is exactly 154 times the chipping rate.

Chapter 3

GPS Subsampling Receiver Architecture

Subsampling or bandpass sampling architectures sample the incoming RF signal at a frequency close to the much lower frequency of the information content change rather than the carrier frequency. Subsampling architectures downconvert the RF signal to IF by aliasing, which is in contrast with the super-heterodyne architecture where downconversion is achieved through mixing rather than through sampling. It is not surprising that relevant RF figures of merit such as the receiver NF are computed in a crucially different way for a subsampling architecture.

This chapter describes the subsampling architecture for GPS in more detail and derives the relevant RF figures of merit. The thermal NF of the subsampling receiver is calculated taking into account in-band and aliased out-of-band thermal noise from the LNA, the RF filter and the S/H stage. The analysis combines and extends the derivations from *Pekau and Haslett*, [2006] and *DeVries and Mason*, [2008]. Using approximations, a simplified expression for the thermal NF of a subsampling receiver is found. The section is followed by a brief discussion on Q-enhanced resonator filters which are used as anti-aliasing filters. The NF of the subsampling GPS receiver front-end is not only affected by in-band thermal noise and aliased out-of-band noise. Other sources of noise ranging from the jitter of the sampling clock (also known as aperture noise) to the quantization noise introduced during A/D conversion are investigated
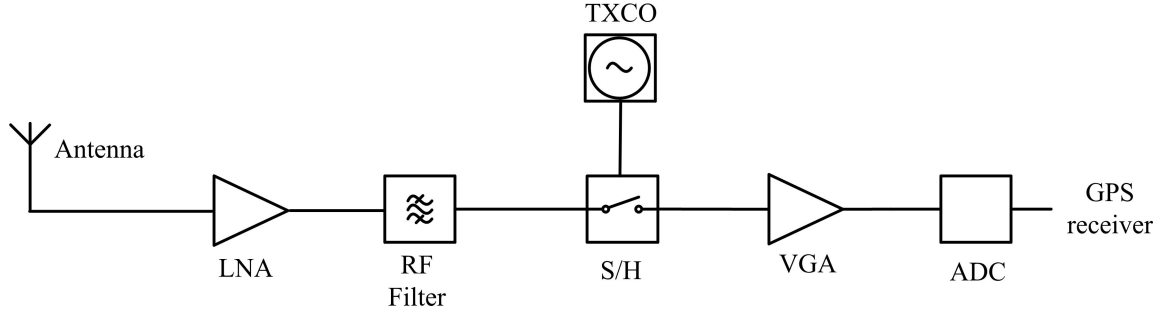
Figure 3.1: Subsampling GPS receiver architecture comprised of a LNA, RF filter, S/H stage, VGA and ADC. The subsampling receiver downconverts the RF signal to IF by sampling rather than mixing. The clock signal is directly derived from a crystal oscillator.

in the following sections. It is shown that subsampling architectures are suited for GPS and GNSS application where ultra-low NFs are of uttermost importance. An additional section on interference rounds off the discussion in this chapter.

3.1 Subsampling Architectures

The subsampling architecture proposed for the GPS receiver front-end is shown in Figure 3.1 and is comprised of a LNA, a bandpass filter, a S/H stage and a VGA followed by an ADC. The architecture is conceptually simpler than the super-heterodyne receiver described in Chapter 2. The principle of operation of a subsampling architecture is well explained in [*Pekau and Haslett*, 2006], [*DeVries and Mason*, 2008] and [*Psiaki et al.*, 2005]. The RF signal is captured by the antenna and low-noise amplified by the LNA. In contrast to the heterodyne architecture, the RF signal is anti-aliasing filtered right after the LNA and directly sampled by the subsequent S/H stage. Direct sampling of the RF signal can be thought of as convolution of the incoming signal with an impulse train in the frequency domain. Let us assume the incoming RF signal is given in the time-domain by $x(t)$ and in the frequency domain by $X(f)$. The RF signal is sampled by the S/H stage which can be mathematically described in the time-domain by multiplication of $x(t)$ with Dirac impulses. The sampled signal $x_S(t)$ is given by

$$x_\text{s}(t) = x(t) \cdot \sum_{k=-\infty}^{\infty} \delta(t - k/f_\text{S}) \tag{3.1}$$

where f_S is the sampling frequency. The spectral representation of $x_\text{S}(t)$ is given by

$$X_\text{s}(f) = X(f) f_\text{S} * \sum_{k=-\infty}^{\infty} \delta(f - kf_\text{S}) = f_\text{S} \sum_{k=-\infty}^{\infty} X(f - kf_\text{S}) \tag{3.2}$$

Thus, the RF signal received by the antenna is aliased to frequencies spaced f_S apart from each other, a familiar result predicted by the Nyquist-Shannon Sampling Theorem. Note that the incoming RF signal has also a spectrally inverse frequency component at $-f_\text{RF}$ which is also aliased to frequencies spaced f_S apart from each other and $f_\text{S}/2$ apart from the aliasing frequencies of f_RF as illustrated in Figure 3.2. Sinc-distortion is not included in the spectrum in Figure 3.2 but has to be added if a zero-order hold S/H stage is used. The signal with the lowest frequency content is considered the IF.

In summary, subsampling architectures downconvert the RF signal to IF by aliasing. This is in contrast to downconversion by mixing and has also consequences for computing the NF. While the NF of a Gilbert Cell mixer is calculated taking into account only in-band noise and noise located at the image frequency, the NF of a subsampling receiver is computed by taking into account thermal noise from out-of-band sources that are aliased into the passband due to the sampling operation as illustrated in Figure 3.2. As it will be shown in the next section, to achieve a decent NF for a subsampling architecture, a good RF bandpass filter is necessary before subsampling to filter out the undesired out-of-band noise.

After downconversion, the VGA amplifies the IF signal to meet the input requirements of the quantizer. An IF filter before quantization can potentially be omitted if the RF filter is of higher order. Usually, it is still included serving as an image rejection filter and anti-aliasing filter. In contrast to the heterodyne architecture the off-chip crystal oscillator can directly provide the clock signal. As for the heterodyne architecture, frequency stability as well as superior phase noise performance is
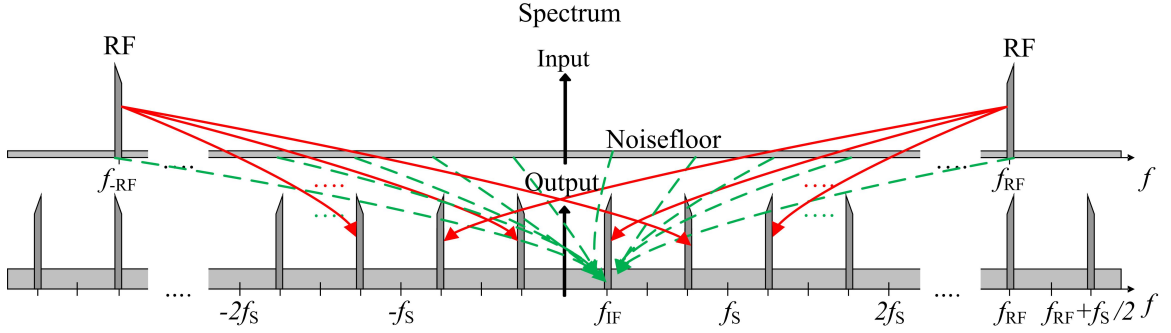
Figure 3.2: Spectral content of the signal at the input and output of the S/H stage. Aliasing of the two RF signal components at f_{RF} and $-f_{RF}$ (red, solid arrows) and noise aliasing from out-of-band noise sources (green, dashed arrows).

important for the subsampling architecture. Any frequency offset of the crystal oscillator ends up as frequency offset in the IF conceptually similar to the Doppler shift. Another concern is clock jitter which directly degrades receiver NF. A good external oscillator such as a temperature compensated crystal oscillator (TCXO) provides the necessary frequency stability and phase noise performance. A phase-locked loop (PLL) is not required for this architecture.

A main benefit of subsampling is to a build multi-frequency receiver that can process multiple signals simultaneously without adding complexity. Such a multi-frequency subsampling receiver is depicted in Figure 3.3, where only the center frequencies of the RF filters are tuned to the respective L1, L2 and L5 frequency while the S/H stages share the same crystal oscillator. As Psiaki showed, it is possible to downconvert the GPS frequencies L1, L2 and L5 and the Galileo signals simultaneously, for instance with a sampling frequency of 99.23 MHz.

In this chapter, a subsampling mixer is defined as ideal S/H stage preceded by a bandpass filter. Such an ideal subsampling mixer is illustrated in Figure 3.5. Several filter stages, sometimes providing extra gain, can be located before the S/H stage. Let f_S be the subsampling frequency of the sampling clock applied to the S/H stage. An RF carrier located at f_{RF} that is applied to the input of the subsampling mixer is downconverted to f_{IF} by aliasing. The spectral content at the output of the subsampling mixer is depicted in Figure 3.4. The IF is located at $f_0 = f_{IF}$; aliases are
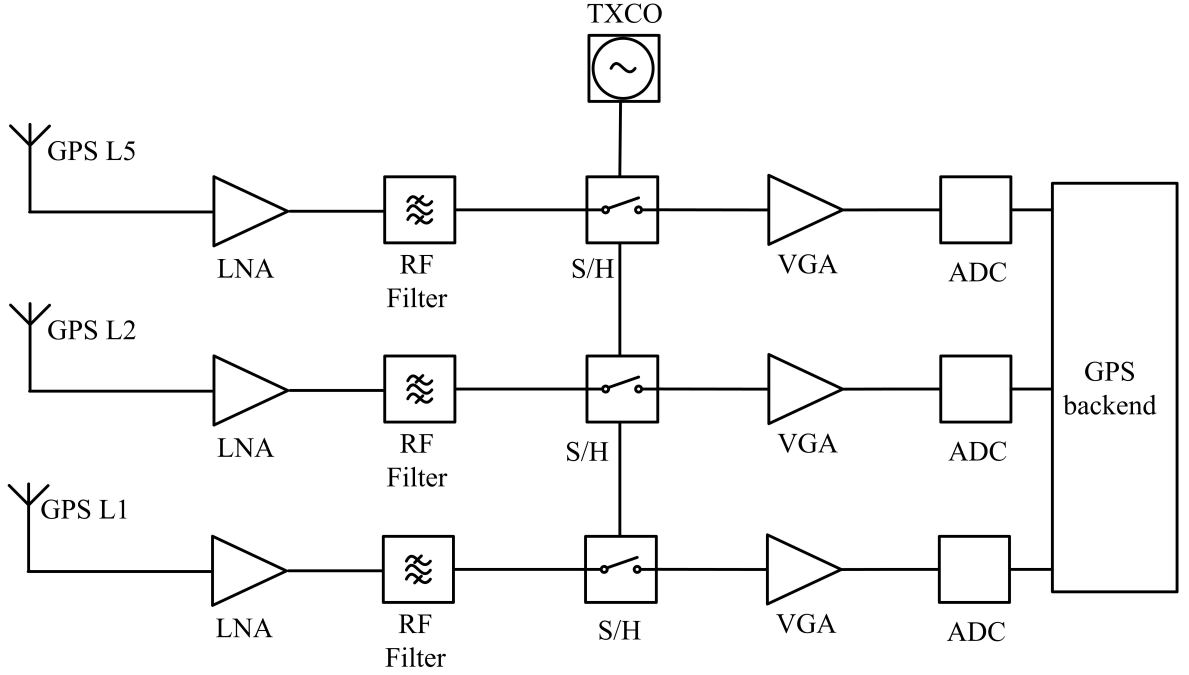
Figure 3.3: Multi-frequency subsampling architecture capable of downconverting GPS L1, L2 and L5.

located at f_1, f_2, ... In theory, the IF frequency can be chosen arbitrarily. However, it has been shown that a value of $f_S/4$ provides some IF processing benefits [*DeVries and Mason*, 2008]. It is important to note that not only thermal noise located at f_{RF} is downconverted to f_{IF} but also thermal noise located at f_1, f_2, ... as explained before. According to Figure 3.4, even order frequencies that alias to IF are given by

$$f_{2m} = (m + \Delta) f_S \quad m \; int \;, m \; \geq \; 0 \tag{3.3}$$

and odd order frequencies by

$$f_{2m-1} = (m - \Delta) f_S \quad m \; int \;, m \; \geq \; 1 \tag{3.4}$$

where Δ can be a number between 0 and 0.5. The location of the IF frequency relative to the subsampling frequency f_S is determined by the relation $f_{IF} = \Delta f_S$. The subsampling ratio n relating the sampling frequency f_S with the RF frequency f_{RF} is
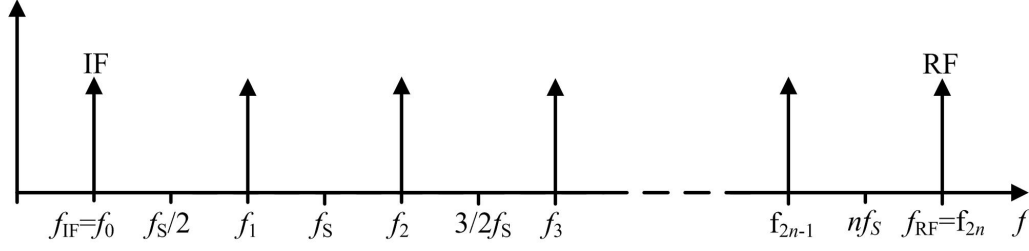
Figure 3.4: Output frequencies of the subsampling mixer

defined as follows:

$$\frac{f_{RF}}{f_\text{S}} = \frac{f_{2n}}{f_\text{S}} = n + \Delta \tag{3.5}$$

It can be seen from (3.3) and (3.5) that $f_\text{RF} = f_{2n}$ (which will be used interchangeably in the following derivation). In (3.5), the RF frequency is located at an even-order frequency above $n f_\text{S}$. Depending on the application, the RF frequency can be also located below $n f_\text{S}$ at an odd-order frequency. In the latter case the downconverted IF signal spectrum is flipped in the frequency domain as compared to the original RF signal spectrum.

3.2   Thermal Noise Figure

3.2.1   Mathematical Derivation

In this section, an expression for the thermal NF of a subsampling mixer is derived. The thermal noise factor F of a subsampling mixer can be calculated with the well-known formula from Section 2.4:

$$F = \frac{\text{Total Output Noise Power}}{\text{Total Output Noise Power due to the Source}} = \frac{P_\text{tot}}{P_\text{S,tot}} \tag{3.6}$$

The total available output noise power of the subsampling mixer evaluated at IF can be found by summing over all aliased noise components. As depicted in Figure 3.5, let $S(f)$ be the available noise power spectral density at the input of the S/H stage, $S_\text{Alias}(f)$ the available noise power spectral density at the output of the S/H stage, and $S_\text{s}(f)$ the available noise power spectral density from the source at the input of
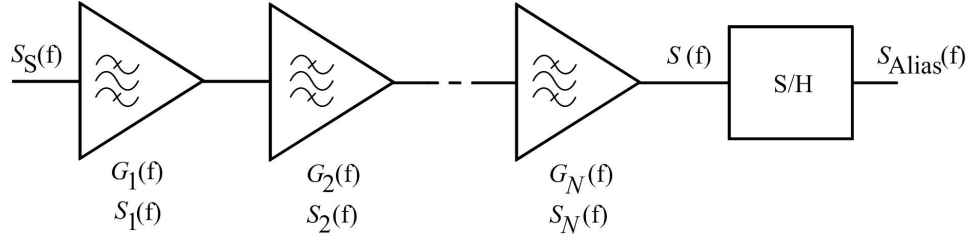
Figure 3.5: Multistage subsampling mixer. The available noise power spectral densities are given by $S_S(f)$, $S_1(f)$, ... , $S_n(f)$, $S(f)$ and $S_{Alias}(f)$. The available power gain per stage is given by $G_1(f)$, ...,$G_N(f)$. The S/H stage is assumed to be noiseless.

the subsampling mixer. $S_q(f)$ is the available noise power spectral density added by the q-th filter stage. $G_q(f)$ the available power gain of the of the q-th filter stage. The S/H stage is assumed to be noiseless since all input referred noise of the S/H stage can be included in $S_N(f)$. According to Figure 3.5, $S(f)$ is given by

$$S(f) = \prod_{k=1}^{N} G_k(f)S_S(f) + \prod_{k=2}^{N} G_k(f)S_1(f) + ...$$

$$+G_N(f)S_{N-1}(f) + S_N(f)$$

(3.7)

In most subsampling architectures f_{RF} is the center frequency of the bandpass filter. Therefore, $G_k(f_{RF})$ is the available passband gain of the k-th filter stage; in the following derivation, the shorter notations $G_k(f_{RF}) = G_k$ and $S_k(f_{RF}) = S_k$ are used for simplicity. The available power spectral density $S_{Alias}(f_{IF})$ after sampling can be found by summing over all aliased noise components according to (3.2):

$$S_{Alias}(f_{IF}) \propto \sum_{m=0}^{\infty} S(f_m)df$$

(3.8)

Note, that the factor f_S in (3.2) was omitted in (3.8) as we are only interested in the noise factor ratio. In (3.8) ideal impulse sampling is assumed. If the S/H stage is zero-order hold, then a sinc-distortion term will have to be included in (3.8). The total output noise power P_{tot} at the output of the S/H stage within an IF signal

bandwidth of $2B$ is given by

$$P_{\text{tot}} = \int_{f_{\text{IF}}-B}^{f_{\text{IF}}+B} S_{\text{Alias}}(f)df \propto \sum_{m=0}^{\infty} \int_{f_m-B}^{f_m+B} S(f)df \qquad (3.9)$$

and includes aliased out-of-band noise. The component $m = 2n$ in (3.9) represents the in-band noise, while the other values of m represent the aliased out-of-band noise. The output noise power due to the source within an IF bandwidth of $2B$ is given by

$$P_{\text{S,tot}} \propto \int_{f_{2n}-B}^{f_{2n}+B} \prod_{k=1}^{N} G_k(f)S_{\text{S}}(f)\, df \qquad (3.10)$$

and does not include aliased out-of-band noise. The noise factor F of the subsampling mixer can be computed by inserting (3.7), (3.9), (3.10) in (3.6). The derivation is further illustrated in Appendix A. The resulting noise factor F of the subsampling mixer is given by

$$F = S_{0N} + (F_1 - 1)S_{1N} + \frac{(F_2 - 1)}{G_1}S_{2N} + .. + \frac{(F_N - 1)}{\prod_{k=1}^{N-1} G_k}S_{NN} \qquad (3.11)$$

The coefficients S_{qN} are called *Aliasing Coefficients* and are defined by

$$S_{qN} = \sum_{m=0}^{\infty} R_{qN}^m \qquad (3.12)$$

where

$$R_{0N}^m = \frac{\displaystyle\int_{f_m-B}^{f_m+B} G_{1N}(f)\frac{S_{\text{S}}(f)}{S_{\text{S}}}df}{\displaystyle\int_{f_{2n}-B}^{f_{2n}+B} G_{1N}(f)\frac{S_{\text{S}}(f)}{S_{\text{S}}}\, df} \qquad (3.13)$$

and

$$R_{qN}^m = \frac{\displaystyle\int_{f_m-B}^{f_m+B} G_{(q+1)N}(f)\frac{S_q(f)}{S_q}df}{\displaystyle\int_{f_{2n}-B}^{f_{2n}+B} G_{1N}(f)\frac{S_{\text{S}}(f)}{S_{\text{S}}}\, df}; \quad q = 1, ..., N-1 \qquad (3.14)$$

and

$$R_{NN}^m = \frac{\int_{f_m-B}^{f_m+B} \frac{S_N(f)}{S_N} df}{\int_{f_{2n}-B}^{f_{2n}+B} G_{1N}(f) \frac{S_S(f)}{S_S} df} \tag{3.15}$$

where the cascaded available gain $G_{pq}(f)$ from stage p to stage q, normalized by the available gain at frequency f_{RF} is defined by the relationship

$$G_{pq}(f) = \prod_{k=p}^{q} \frac{G_k(f)}{G_k} \qquad 1 \le p \le q \le N \tag{3.16}$$

$G_{pq}(f)$ is the transfer function of the cascaded RF filter stage from the input of stage q to the output of stage p, normalized to 0 dB at the center frequency f_{RF} (since $G_k = G_k(f_{RF})$). F_q in (3.11) is the spot noise factor of the q-th filter stage evaluated at frequency f_{RF}. It is evident by comparing (3.11) with (2.20) that (3.11) is indeed a modified version of the Friis equation weighted by the Aliasing Coefficients S_{qN}.

3.2.2 Interpretation

Equation (3.13)–(3.15) can be further simplified assuming that the available gain and the available noise power spectral density are approximately constant within the bandwidth of $2B$. This is a reasonable assumption since the bandwidth of interest $2B$ is typically a lot smaller than the RF center frequency. For example, the RF frequency of the GPS L1 signal is at 1575.42 MHz. The bandwidth of the GPS L1 C/A code is 2 MHz. In such case, (3.13)–(3.15) simplify to

$$R_{0N}^m = G_{1N}(f_m) \frac{S_S(f_m)}{S_S} \tag{3.17}$$

$$R_{qN}^m = G_{(q+1)N}(f_m) \frac{S_q(f_m)}{S_q}; \quad q = 1, ..., N-1 \tag{3.18}$$

$$R_{NN}^m = \frac{S_N(f_m)}{S_N} \tag{3.19}$$

$S_q(f_m)/S_q$ is the normalized (since $S_q = S_q(f_{\mathrm{RF}}) = S_q(f_{2n})$) available noise power spectral density added by filter stage q, evaluated at frequency f_m. $G_{(q+1)N}(f_m)$ is the normalized cascaded filter transfer function from the output of stage q to the output of stage N, evaluated at frequency f_m. $G_{(q+1)N}(f)$ has a bandpass filter characteristic in subsampling architectures. Thus, the terms R_{qN}^m in (3.17)–(3.19) can be understood as the normalized available noise power spectral density originating from the q-th filter stage or the source of the subsampling mixer, measured at the input of the S/H stage. This is illustrated in Figure 3.6, where a typical curve for the normalized noise power spectral density originating from stage q — measured at the input of the S/H stage — has been plotted. The curve has a bandpass filter characteristic and is normalized so that the maximum of the available noise power spectral density is 1 at the RF center frequency. The terms R_{qN}^m represent the value of the normalized noise power contribution from stage q at the input of the S/H stage, evaluated at frequency f_m. The out-of-band noise component is weighted by R_{qN}^m while in the in-band noise component ($m = 2n$) is weighted by 1 reflecting that this component is aliased to IF without any filtering. The Aliasing Coefficients S_{qN} as defined in (3.12) can be interpreted as the summation of all filtered noise contributions from stage q that are aliased down to the same IF.

Equations (3.13)–(3.15) are equivalent to equations (3.17)–(3.19) except that for the derivation of the latter it was assumed that the noise power spectral density it is constant over $2B$. The Aliasing Coefficients S_{qN} are solely dependent on the shape (and not the gain) of the transfer function for noise originating from stage q to the input of the S/H stage. It is also apparent from Figure 3.6 that $S_{qN} \geq 1$. If an ideal rectangular filter is used, no out-of-band aliasing occurs and $S_{qN} = 1$. The Aliasing Coefficients S_{qN} can be found from the noise transfer functions of the stages, either by AC simulation or by hand calculation.

To gain further insight, more approximations are made in the following analysis. If the gain of the first stage G_1 is sufficiently high, (3.11) can be simplified by keeping only the first two terms:

$$F \simeq S_{0N} + (F_1 - 1)S_{1N} \tag{3.20}$$
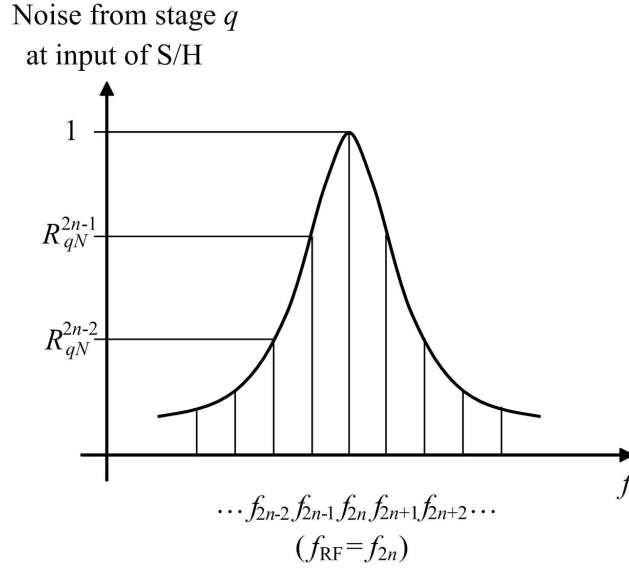
Figure 3.6: Normalized available noise power spectral density for noise originating from stage q, measured at the input of the S/H stage.

If a narrowband Q-enhanced bandpass filter is used for the second stage and a LNA with noise factor F_1 as first stage, then S_{0N} and S_{1N} in (3.20) are approximately equal since the normalized noise transfer function of the narrowband filter dominates the overall noise transfer function from the input of the LNA to the input of the S/H stage. In this case,

$$F \simeq F_1 \cdot S_{1N} \tag{3.21}$$

Hence, the NF becomes

$$NF \simeq 10 \log(F_1) + 10 \log(S_{1N}) \tag{3.22}$$

It is apparent that in this case, the Aliasing Coefficient S_{1N} increases the spot NF of the system. Without noise aliasing, this figure would simply be $10 \log(F_1)$. Thus, for the purpose of total system noise factor calculations, noise from out-of-band aliasing can be treated as an additional stage with equivalent noise factor S_{1N}. The NF $10 \log(S_{1N})$ accounting for out-of-band aliasing can be just added to the simple spot NF on a log scale diagram. It is important to note that (3.21) is one of the most

practical and frequent cases.

3.2.3   Computation of the Aliasing Coefficients

In the following, the Aliasing Coefficients S_{qN} defined by (3.12) are computed for typical filter characteristics. It was recently shown by *Wiser*, [2008] that a higher order bandpass filter can be implemented in an IC with arbitrary filter characteristic. Such filters are referred to as stagger-tuned filters that use Q-enhanced resonators to control the poles and zeros of the filter transfer function. R_{qN}^m is the value of the normalized noise transfer function for noise originating from stage q, measured at the input of the S/H stage and evaluated at frequency f_m. In most subsampling architectures, the normalized noise transfer function can have either a bandpass or lowpass filter characteristic. If a sufficiently narrow bandpass filter is used, such as a Q-enhanced RF bandpass filter, the overall normalized noise transfer function is approximately equal to the normalized narrow bandpass filter transfer function. This observation greatly simplifies the analysis in the sense that for the calculation of R_{qN}^m and S_{qN} only the dominant transfer filter characteristic has to be taken into account.

In the following, S_{qN} is evaluated for a first order low-pass filter characteristic and for higher order bandpass filter characteristics. The transfer function of a RF bandpass filter of 2N-th order with Butterworth characteristic is given by [*Pozar*, 1998, pp. 443-470]

$$R_{qN}^m = \frac{1}{1 + \left(\frac{f_{\mathrm{RF}}}{f_{\mathrm{C}}} \left(\frac{f_m}{f_{\mathrm{RF}}} - \frac{f_{\mathrm{RF}}}{f_m} \right) \right)^{2N}} \tag{3.23}$$

and the transfer function of a Chebyshev filter of 2N-th order by

$$R_{qN}^m = \frac{1}{1 + \varepsilon^2 T_N^2 \left(\frac{f_{\mathrm{RF}}}{f_{\mathrm{C}}} \left(\frac{f_m}{f_{\mathrm{RF}}} - \frac{f_{\mathrm{RF}}}{f_m} \right) \right)} \tag{3.24}$$

where f_{C} is the 3 dB bandwidth of the filter; ε represents the ripple of the Chebyshev filter and T_N is the Chebyshev polynomial of N-th order. Using (3.12), S_{qN} can be calculated by summing over (3.23) or (3.24). For simplicity, the terms S_{qN} were only derived for a Butterworth filter characteristic but it is straightforward to derive S_{qN}

for Chebyshev filters. S_{qN} is plotted into Figure 3.7 for a second order Butterworth filter versus the subsampling ratio n and the inverse of the normalized bandwidth f_C/f_{RF} as parameter. The corresponding second order Butterworth noise transfer function is plotted into Figure 3.15. Δ is assumed to be 0.25 so that $f_{IF} = f_S/4$. Two cases are distinguished. First, the bandwidth $2B$ is set equal to $f_S/2$ in (3.13), (3.14) and (3.15). Second, the bandwidth $2B$ is much smaller than $f_S/2$ so that equation (3.17), (3.18) and (3.19) can be applied. Therefore, two curves per f_{RF}/f_C are plotted, where the solid curve corresponds to $2B = f_S/2$ and the dashed curve corresponds to $2B << f_S/2$. It is interesting to observe, that the case where $2B$ spans the entire subsampling bandwidth $f_S/2$ represents the worst case scenario. Thus, the Aliasing Coefficients of a real subsampling mixer will be somewhere between these two curves for finite bandwidth $2B < f_S/2$.

In Figure 3.8 and Figure 3.9, S_{qN} is plotted for a fourth and sixth order Butterworth bandpass filter noise transfer function. Finally, in Figure 3.10, S_{qN} is plotted for a first-order lowpass type noise transfer function with 3 dB frequency f_C. The respective Butterworth noise transfer functions are plotted in Figure 3.16 and Figure 3.17. Several interesting observations can be drawn from the figures: First, the Aliasing Coefficients S_{qN} decrease with increasing subsampling frequency or decreasing subsampling ratio. This is expected as with a higher subsampling frequency, less noise folding occurs. Second, a smaller filter bandwidth decreases the Aliasing Coefficients S_{qN} because the aliased noise will be attenuated more strongly. Also, comparing Figure 3.7 – Figure 3.9, a lower NF can be achieved by a higher filter order.

Figure 3.7 – Figure 3.9 can be applied to (3.22) to find the increase in NF resulting from aliased out-of-band noise of a subsampling mixer with a bandpass filter characteristic. The Aliasing Coefficient S_{1N} can be directly found from Figure 3.7 – Figure 3.9. If multiple stage filtering is applied before sampling, the NF has to be computed with the more general equation (3.11). The Aliasing Coefficients can still be found approximately from Figure 3.7 – Figure 3.9. For example, if the first stage is a very narrow second order bandpass filter with Butterworth filter characteristic and the second stage a wideband lowpass filter, the transfer function from the input of the

Figure 3.7: Aliasing Coefficient S_{qN} (in dB) due to out-of-band aliasing in a subsampling mixer with the second order Butterworth filter characteristic shown in Figure 3.15. The NF is a function of the inverse of the normalized filter bandwidth $f_{\mathrm{C}}/f_{\mathrm{RF}}$ and the subsampling ratio. Two different cases are displayed: Noise is integrated over $2B = f_{\mathrm{S}}/2$ for the solid lines and over $2B << f_{\mathrm{S}}/2$ for the dashed lines.

first stage to the sampler is dominated by the bandpass filter. The transfer function from the output of the first stage to the S/H stage, however, exhibits a lowpass filter characteristic. In that case, S_{1N} can be found from figure Figure 3.7 and S_{2N} from Figure 3.10. If, on the other hand, both filters are narrow second order bandpass filters with Butterworth characteristic, then the transfer function from the input of the first stage to the S/H stage is of fourth order and S_{1N} can be found from Figure 3.8 while the transfer function from the output of the first stage to the S/H stage is of second order and figure Figure 3.7 has to be used to approximate the NF of the subsampling mixer. In most cases, the first stage of the subsampling mixer exhibits a bandpass filter characteristic and the second stage, the S/H stage, a lowpass filter
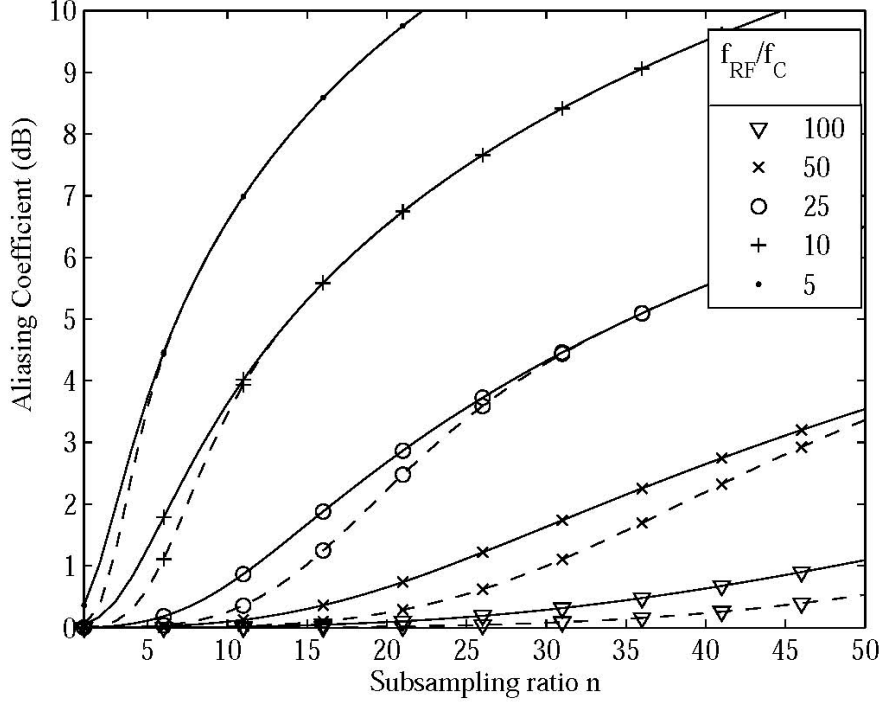
Figure 3.8: Aliasing Coefficient S_{qN} (in dB) due to out-of-band aliasing in a sub-sampling mixer with the fourth order Butterworth filter characteristic shown in Figure 3.16. The NF is a function of the inverse of the normalized filter bandwidth f_C/f_{RF} and the subsampling ratio. Two different cases are displayed: Noise is integrated over $2B = f_S/2$ for the solid lines and over $2B << f_S/2$ for the dashed lines.

characteristic.

An important aspect in subsampling architectures is the effect of higher order terms in the modified Friis equation in (3.11). In the conventional Friis equation, the noise factor of subsequent stages is dividend by the gain of the preceding stages. Therefore, the first stages have to provide sufficient gain so that the noise from higher order stages has no effect on the cascaded noise factor. In subsampling architectures, the noise factors of the higher order stages are scaled by the Aliasing Coefficients S_{qN}; thus the higher order terms in (3.11) are larger than in the conventional Friis equation and a higher gain needs to be provided by the first stages. In order for
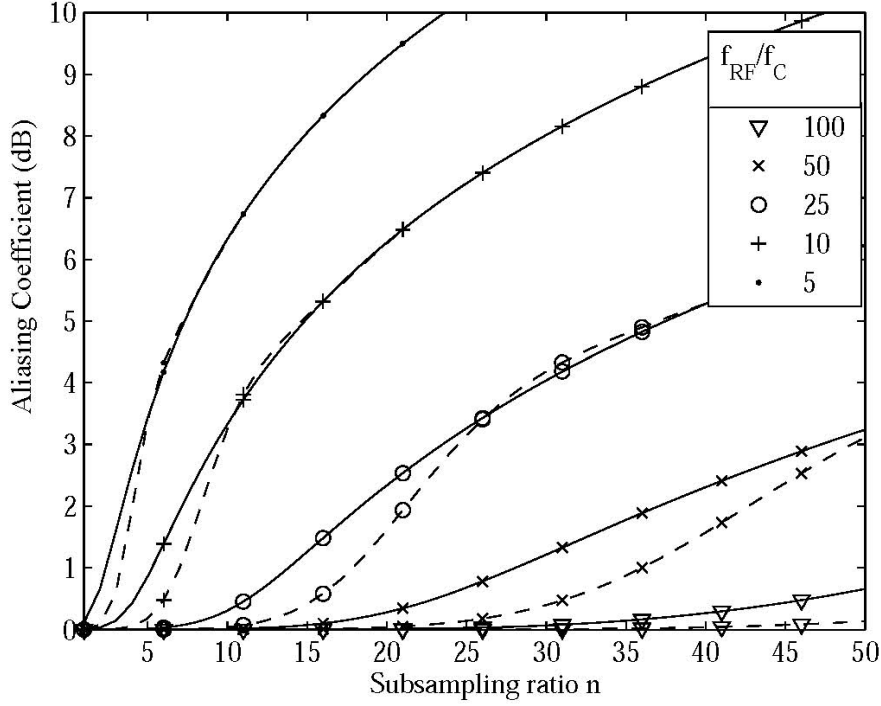
Figure 3.9: Aliasing Coefficient S_{qN} (in dB) due to out-of-band aliasing in a subsampling mixer with the sixth order Butterworth filter characteristic shown in Figure 3.17. The NF is a function of the inverse of the normalized filter bandwidth f_C/f_{RF} and the subsampling ratio. Two different cases are displayed: Noise is integrated over $2B = f_S/2$ for the solid lines and over $2B << f_S/2$ for the dashed lines.

approximation (3.20) to be valid,

$$S_{0N} + (F_1 - 1)S_{1N} >> \frac{(F_2 - 1)}{G_1}S_{2N} \tag{3.25}$$

The available gain G_1 has to be significantly larger than the product of S_{2N} and the spot noise factor $(F_2 - 1)$. This is in contrast with the conventional Friis equation where the gain G_1 has to be only significantly larger than $(F_2 - 1)$. The higher order terms are a critical factor in subsampling architectures and need to be considered.

In most designs, the transfer function for noise produced after the bandpass filter stages exhibits a lowpass filter characteristic because the S/H stage typically has
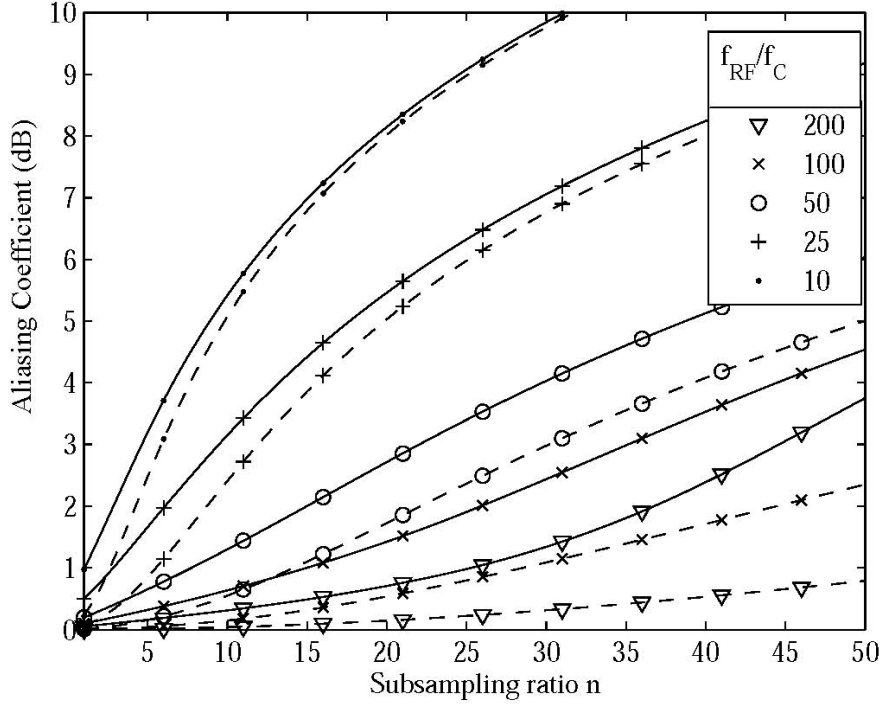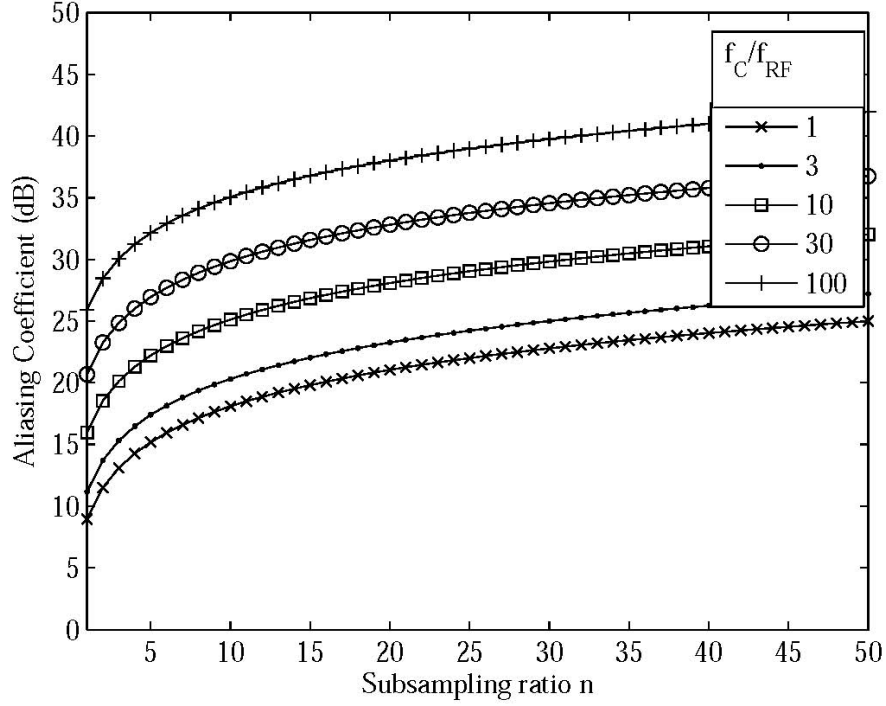
Figure 3.10: Aliasing Coefficient S_{qN} (in dB) due to out-of-band aliasing in a sub-sampling mixer with a first order lowpass filter characteristic. The NF is a function of the normalized filter bandwidth f_C/f_{RF} and the subsampling ratio.

a RC type lowpass filter characteristic. For example, assume that the first stage is a Q-enhanced stagger-tuned bandpass filter and the second stage a VGA with lowpass filter characteristic. The respective spot noise factors (evaluated at f_{RF}) are F_1 and F_2 and the available RF gains (evaluated at f_{RF}) are G_1 and G_2. Then, the normalized noise transfer function from the input of the filter to the S/H stage exhibits a bandpass filter characteristic as well as the transfer function for noise originating from the bandpass filter itself. Thus, $S_{0N} \simeq S_{1N}$. Assuming that the higher order terms are negligible, the noise factor can then be found from (3.11)

$$F \simeq F_1 S_{1N} + \frac{(F_2 - 1)}{G_1} S_{2N} \tag{3.26}$$

If the normalized transfer function for noise from the VGA to the S/H stage exhibits

a lowpass filter characteristic, S_{2N} has to be found from Figure 3.10. To achieve a low NF, the available gain G_1 has to be significantly larger than S_{2N} which can be as high as 40 dB. This detail is often overlooked in the design of subsampling architectures leading to higher system NFs. The assumption that the S/H stage exhibits a low pass filter characteristic is true in most cases since the S/H stage is usually a RC type of filter, which has to be taken into account when computing S_{2N}.

3.3 Clock Jitter

Another source of noise stems from the finite phase jitter of the sampling clock. Aperture jitter causes an uncertainty in the sampling instances, which effectively adds to the system noise and results in a degradation of signal-to-noise ratio therefore increasing the NF of the mixer. The following analysis is a simplified version of the analysis performed in [*Arkesteijn et al.*, 2006]. The incoming signal is sampled by the S/H stage as depicted in Figures 3.11. The goal of the following analysis is find the equivalent rms input power due to jitter and treat the sample and hold stage as noiseless as illustrated in 3.12. Expressing jitter as zero mean random variable τ, the sampling instances t_n are given by

$$t_\mathrm{n} = \tau + \frac{n}{f_\mathrm{s}}, \quad n \; integer \tag{3.27}$$

As shown in Figure 3.13, aperture uncertainty ΔV_RF is related to the clock jitter via the slope of the subsampled signal by

$$\Delta V_\mathrm{RF} = \frac{dV_\mathrm{RF}}{dt}\tau \tag{3.28}$$

For the purpose of this calculation it is sufficient to treat the bandpass filtered GPS signal as deterministic narrowband signal. It can be therefore written as

$$V_\mathrm{RF}(t) = A(t)\cos(2\pi f_\mathrm{RF}t + \phi(t)) \tag{3.29}$$

where the amplitude and the phase is given by $A(t)$ and $\phi(t)$, respectively. Since the
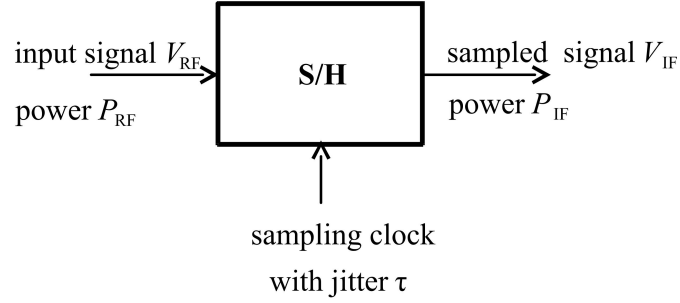
Figure 3.11: Sample and hold stage with clock jitter
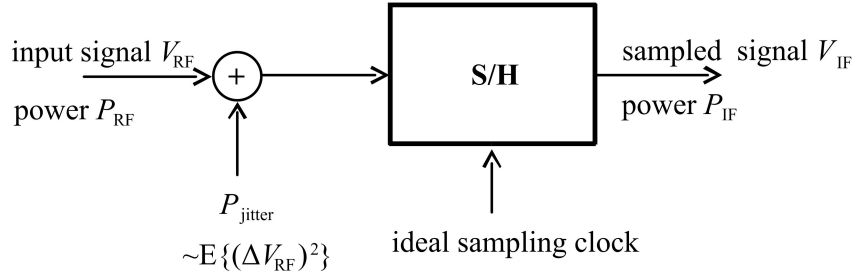
Figure 3.12: Ideal Sampled and Hold stage, where clock jitter causing aperture uncertainty is represented as input referred Gaussian noise source.

signal is narrowband, $A(t)$ and $\phi(t)$ are slowly varying with respect to the carrier frequency f_{RF}. The rms noise power introduced by aperture jitter P_{Jitter} is related to the expected value of $(\Delta V_{\mathrm{RF}})^2$

$$
\begin{aligned}
P_{\mathrm{Jitter}} \propto E[(\Delta V_{\mathrm{RF}})^2] &= \left(\tfrac{dV_{\mathrm{RF}}}{dt}\right)^2 E[\tau^2] \\[2mm]
&= \left(\tfrac{d}{dt}\left(A(t)\cos(2\pi f_{\mathrm{RF}}t + \phi(t))\right)\right)^2 \sigma_\tau^2 \\[2mm]
&\approx E[(2\pi f_{\mathrm{RF}} A(t)\cos(2\pi f_{\mathrm{RF}}t + \phi(t)))^2]\sigma_\tau^2 \\[2mm]
&\approx 1/2 A(t)^2 \left(2\pi f_{\mathrm{RF}}\right)^2 \sigma_\tau^2
\end{aligned}
$$

$$(3.30)$$

where use of the approximation was made that $A(t)$ and $\phi(t)$ are slowly varying with respect to the carrier frequency f_{RF}. The rms signal power P_{Signal} is related to $A(t)$

$$\Delta V_{\mathrm{RF}} = \frac{dV_{\mathrm{RF}}}{dt}\tau$$
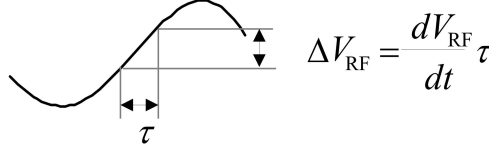
Figure 3.13: Aperture uncertainty and the clock jitter are related via the slope of the subsampled signal.

by

$$P_{\mathrm{Signal}} \propto 1/2 A(t)^2 \tag{3.31}$$

resulting in the well-known equation for the NF due to jitter

$$NF = 10\log(1 + \frac{P_{\mathrm{Jitter}}}{P_{\mathrm{Signal}}}) = 10\log(1 + (2\pi f_{\mathrm{RF}})^2 \sigma_{\tau}^2) \tag{3.32}$$

which depends only on the variance of the clock jitter and the frequency of the incoming GPS signal. This relationship for the NF of the sample and hold stage due to clock jitter is plotted into Figure 3.14 for relevant GPS signal frequencies between 1 and 2 GHz. As it can be seen, acceptable NFs can be achieved if the rms clock jitter is below 20 ps. This is a rather unambitious target given that recent developments in high frequency, fixed frequency oscillators offer less than 10 ps rms phase jitter and often even less than 1 ps rms phase jitter [*Wei et al.*, 2006], [*Van den Homberg*, 1999], [*Lam*, 2008]. The NF due to clock jitter is likely to be even smaller since in (3.32) the jitter power over the entire Nyquist range is considered. Since the subsampled signal is often highly oversampled, only the jitter power that falls within the signal band needs to be considered [*Arkesteijn et al.*, 2006]. This result is in line with the findings by *DeVries and Mason*, [2008], showing that the performance degradation due to clock jitter for a RF subsampling receiver is of the same order of magnitude as for a super-heterodyne receiver.

It is interesting to note that (3.32) is independent of the subsampling frequency. However, depending on the oscillator, σ_{τ} can indeed be a function of the oscillator frequency.
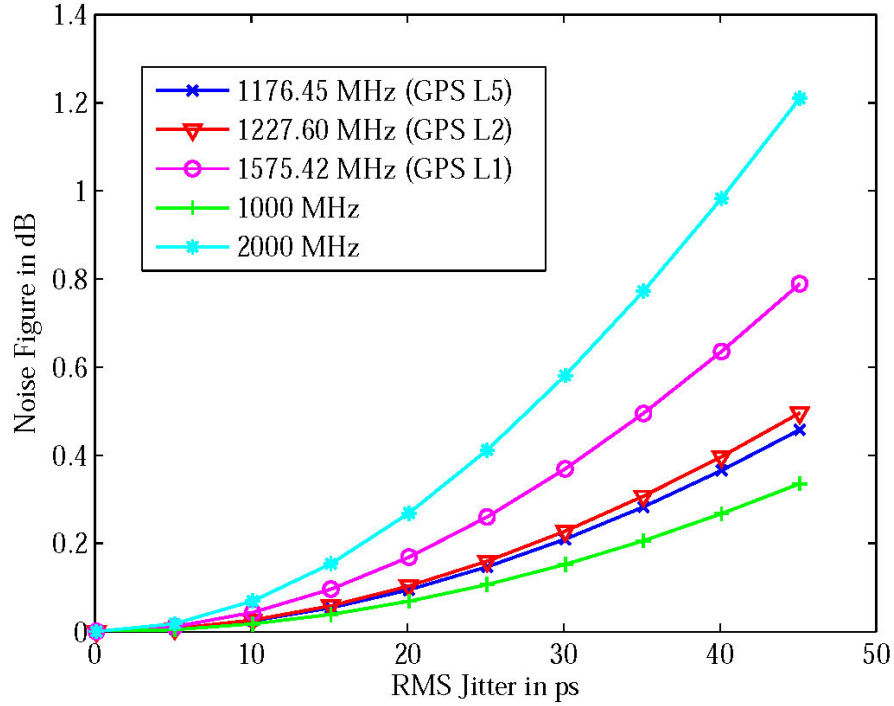
Figure 3.14: Noise figure of the sample and hold stage due to clock jitter causing aperture uncertainty.

3.4 Interference

Interference plays an important role in subsampling architectures. Any out-of-band interference spaced multiples of the sampling frequency apart will alias into the IF band. Therefore, adequate bandpass filtering has to be provided to ensure that interferers are sufficiently suppressed before bandpass sampling. Such an analysis was performed in [*DeVries*, 2008] for a second order bandpass filter and is extended here for higher order filters.

Using the same notation as in Section 3.2 the suppression or attenuation A of interference in dB at frequency f can be directly found from the filter transfer function
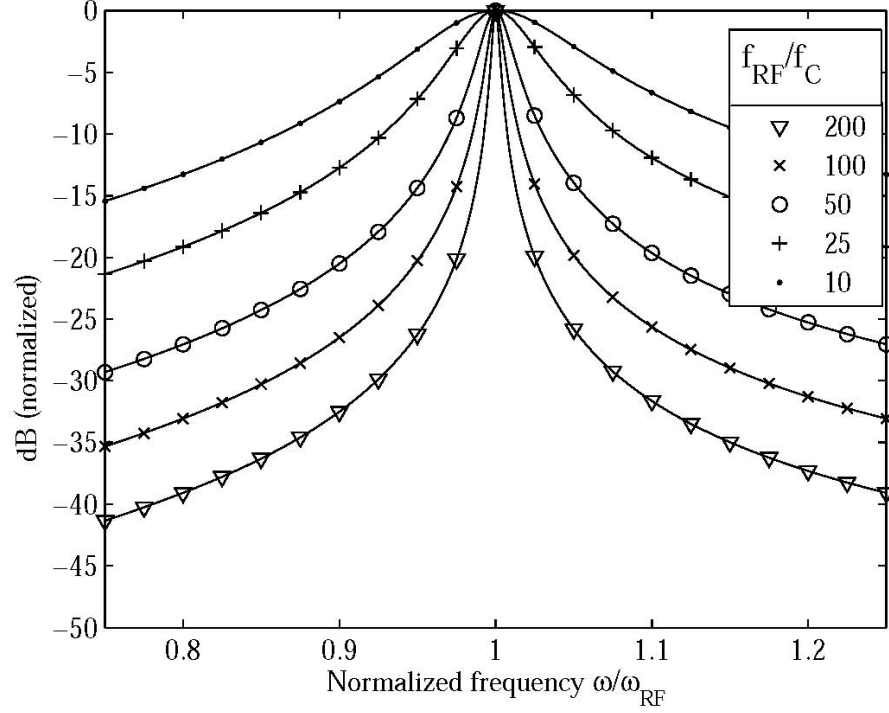
Figure 3.15: Noise transfer function of a second order Butterworth filter versus normalized frequency.

G_{1N} from stage 1 to stage N by

$$A = 10 \log G_{1N}(f) = 10 \log \left(\prod_{k=1}^{N} \frac{G_k(f)}{G_k} \right) \qquad (3.33)$$

The filter transfer functions are plotted into Figure 3.15 – Figure 3.17 for a Butterworth filter of second, fourth and sixth order, respectively. Satisfying the interference requirements of some GPS applications can be challenging for subsampling architectures. Interference is a problem especially in the vicinity of the center frequency if a Butterworth filter architecture is employed. In subsampling architectures many harmonics potentially end up within the receiver IF bandwidth. A second order bandpass filter is often not enough and higher order filter architectures in conjunction with an external Surface Acoustic Wave (SAW) filter are required if operated in
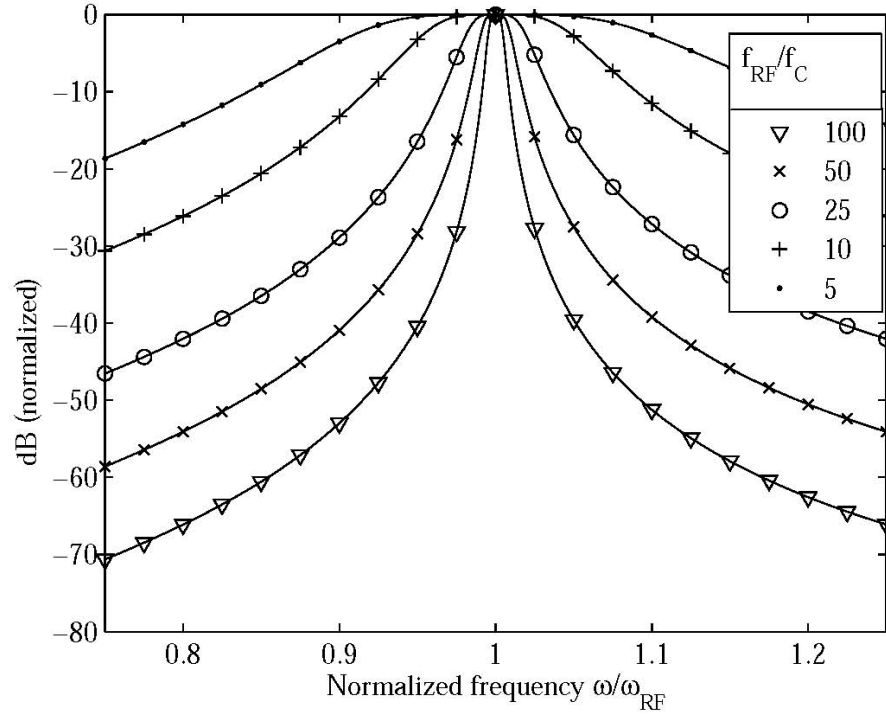
Figure 3.16: Noise transfer function of a fourth order Butterworth filter versus normalized frequency.

high interference environments as often encountered in handheld devices.

In a Gilbert-Cell based heterodyne receiver, for instance, there is only one frequency that can generate an image within the receiver IF bandwidth. This problem can be further mitigated in heterodyne architectures by employing quadrature mixer architectures such as the Weaver architecture that are able to suppress the image frequency. In practice, these receiver architectures achieve less than 35 dB of image suppression and an off-chip SAW filter is required nevertheless [*Lee*, 1998, pp. 700-701].

For GPS receivers, interference within the GPS band can come from either spurious harmonic mixing products from adjacent transmitters or from intentional jamming. Due to its wider bandwidth, the GPS C/A code is less vulnerable to interference than narrowband signals. In addition to interference suppressing filters, several techniques can be applied to improve the ability to reject interference. As summarized
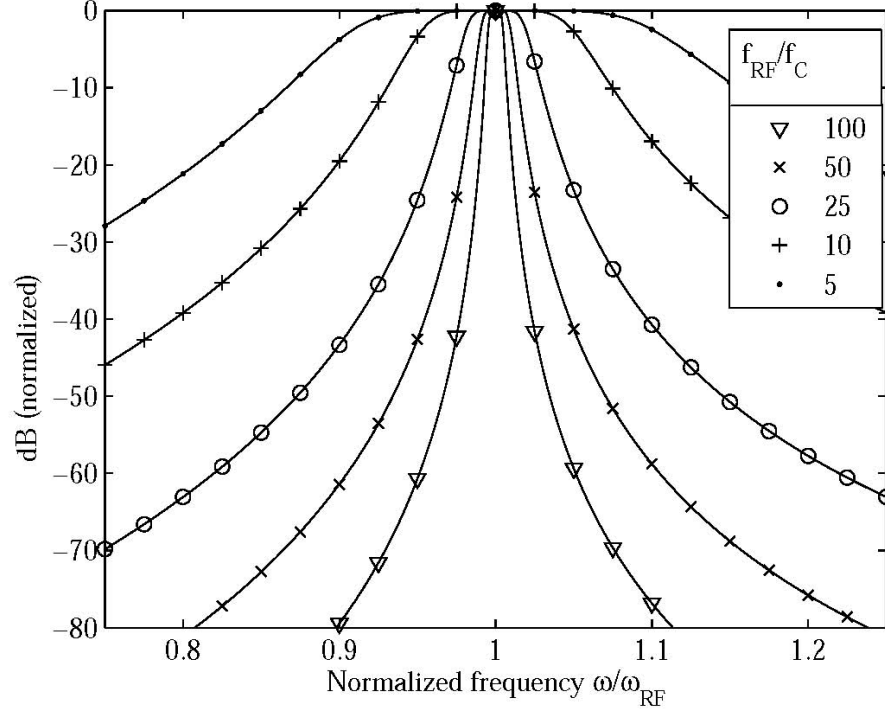
Figure 3.17: Noise transfer function of a sixth order Butterworth filter versus normalized frequency.

in [*Parkinson et al.*, 1996, Chapter 20], most of the techniques are implemented in the back-end digital signal processing (DSP) unit of the receiver and are not considered here. However, in-band interference can significantly degrade the carrier to noise ratio C/N_0 of GPS receiver front-ends if the signal is quantized by a 1-bit ADC. Higher order ADCs provide significantly improved performance in high interference environments [*Parkinson et al.*, 1996, pp.354–355].

3.5 Quantization Noise

The signal sampled by the ADC consists of the GPS signal plus a much larger component of thermal noise, which is fed into the DSP unit for further processing. In the DSP unit, the detector correlates the signal with a replica of the C/A code during

the so-called code-wipeoff. The optimum detector for the GPS signal buried in Gaussian noise would be an ideal matched filter, where correlation of the GPS signal with the replica C/A code is achieved through convolution by integration. Such a filter cannot be implemented in a practical receiver. Instead, the signal is quantized by an ADC and correlated with the replica code by summation instead of integration. Such an arrangement is also know as Digital Matched Filter (DMF), which introduces a correlation loss with respect to the ideal matched filter.

In [*Chang*, 1982], the degradation factor D of a DMF is defined as the necessary increase in energy per bit to noise power spectral density ratio E_{b}/N_0 to achieve the same bit error rate P_{e} as the ideal matched filter. This analysis has been performed by *Chang*, [1982] where tables are provided for the resulting degradation. Using a 1-bit ADC, the quantization loss D of a signal buried in Gaussian noise is about 2 dB if the noise bandwidth is large compared to the signal bandwidth. For higher order quantization, the quantization loss D improves significantly but becomes a function of the maximum ADC threshold voltage relative to the RMS noise power. For example, for a 2-bit ADC the lowest quantization loss of about 0.7 dB is achieved if the maximum ADC threshold is approximately equal to the RMS noise level. For 3-bit quantization, the quantization loss can be about as low as 0.3 dB assuming a wide noise bandwidth.

Chapter 4

Circuit Implementation

The subsampling GPS receiver chip was fabricated in a 130 nm BiCMOS process from National Semiconductor. This process is very suited for RF applications due to the high transit frequency of the process, the availability of spiral inductors, metal comb capacitors and tunable varactors. The process enables high quality inductors by the availability of two thick top metal layers. Using a patterned ground shield, the inductor quality factor can be as high as 20. The process is rounded off by bipolar devices which allow high speed operation with lower power consumption. Only CMOS transistors are used in the chip except for the test buffers that match the high impedance at the output of the filter to the 50 Ω impedance that is required by most test equipment. Bipolar transistors were not employed in the main signal path of the receiver, which was done for reasons of comparability with other CMOS architectures. A competitive power consumption is a achieved through use of a 1.2 V supply voltage which is enabled by low threshold CMOS devices.

In this chapter, the circuit and layout techniques employed in the subsampling GPS receiver are discussed. In the beginning, the architectural design choices are reviewed and the receiver gain and frequency plan is presented. In the next sections, the circuits of the RF building blocks are explained including the LNA, the RF filter, the S/H stage and the VGA. Then, the tuning algorithm for the RF filter is formulated. Finally, the layout of the IC is discussed at the very end.

4.1 Design Choices

4.1.1 Architecture and Gain Plan

The gain plan of the GPS receiver front-end is depicted in Figure 4.1. It shows the architecture of the subsampling GPS receiver which was treated in Chapter 2 and 3 on a theoretical basis. The first row in the table below the figure shows the voltage gain of each stage in the architecture. In the second row the cumulative voltage gain is printed and in the third row the cumulative NF. Most of these values are simulated. Only the values that can be accessed by measurement equipment at the output of the buffer stage and the output of the GPS receiver after the VGA are measured quantities. The receiver achieves the lowest ever reported NF of 3.8 dB, more than 4 dB lower than in previously reported subsampling receivers [*Pekau and Haslet*, 2005, 2007], [*DeVries and Mason*, 2008]. The subsampling NF penalty is less than 1 dB. The power consumption and the NF is comparable with state-of-the-art heterodyne GPS receiver front-ends [*Cheng et al.*, 2009].

The LNA with a 50 Ω input impedance is based on the well-known inductively-degenerated topology [*Shaeffer and Lee*, 1997]. The LNA provides 18 dB of gain with a NF of 2.5 dB. The gain of the LNA is not large enough to overcome the input referred noise of the RF filter. Therefore, an additional amplifier was added between the LNA and the filter. The supplementary amplifier has 7 dB of extra gain affecting the NF of the system only slightly.

The Q-enhanced RF filter is capable of suppressing interference close to the RF carrier frequency. This is an important requirement since interference from out-of-band can alias in-band and corrupt the GPS signal, which is of special concern if a 1-bit ADC is used for quantization [*Parkinson et al.*, 1996, pp. 724–745]. The RF filter uses a LCC series parallel resonant tank for image rejection. The input impedance of the LCC tank exhibits a closely spaced zero-pole doublet creating a notch in the transfer function at 1540 MHz and at 1610 MHz. The notch at 1540 MHz and 1610 MHz attenuates noise and interference close to the center frequency which is not attenuated in conventional subsampling architectures, a main factor leading to historically elevated NFs. The 3 dB bandwidth of the filter is 20 MHz.

The center frequency is at 1575 MHz. The RF filter has a gain of 25 dB. Hence, the total cumulative gain of the LNA, the common source amplifier and the filter is thus 50 dB. The NF at the output of the filter was measured to be 3.2 dB. An RF buffer allows measuring the voltage at the filter output and provides an output impedance match to the 50 Ω input impedance of the measurement equipment.

Cross-coupled differential pairs are applied to moderately enhance the Q-factor of the on-chip spiral inductors. A higher level of Q-enhancement leads to a reduced in-band linearity. Out-of-band linearity is barely affected by Q-enhancement. Reduced in-band linearity can be tolerated for a GPS receiver with low bit quantization since jamming of the receiver back-end occurs at an in-band interference level as low as -110 dBm. Thus, the receiver is jammed already at signal levels significantly below the in-band compression. The out-of-band linearity is limited by the common source amplifier and could likely be improved.

Depending on the environment and application of the GNSS receiver, there can be a significant amount of out-of-band interference due to adjacent channels. These out-of-band signals can saturate the receiver front-end, generate undesired intermodulation products and lead to unacceptable NFs. In practice, techniques that prevent saturation of the receiver front-end include the use of external RF filter stages. For example, an external Surface Acoustic Wave (SAW) filter can be placed between the antenna and the receiver, which attenuates the undesired out-of-band interference.

After the filter, the RF signal is sampled by a S/H stage which mixes the RF signal down to IF by aliasing. The available power of the GPS L1 signal is -130 dBm, the available noise power within the 2 MHz wide C/A code bandwidth is

$$P_{\mathrm{N}} = 10 \log kTB = -174 + 63 \, \mathrm{dBm} = -111 \, \mathrm{dBm} \tag{4.1}$$

using the well know relation $kT = -174$ dBm/Hz at ambient temperature. Thus, the signal power is about 20 dB lower than the noise power within the C/A code bandwidth. At least 100 dB of voltage gain is necessary before quantization. A variable gain amplifier brings the RF voltage up by 30-60 dB to a level where it can be quantized by an off-chip A/D converter. As explained in Chapter 3, the RF signal

Antenna

RF

LNA

CS Amplifier

RF Filter

Buffer

50Ω

TXCO

S/H

VGA

VGA

IF

GPS Back-end

Chip

	LNA	CS Amplifier	RF Filter	Buffer	S/H	VGA	VGA	
Gain per stage	18	7	25		-3	30 - 60		dB
Cumultive Gain	18	25	50		47	77 - 107		dB
Cumulative NF	2.6	2.7	3.2	3.2	3.8	3.8		dB
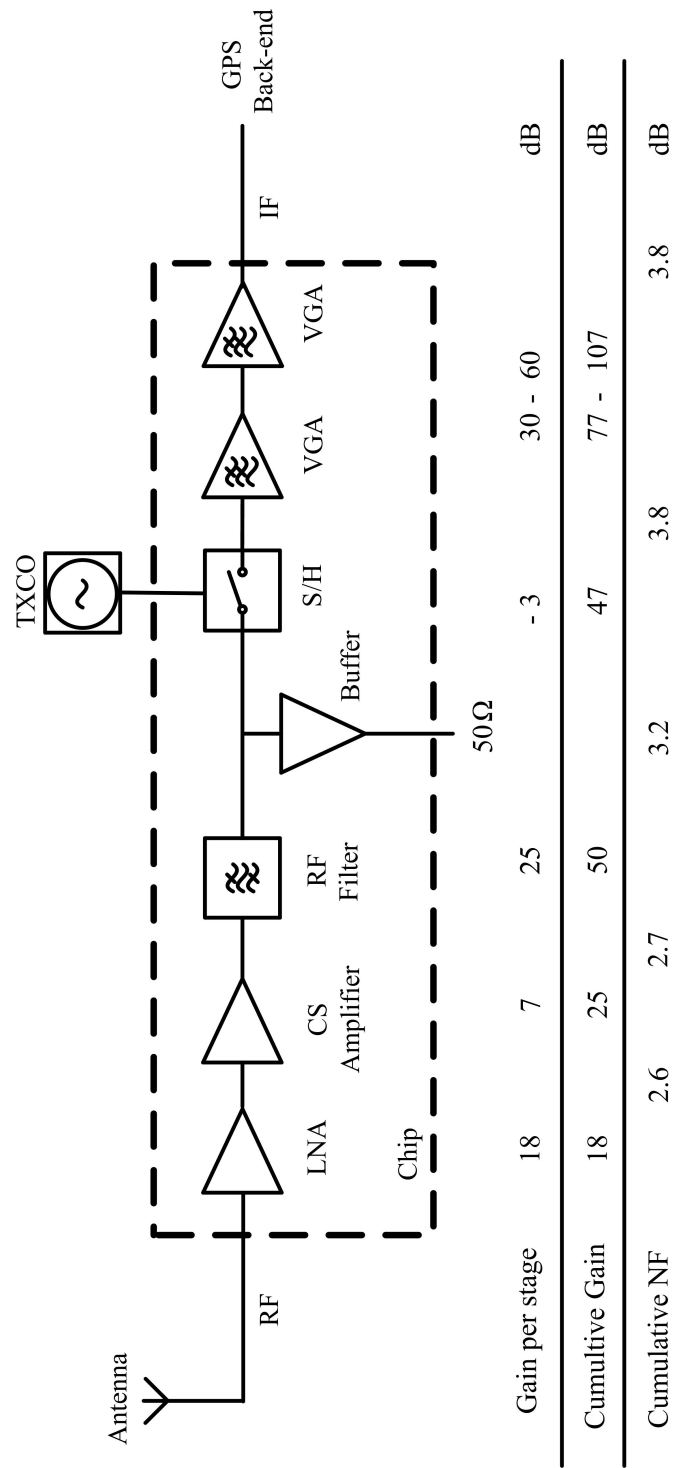
Figure 4.1: Receiver architecture and corresponding voltage gain plan. The table below the figure lists gain per receiver stage, the cumulative gain and NF at the output of each stage. Only the numbers at the output of the RF buffer and at the output of the VGA represent measured quantities. All other quantities are simulation based.

needs to be equal to the full scale range of the ADC. In case of a 1-bit ADC, the signal needs to be significantly larger than the comparator offset. The VGA ensures that the desired signal level is achieved before quantization. The VGA is made of four cascaded ac-coupled folded cascode gain stages providing additional signal gain and IF filtering: The transfer function of the VGA has a low frequency gain of 60 dB and a 3 dB frequency of 20 MHz with a roll-off of -80 dB/decade.

An interesting point is the location of the S/H stage. In conventional sampling architectures the S/H stage is placed right before the quantization stage. This is not practical for a subsampling GPS receiver since the RF signal would be amplified by 100 dB at a single frequency, leading to instability problems due to unwanted parasitic RF coupling effects and spurious mixing products. Parasitic extraction simulations show that the coupling coefficient k for two adjacent bondwires can be significant (k can be as large as 0.25), so that a portion of the RF signal can be coupled to other nodes leading to unexpected effects. In the chosen architecture, the S/H stage and the quantization stage is separated by the VGA. The total gain of 100 dB is distributed over two different frequencies: A gain of approximately 50 dB at the RF from the input of the LNA to the output of the RF filter and another 50 dB at the IF from the output of the S/H stage to the output of the VGA.

4.1.2   Frequency Plan

The frequency plan of the receiver is presented in Figure 4.2. A S/H stage directly samples the GPS L1 carrier at 1575.42 MHz at a rate of 60 MHz, down-converting the signal to an IF of 15.42 MHz. Aliases are spaced about 30 MHz apart: The first alias occurs at 44.58 MHz, the second at 75.42 MHz, the third at 104.58 MHz and so on. As explained in Chapter 3, a higher subsampling frequency improves the noise and interference performance of the receiver at the same time as it increases the power consumption. A lower subsampling frequency leads to higher NFs or more stringent RF filter requirements, and vice versa. The chosen sampling rate of 60 MHz translates into a subsampling ratio of 26.25 and requires a filter bandwidth of roughly 20 MHz to achieve the target NF. A two stage, fourth-order RF anti-aliasing bandpass
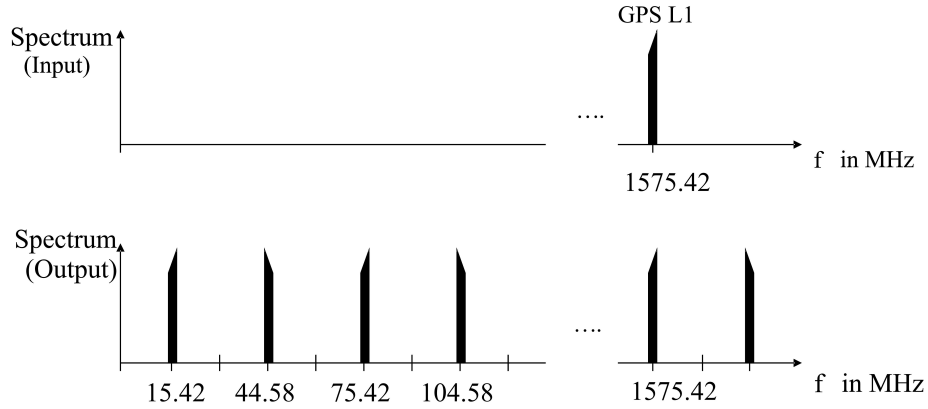
Figure 4.2: Frequency plan of the subsampling GPS receiver. Input is the GPS L1 signal at 1575.42 MHz that is aliased down to 15.42 MHz. The receiver frequency plan also includes the aliases of the downconverted GPS L1 signal.

filter with 20 MHz bandwidth prior to sampling can be practically realized even with moderate Q-enhancement. Therefore, 60 MHz was chosen as optimum sampling rate.

4.2   Low Noise Amplifier

The first stage of the subsampling receiver is a low noise amplifier (LNA) which sets the NF of the RF receiver and provides matching to the input impedance of the antenna.

The LNA is illustrated in Figure 4.3 and based on the well known common source inductively degenerated topology adopted from *Shaeffer and Lee*, [1997] which allows tuning of the input impedance via the source and gate inductors without significantly compromising noise performance. The LNA is designed in a differential fashion to provide better immunity against various sources of noise. An off-chip RF balun[1] performs conversion to the single-ended input of the GPS antenna. Transistor pair M_1 forms the differential input pair that is cascoded by transistor pair M_2 to enhance the gain and output impedance of the LNA, the tail current for the differential pair is provided by current source M_4. The input differential pair M_1 is biased by the resistive

---

[1]Balun from Johanson Technology, 1600BL15B050

Figure 4.3: The LNA is a common source inductively degenerated amplifier stage implemented in a differential fashion. An off-chip RF balun performs single-ended to differential conversion.
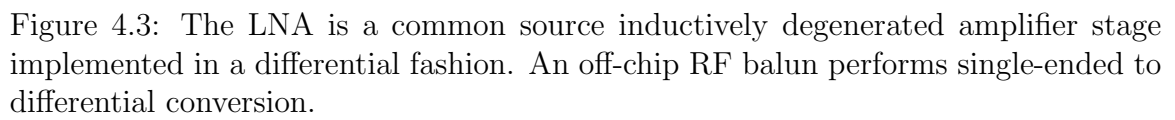
divider R_1 and R_2. The on-chip LC resonant tank made of C_2 and spiral inductor L_2 is tuned to the center frequency of the GPS L1 signal. The input impedance is controlled by the on-chip spiral inductor L_1, the capacitor C_1 and the bondwire inductances at the gates of transistor pair M_1. For practical reasons, the capacitance C_1 was added to fine tune the input impedance without altering the sizing of transistor M_1. This was especially useful for making minor changes after post layout parasitic extraction. In the following, the equations for computing the minimum NF and the input impedance of the common source inductively degenerated LNA are repeated. A simplified single-ended equivalent circuit of the LNA in Figure 4.3 is depicted in Figure 4.4, where the bond pads and the bias circuitry have been omitted. The input impedance of the LNA in Figure 4.4 is given by

$$Z_{\text{in}} = sL_{\text{G}} + \frac{1}{sC_{\text{GS}}} + \frac{g_{\text{m1}}}{C_{\text{GS}}}L_{\text{S}}$$
$$\approx \omega_{\text{T}}L_{\text{S}} \text{ (at resonance)} \tag{4.2}$$

where L_{G} is the gate inductance, L_{S} is the source inductance, g_{m1} the transconductance of transistor M_1, C_{GS} the gate source capacitance of transistor M_1 and ω_{T} is the transit frequency. The real part and the imaginary part of the input impedance Z_{in} in (4.2) can be independently tuned by L_{G} and L_{S}. This allows setting the real part of Z_{in} equal to 50 Ω while resonating out the gate source capacitance of M_1 and thus, the capacitive part of the input impedance.

Optimizing the NF for a given antenna source resistance R_{S} under the constraint of a fixed power consumption, a procedure well explained in [*Shaeffer and Lee*, 1997], the minimum NF is achieved if the input quality factor Q_{L} as defined by

$$Q_{\text{L}} = \frac{\omega_0 \left(L_S + L_G\right)}{R_S} = \frac{1}{\omega_0 R_S C_{GS}} \tag{4.3}$$

takes its optimal value

$$Q_{\text{L,opt}} \approx 3.9 \tag{4.4}$$
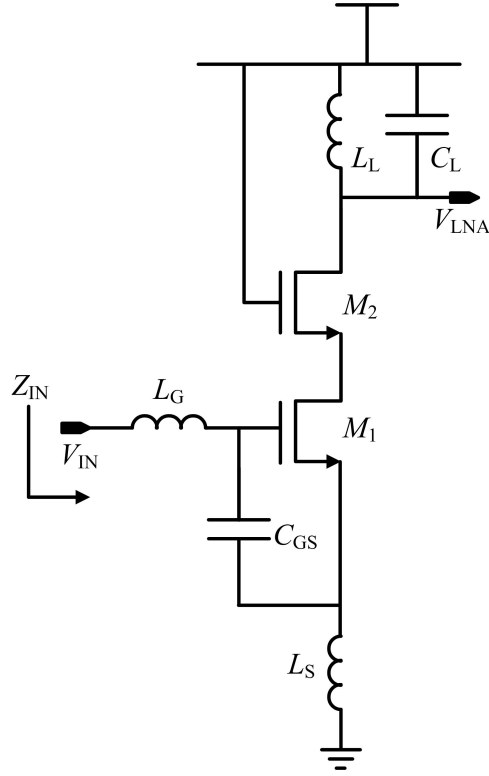
Figure 4.4: Simplified single-ended equivalent circuit of the LNA in Figure 4.3, where the bias circuitry and the bond pads have been omitted.

The minimum NF is then given by

$$F_{\min} \geq 1 + 1.62 \left(\frac{\omega_0}{\omega_{\mathrm{T}}} \right) \tag{4.5}$$

where the equal sign in (4.5) holds only for ideal long channel devices. For short channel devices, the minimum NF is somewhat larger.

This circuit introduces a degree of freedom since the two inductors L_{S} and L_{G} can be independently tuned. This degree of freedom is exploited to achieve near optimum noise performance and the desired impedance match at the input. Near optimum noise performance can be achieved by satisfying (4.4) through tuning the size of transistor M_1 and thus, the gate source capacitance C_{GS}. This fixes the value of the sum of L_{S} and L_{G} in (4.3). At the same time, the desired impedance match

can be obtained by setting $\omega_{\mathrm{T}} L_{\mathrm{S}}$ equal to 50Ω in (4.2). The NF of the amplifier shows only a weak dependence on Q_{L} in the vicinity of $Q_{\mathrm{L,opt}}$.

4.3   Additional Gain Stage

The LNA has a simulated gain of 18 dB, barely sufficient to overcome the input referred noise of the subsequent filter stage. A second amplifier with an output buffer stage as shown in Figure 4.5 was added between the LNA and the filter. The second amplifier stage provides about 7 dB of extra gain and consists of a resistively loaded differential amplifier, followed by a source follower buffer stage. The gain of the additional buffer stage is given by

$$G = g_{\mathrm{m1}} R_3 \frac{g_{\mathrm{m2}}}{sC_{\mathrm{L}} + g_{\mathrm{m2}}} \approx g_{\mathrm{m1}} R_3 \text{ (at lower frequencies)} \tag{4.6}$$

 where g_{m1} and g_{m2} are the transconductances of transistor M_1 and M_2, respectively. C_{L} is the load capacitance of the amplifier stage (not shown in Figure 4.5), which represents the input capacitance of the subsequent RF filter stage. The buffer stage is required to drive the gate-source capacitance of the input transistors of the filter stage.

It should be noted that the additional gain stage reduces the linearity of the GPS receiver, since the input referred compression point of the RF front-end is reduced by the amount of extra gain provided by the additional amplifier stage. This degradation of linearity, however, can be tolerated since the extra gain is only 7 dB.

4.4   Double Notch RF Filter

4.4.1   LCC Notch Filter Resonant Tank

The RF filter is based on the elementary LCC series parallel resonant tank depicted in Figure 4.6. Such LCC resonant tank is often employed in notch filter architectures

Figure 4.5: Additional amplifier stage to provide some extra gain to overcome the input referred noise floor of the subsequent RF filter. The gain stage includes a common source differential pair followed by a source follower buffer stage.

to filter out certain frequency bands or to suppress interference arising from adjacent channels [*Vallese et al.*, 2009]. Assuming perfectly lossless inductors, the input impedance of the LCC notch filter resonant tank as depicted in Figure 4.6 is given by

$$Z_{\text{in}} = \frac{1 + s^2 L_1 \left(C_2 + C_1\right)}{s C_1 \left(1 + s^2 L_1 C_2\right)} \tag{4.7}$$

(4.7) can be rewritten as

$$Z_{\text{in}} = \frac{1 + s^2/\omega_{\text{z}}^2}{s C_1 (1 + s^2/\omega_{\text{p}}^2)} \tag{4.8}$$
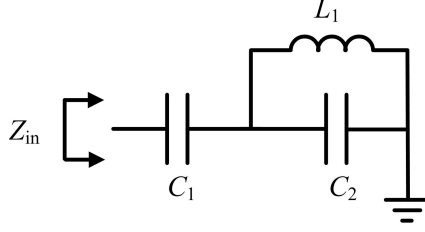
Figure 4.6: Elementary LCC resonant tank circuit implemented in the RF double notch filter. The input impedance exhibits a closely spaced zero and pole creating a steep transition region.

with zero and pole frequencies of

$$\omega_z = 2\pi f_z = \frac{1}{\sqrt{L_1(C_1 + C_2)}} \tag{4.9}$$

$$\omega_p = 2\pi f_p = \frac{1}{\sqrt{L_1 C_2}} \tag{4.10}$$

Thus, the input impedance has a pole at frequency f_p and a zero at frequency f_z. If $C_1 \ll C_2$ in (4.9) the pole is directly adjacent to the zero creating a steep transition region between the zero and the pole in the plot of the input impedance Z_{in}.

This brings up a valid question: How steep can the slope of the transition region become? In the case of perfectly lossless inductors (an assumption used in the derivation of (4.8)) every desired slope can be achieved by moving the location of the zero closer to the location of the pole. In reality, on-chip spiral inductors in modern CMOS processes are inherently lossy due to eddy currents induced in the semiconductor substrate and due to finite metal sheet resistance. This limits the maximum achievable slope of the transition region between the zero and pole as it will be shown in the following analysis.

The impedance of a lossy inductor can be modeled by a lossless inductor L_1 plus series resistor R_s. The input impedance of such an inductor is given by

$$Z_{ind,lossy} = R_s + sL_1 \tag{4.11}$$

Replacing the ideal lossless inductor with impedance sL_1 in (4.7) with a lossy inductor

with impedance $sL_1 + R_s$ leads to

$$Z_{\text{in}} = \frac{1 + s^2 L_1 (C_2 + C_1) + sR_s (C_2 + C_1)}{sC_1 (1 + s^2 L_1 C_2 + sR_s C_2)} \tag{4.12}$$

The inductance L_1 can be related to the series resistance R_s by introducing the quality factor Q of the spiral inductor,

$$Q(\omega) = \frac{\omega L_1}{R_s} \tag{4.13}$$

The Q-factor of the spiral inductor evaluated at the zero frequency ω_z is given by

$$Q(\omega_z) = \frac{\omega_z L_1}{R_s} = \frac{1}{R_s} \sqrt{\frac{L_1}{C_1 + C_2}} \tag{4.14}$$

whereas the Q-factor of the spiral inductor evaluated at the pole frequency ω_p is given by

$$Q(\omega_p) = \frac{\omega_p L_1}{R_s} = \frac{1}{R_s} \sqrt{\frac{L_1}{C_2}} \tag{4.15}$$

The Q-factor of the spiral inductor exhibits only a weak frequency dependency up to frequencies of several GHz. Since the relative location of ω_p and ω_z is within a couple MHz, while the absolute value of ω_p and ω_z is at 1.575 GHz, a valid approximation is to set $Q = Q(\omega_p) = Q(\omega_p)$. Therefore, equation (4.7) can be rewritten in the following form

$$Z_{\text{in}} = \frac{1 + s^2/\omega_z^2 + s/(Q\omega_z)}{sC_1 (1 + s^2/\omega_p^2 + s/(Q\omega_p))} \tag{4.16}$$

Using $s = j\omega = j2\pi f$ the input impedance Z_{in} is in the form of $N(\omega)/D(\omega)$. Both the numerator $N(\omega)$ and the denominator $D(\omega)$ of Z_{in} in (4.16) possess the equation of a second-order bandstop filter with quality factor Q and resonance frequency ω_p and ω_z, respectively. Therefore, the methods used in conventional filter design can be applied to analyze to input impedance Z_{in}. The numerator $N(\omega)$ is the equation of a second order bandstop filter transfer function with center frequency ω_z. The bandwidth of the filter transfer function of $N(\omega)$ is controlled by Q.

Neglecting the part sC_1 (which introduces a pole at zero), the denominator $D(\omega)$ also exhibits a second order Butterworth filter characteristic with center frequency
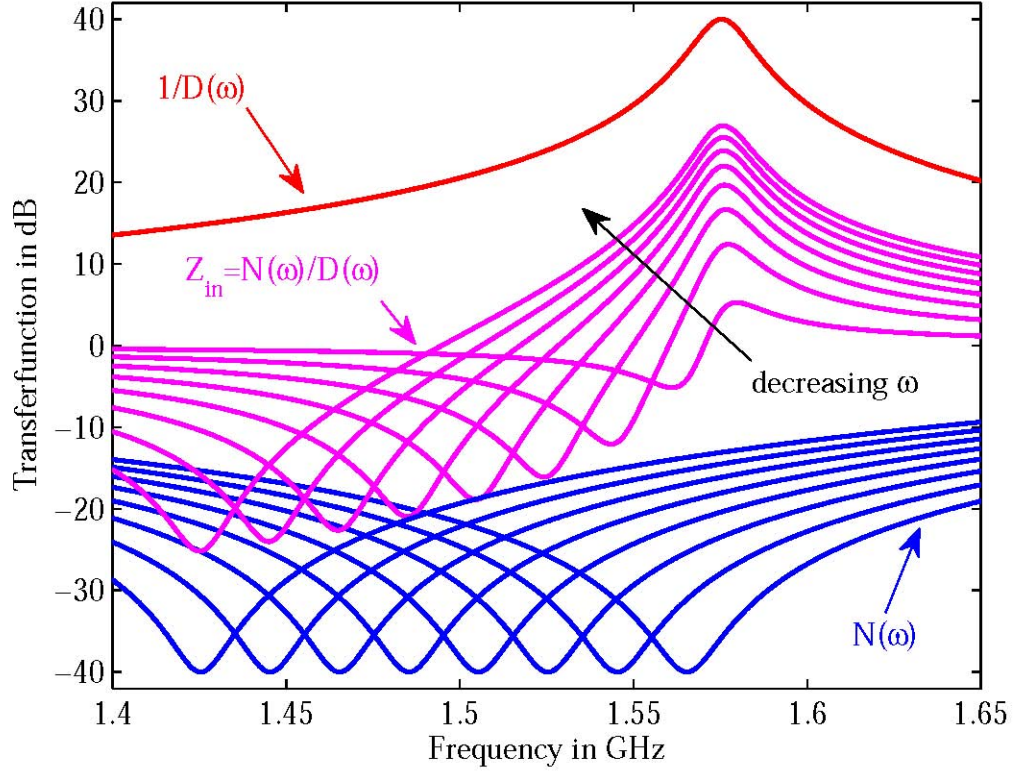
Figure 4.7: Magnitude of the input impedance $Z_\text{in} = N(\omega)/D(\omega)$, numerator $N(\omega)$ and the inverse of the denominator $1/D(\omega)$ in dB versus frequency. The quality factor Q is pinned to 100, while the zero frequency $f_\text{z} = \omega_\text{z}/2\pi$ in $N(\omega)$ is swept in negative steps of 20 MHz starting at 1570 MHz; the pole frequency $f_\text{p} = \omega_\text{p}/2\pi$ in $D(\omega)$ remains at the GPS L1 center frequency of 1575 MHz. The steepness of the slope of the transition region of $Z_\text{in} = N(\omega)/D(\omega)$ between the zero and the pole increases as the zero approaches the pole. At the same time, the range of the transition (in dB) region of Z_in in Y-direction decreases.
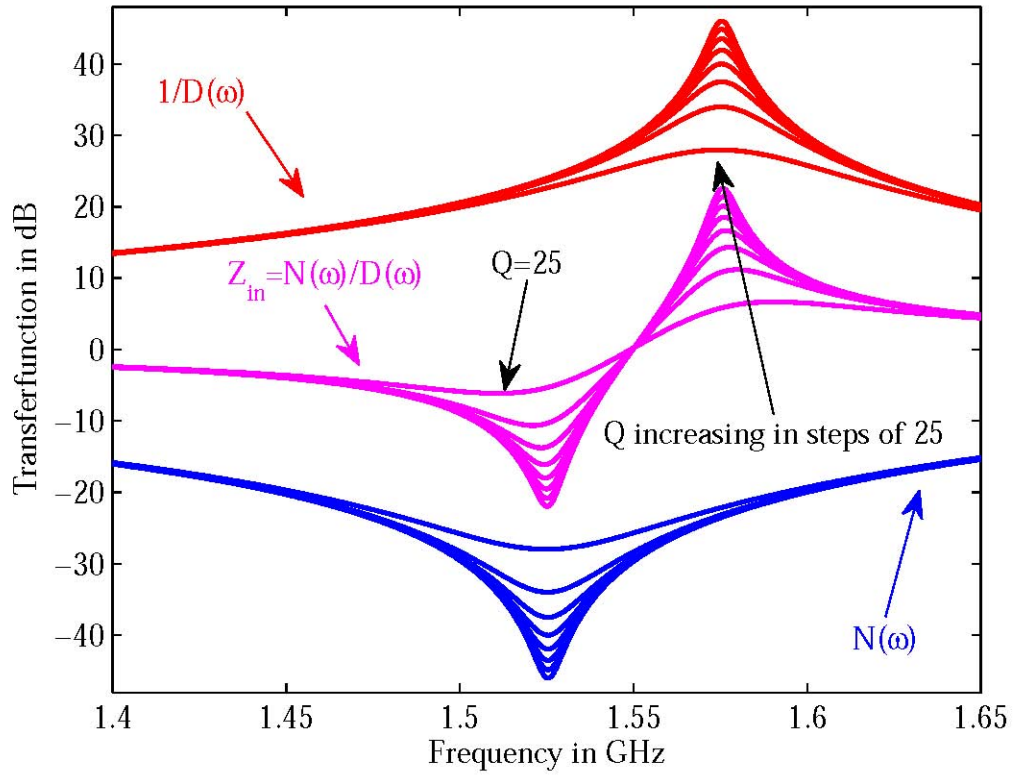
Figure 4.8: Magnitude of the input impedance $Z_{\text{in}} = N(\omega)/D(\omega)$, numerator $N(\omega)$ and the inverse of the denominator $1/D(\omega)$ in dB versus frequency. The quality factor Q is swept from 25 to 200 in steps of 25, while the zero frequency $f_{\text{z}} = \omega_{\text{z}}/2\pi$ in $N(\omega)$ is kept at 1525 MHz and the pole frequency $f_{\text{p}} = \omega_{\text{p}}/2\pi$ in $D(\omega)$ at the GPS L1 center frequency of 1575 MHz. The steepness of the slope of the transition region of Z_{in} between the zero and the pole but even more so the range of the transition region increases with the quality factor Q.

ω_p; therefore $1/D(\omega)$ is the inverse of the transfer function of $D(\omega)$ and exhibits bandpass behavior. Again, the bandwidth of the denominator transfer function is set by the quality factor Q of the spiral inductors. This is demonstrated in Figure 4.7 and Figure 4.8, where the magnitude of $N(\omega)$ and $1/D(\omega)$ is plotted in dB. The magnitude plot of $Z_\mathrm{in} = N(\omega)/D(\omega)$ is found on the log-scale plot simply by adding the magnitude plots of $N(\omega)$ and $1/D(\omega)$. In both figures, the pole frequency $f_\mathrm{p} = \omega_\mathrm{p}/2\pi$ is pinned to the GPS L1 center frequency of 1575 MHz. In Figure 4.7, the quality factor Q is kept constant and equal to 100 while the zero frequency $f_\mathrm{z} = \omega_\mathrm{z}/2\pi$ of $N(\omega_\mathrm{z})$ is swept in negative steps of 20 MHz starting at 1.570 MHz. In Figure 4.8 the pole frequency is kept at 1575 MHz and the zero frequency at 1525 MHz, while the quality factor Q is swept from 25 to 200 in steps of 25.

It can be seen from Figure 4.7 that the slope of the transition region between the zero and the pole of $Z_\mathrm{in} = N(\omega)/D(\omega)$ indeed becomes steeper as the zero frequency moves closer to the pole frequency. However, as the pole frequency increases, the range in dB of the transition region (in Y-axis direction) decreases: Less attenuation is achieved at the zero frequency and less gain is achieved at the pole frequency. To counter this effect the transition region can be increased by increasing the Q-factor as illustrated in Figure 4.8. To keep the range in dB of the transition region constant, the Q-factor has to be increased as the zero moves closer to the pole. Overall, it becomes clear that the steepness of the transition region is limited by the achievable Q-factor of the spiral inductors.

4.4.2   Q-Enhancement of the Spiral Inductors

The on-chip spiral inductors are lossy due to the finite metal resistance of the inductor windings and due to substrate loss from induced eddy currents; in fact, the quality factor Q of the spiral inductors in the 130 nm BiCMOS process is below 20. To increase the Q of the inductors in (4.16), a technique called Q-enhancement is applied in [*Georgescu et al.*, 2006] and [*DeVries and Mason*, 2002].

The series loss resistance of a spiral inductor can be transformed into a parallel loss resistance by the well-know series-parallel impedance transformation $R_\mathrm{p} = R_\mathrm{s}(1 + Q^2)$.
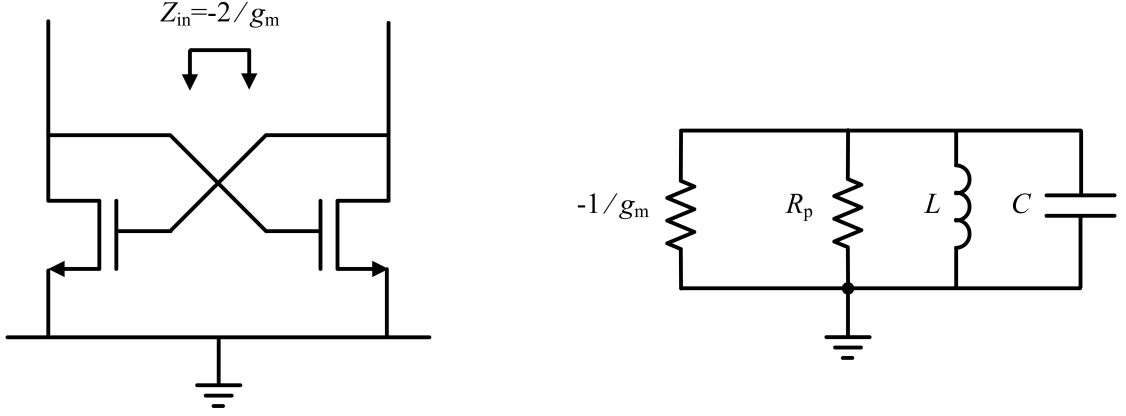
Figure 4.9: Cross coupled differential pair exhibits a negative input impedance of $-2/g_{\mathrm{m}}$; half of the impedance $-1/g_{\mathrm{m}}$ is applied across each LC resonant tank in the RF filter to cancel out part of the loss resistance of the spiral inductors and to enhance the quality factor Q as shown on the right side of the picture.

The Q-factor can be enhanced by placing a negative resistance in parallel with the parallel loss resistance R_{p}. Such a negative resistance is created by a cross-coupled differential transistor pair as depicted in Figure 4.9. Small signal analysis reveals the input impedance of the cross-coupled pair $Z_{\mathrm{in}}=-2/g_{\mathrm{m}}$. If applied in a differential fashion, $-1/g_{\mathrm{m}}$ is placed in parallel with each LC tank and therefore in parallel with the loss resistance as illustrated on the right side in Figure 4.9. The resulting Q-enhanced quality factor becomes

$$Q(\omega) = \frac{R_{\mathrm{p}} \left\| \dfrac{-1}{g_{\mathrm{m}}}\right.}{\omega_{\mathrm{z}} L} = \frac{Q_{\mathrm{unenhanced}}}{1 - g_{\mathrm{m}} R_{\mathrm{p}}} \qquad (4.17)$$

The enhanced Q can be controlled via the transconductance of the cross-coupled pair, which in turn can be controlled via the tail current.

A limitation is the fundamental tradeoff between linearity, noise and the level of Q-enhancement of the RF filter. This sometimes prevents the use of active Q-enhancement in some applications. The total integrated noise power at the output of

a Q-enhanced resonator is given by [*Wiser*, 2008]

$$\overline{v_{\mathrm{nT}}^2} = kT(\gamma + 1) \cdot \sqrt{\frac{L}{C}} \cdot \omega_0 \frac{Q}{Q_0} \tag{4.18}$$

where Q_0 is the unenhanced quality factor of the spiral inductor and $\omega_0 = 1/\sqrt{LC}$ the resonance frequency of the LC tank in Figure 4.9. γ is the coefficient of channel thermal noise ($\gamma = 2/3$ for long channel devices). The maximum voltage swing at the output of the Q-enhanced resonator is limited by the output voltage v_{max} at the 1 dB compression given by [*Wiser*, 2008]

$$v_{\mathrm{max}} = \frac{0.494}{K_{\mathrm{N}}\sqrt{\frac{L}{C}}} \sqrt{\frac{1}{QQ_0}} \tag{4.19}$$

where $K_{\mathrm{N}} = \mu C_{\mathrm{ox}} W/L$ depends on the transistor width W and length L, as well as on the electron mobility μ and the gate oxide capacitance per unit area C_{ox}.

The total integrated output noise power in (4.18) increases with stronger enhancement of the Q-factor of the spiral inductors. Simulations of the Q-enhanced filter indeed lead to a NF of 18 dB, which requires a LNA with sufficient gain to overcome the input referred noise of the second filter stage. For this purpose, a second amplifier with 7 dB of extra gain was placed between the LNA and the RF filter in this receiver.

On the other hand, the output 1 dB compression point is reduced with increasing level of Q-enhancement, as apparent from (4.19). In addition, the 1 dB compression point is further degraded by the gain of the LNA, which needs to be relative high to meet the noise requirements of the system. This factor generally leads to a poor linearity of Q-enhanced filters which poses a major limitation for some applications. Equation (4.19), however, is only valid at the center frequency of the Q-enhanced resonator in Figure 4.9. The linearity quickly improves moving away from the center frequency since the gain of the filter drops sharply away from the center frequency. Thus, only in-band linearity is degraded by Q-enhancement, while out-of-band linearity can still be good. Commercial GPS receivers typically employ 1 to 3-bit A/D

converters to quantize the signal. Reduced in-band linearity can be tolerated for a GPS receiver with low bit quantization since jamming of the receiver back-end occurs at an in-band interference level as low as -110 dBm. Thus, the receiver is jammed already at signal levels significantly below the in-band compression. Therefore, Q-enhanced filters do not pose a major limitation in a GPS receiver front-end.

4.4.3 Double Notch Filter Architecture

The primary goal of the RF filter is to prevent noise folding and noise aliasing and to filter out RF interference close to the center frequency of the RF filter. This is accomplished by a Q-enhanced filter topology based on two Q-enhanced LCC resonant tanks that are described in the previous subsection. The two LCC resonant tanks create a double notch in the transfer characteristic of the filter suppressing interference close to the RF center frequency. The two LCC resonant tanks are employed in a differential fashion to a cascoded amplifier stage. The simplified singled ended cascode circuit in Figure 4.10 shows the basic principle. The Q-enhanced LCC tank serves as load and degeneration impedance of the cascode stage. This way, the desired filter characteristic is produced: A sharp roll-off and a narrow passband.

The impedance of the drain LCC tank at the drain of M_1 shows up in the numerator of the transfer function while the the impedance of the degeneration LCC tank at the source of M_1 shows up in the denominator. Hence, the load LCC tank alone produces a filter transfer characteristic similar to the shape of the input impedance Z_{in2} whereas the source LCC tank alone produces a filter transfer function similar to the horizontally flipped shape of the input impedance Z_{in}. This is illustrated in Figure 4.10 showing the magnitude response of the filter, if only the top LCC tank is applied to the drain of M_1 and if only the bottom LCC tank is applied to the source of M_1. The overall transfer function of the RF filter with both LCC tanks can be found by adding the two transfer functions on the log plot. The transfer function exhibits a notch slightly below and above the RF center frequency: A sharp roll-off is achieved to filter out interference close to the RF center frequency.
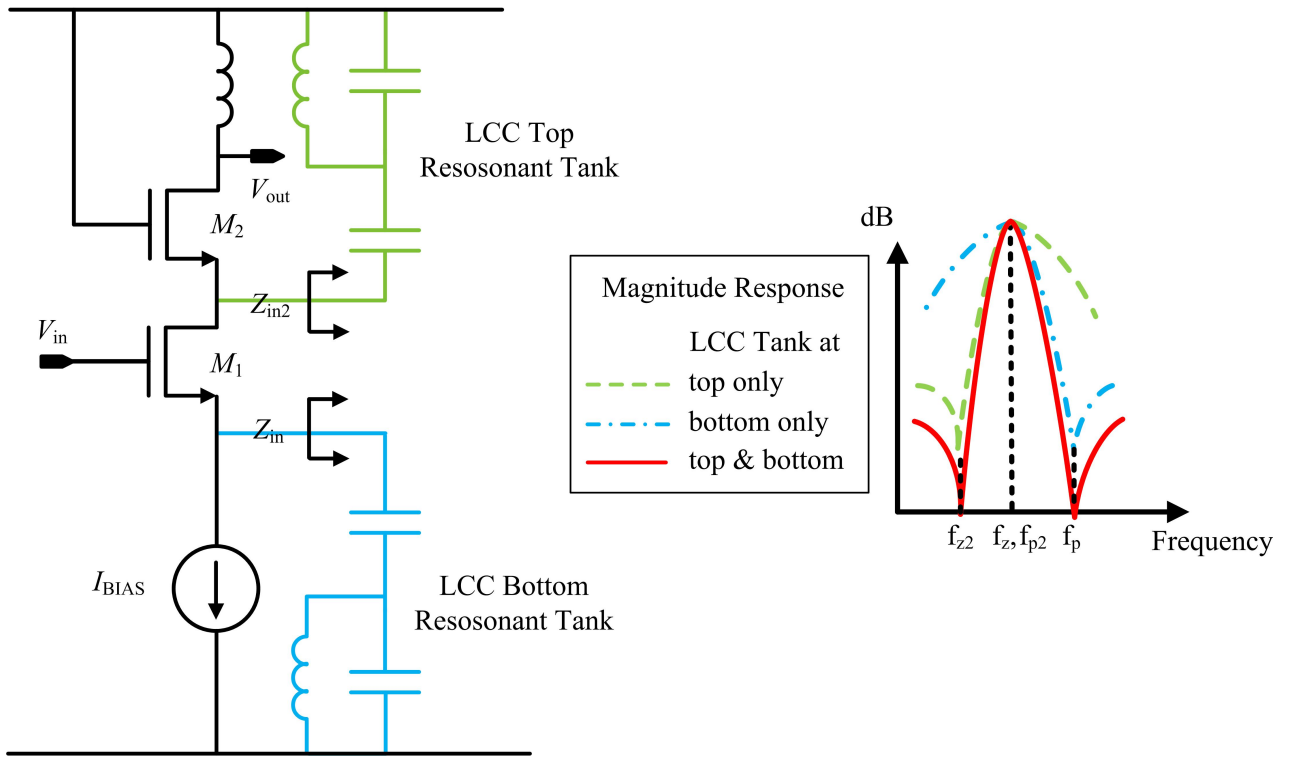
Figure 4.10: Simplified singled-ended schematic of the RF filter based on two of the elementary LCC resonant tank circuits from Figure 4.6. The RF filter consists of a simple cascode stage loaded by the two LCC tanks. The top LCC tank loads the cascode stage, while the bottom LCC tank degenerates the cascode stage. The resulting magnitude response of the RF filter is plotted into the diagram on the right side of the picture.

Figure 4.11: Differential transconductance stage of the double notch RF filter: A Q-enhanced LCC resonant tank controls the desired zeros and poles as illustrated in Figure 4.10

Figure 4.12: Differential transimpedance stage of the double notch RF filter: A Q-enhanced LCC resonant tank controls the desired zeros and poles as illustrated in Figure 4.10
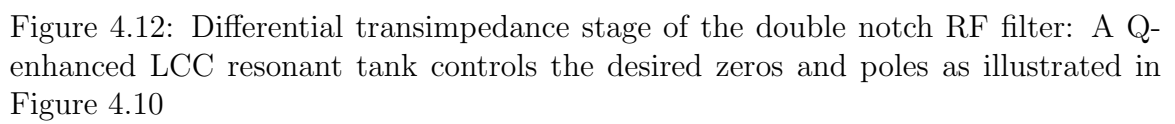
In the following, a more detailed analysis of the RF filter transfer function is performed. The filter is implemented as a single cascode amplifier stage loaded with two LCC resonator tanks. The cascode filter stage can be split up into a transconductance and a transimpedance stage for the ease of analysis. The two stages are displayed in Figure 4.12 and in Figure 4.11, respectively. The LCC resonant tank of the top half of the filter in Figure 4.12 is comprised of C_3, C_4 and L_2. On the other hand, the LCC resonant tank of the bottom half of the filter in Figure 4.11 is comprised of C_1, C_2 and L_1. The LCC resonant tanks are enhanced by the cross coupled differential pairs M_2 and M_4, respectively. R_1 and R_2 at the sources of M_2 and M_4 increase the linearity of the filter by degeneration of the cross coupled differential pairs. M_1 forms the input differential pair that is cascoded by M_3. L_3 is not a Q-enhanced and represents the output load of the filter. I_{gm}, I_{gm2} and I_{FILT} are the biasing currents of the filter that are regulated via current mirrors. The transconductance stage of the filter in Figure 4.11 is degenerated by the LCC filter network. The differential output current of this filter stage is therefore

$$i = i_p - i_n = \frac{g_{m1}}{1 + g_{m1}Z_{in}} v_{in} \tag{4.20}$$

where $v_{in} = V_{AMP+} - V_{AMP-}$.

The transimpedance stage of the filter in Figure 4.12 is loaded by a similar filter network, but with slightly different impedance values. The input impedance Z_{in2} of this LCC network is given by

$$Z_{in2} = \frac{1 + s^2/(2\pi f_{z2})^2}{sC_3(1 + s^2/(2\pi f_{p2})^2)} \tag{4.21}$$

with zero and pole frequencies of

$$f_{z2} = \frac{1}{2\pi\sqrt{L_2(C_3 + C_4)}} \tag{4.22}$$

$$f_{p2} = \frac{1}{2\pi\sqrt{L_2C_4}} \tag{4.23}$$

The differential output voltage $v_\mathrm{out} = V_\mathrm{FILT+} - V_\mathrm{FILT-}$ of the transimpedance filter stage is given by

$$v_\mathrm{out} = sL_3 \frac{g_\mathrm{m3} Z_\mathrm{in2}}{1 + g_\mathrm{m3} Z_\mathrm{in2}} i \tag{4.24}$$

The overall transfer function $v_\mathrm{out}/v_\mathrm{in}$ of the notch filter can be found by inserting (4.20) into equation (4.24)

$$v_\mathrm{out} = \frac{g_\mathrm{m1} g_\mathrm{m3} s L_3 Z_\mathrm{in2}}{(1 + g_\mathrm{m1} Z_\mathrm{in})(1 + g_\mathrm{m3} Z_\mathrm{in2})} v_\mathrm{in} \tag{4.25}$$

The output current in (4.20) of the transconductance stage can be approximated as

$$i \simeq \begin{cases} g_\mathrm{m} v_\mathrm{in} & if \ \ f = f_\mathrm{z} \\ \dfrac{v_\mathrm{in}}{Z_\mathrm{in}} \simeq 0 & if \ \ f = f_\mathrm{p} \end{cases} \tag{4.26}$$

and the output voltage of the transimpedance stage in (4.24) as

$$v_{out} \simeq \begin{cases} sL_3 g_\mathrm{m} Z_\mathrm{in2} i \ \simeq 0 & if \ \ f = f_\mathrm{z2} \\ sL_3 i & if \ \ f = f_\mathrm{p2} \end{cases} \tag{4.27}$$

at the zero and pole frequencies. Thus, the transconductance stage provides a transmission zero at f_p and the transimpedance stage at f_z2. On the other hand, the transfer function of the transconductance stage has a maximum at f_z and the transimpedance stage has a maximum at f_p2, respectively. The relative locations of the zeros and poles of the filter are plotted into Figure 4.10.

It is clear from Figure 4.10 that the zero frequency of the transconductance stage f_z is below the pole frequency stage f_p. Similarly, the zero of the transimpedance stage f_z2 occurs at frequencies below the pole frequency f_p2. The transmission zero, on the other hand, occurs at the zero frequency f_z2 of the transimpedance stage and at the pole frequency of the transconductance stage f_p. This is a direct consequence of equations (4.20) and (4.24). The transimpedance stage in Figure 4.12 is loaded with the LCC resonant tank, thus the pole and zero of the input impedance of the LCC resonant tank are mapped to the same location in the transfer function of the

filter. On the other hand, the transconductance stage is degenerated with the LCC resonant tank. Thus, the pole frequency of the input impedance of the LCC resonant tank is mapped to the frequency where the transmission zero occurs in the transfer function and vice versa. Since, f_z and f_{p2} can be controlled independently, a good choice is to set f_z equal to f_{p2} so that the maximum of the transfer function occurs at $f_z = f_{p2}$ and maximum mid-band filter gain is achieved. Hence, the overall transfer function can be approximated at the zero and pole frequencies as

$$v_{out} \simeq \begin{cases} 0 & if \ f = f_{z2} \ or \ f_{p} \\ g_{max} Z_{max} v_{in} & if \ f = f_z = f_{p2} \end{cases} \qquad (4.28)$$

g_{max} and Z_{max} can both be controlled by the Q-factor of the inductors. The roll-off of the filter on both sides of the center frequency can be controlled by the location of the poles and zeros and by the enhanced quality factor Q of the spiral inductors and thus, as explained in the previous subsection, by the current flowing through the cross-coupled transistor pair.

The double notch filter can be created in the following fashion. First, the location of the zeros and poles is determined. If $C_3 \ll C_4$ and $C_1 \ll C_2$ in equations (4.9) and (4.10) then f_z and f_p as well as f_{z2} and f_{p2} are directly adjacent (the frequency of the zero is slightly lower than the frequency of the pole), so that a steep filter roll-off can be achieved. Then, the Q of the inductors is increased to obtain adequate g_{max} and Z_{max}. To achieve a symmetrical filter characteristic and maximum mid-band gain, it is desirable to set $f_z = f_{p2}$.

4.5   Sample and Hold Stage

The sample and hold stage that subsamples the RF signal with a sampling rate of 60 MHz is depicted in Figure 4.13 with corresponding clock signals in Figure 4.14. Downconversion of the RF signal to IF is achieved by aliasing. The charge cancelation used in the S/H stage was adopted from [*Eichenberger, Guggenbuhl*, 1989]. During tracking phase when p_{1b} is low and p_1 is high, transistor M_1 is on and the input signal V_{in} is sampled. Then, p_{1b} turns high, transistor M_1 turns off and the signal is hold
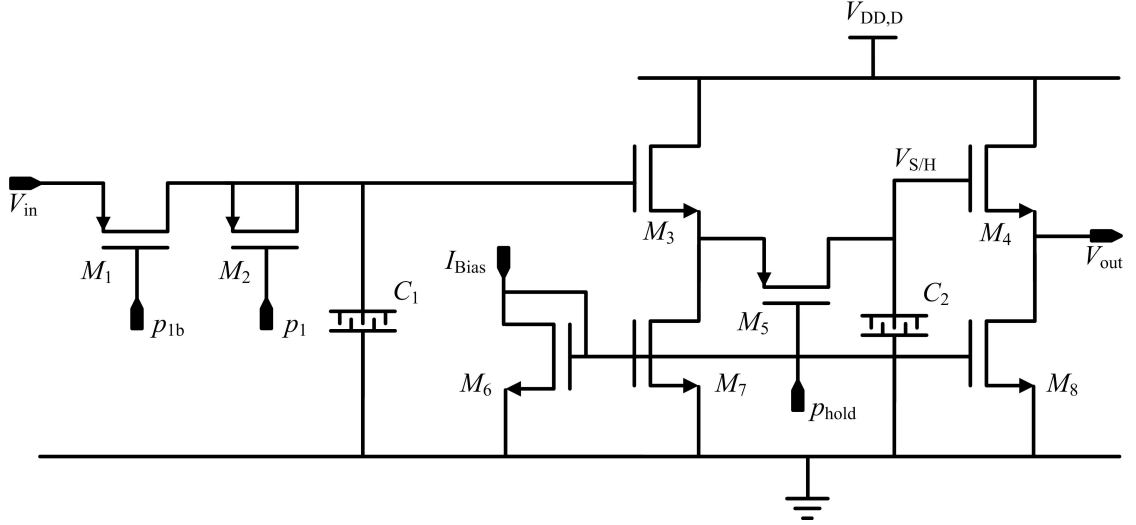
Figure 4.13: Sample and hold stage of the subsampling GPS receiver that down-converts the RF signal to IF frequency by subsampling with a sampling rate of 60 MHz.

across capacitor C_1. A second transistor M_2 that is driven by the inverse clock p_1, cancels the charge injected by M_1. The signal V_{in} and the signal across capacitor $V_{S/H}$ is illustrated in Figure 4.15.

Even though the sampling rate is below 100 MHz, the sample and hold stage needs to have enough input referred bandwidth to accommodate the RF carrier frequency of 1575.42 MHz. The input referred bandwidth of the S/H stage is determined by the sampling capacitor C_1 and the on-resistance of the PMOS sampling switch M_1 in Figure 4.13. The capacitance C_1 is chosen to satisfy the noise requirements of the system. The total integrated noise at the output of the sample and hold stage across capacitance C_1 is kT/C_1. Alternatively, as demonstrated in the previous chapter, the spot noise figure at the output of the S/H stage can be calculated by summing over all noise components aliased down to the IF. The noise components introduced by the S/H stage appear as higher order terms in the modified Friis Equation. As explained in Chapter 3, the LCC bandpass filter needs to provide enough gain to cancel the higher order terms in the Friis Equation resulting from lowpass filtered aliased noise introduced by any other stage between the bandpass filter and the S/H stage.
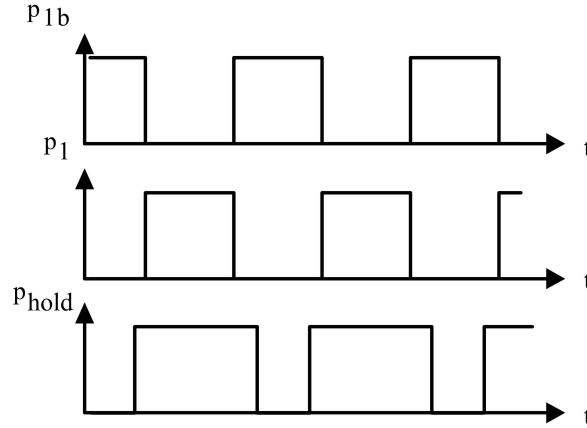
Figure 4.14: Clock timing of the signals from Figure 4.13.

Nonlinearities introduced by the signal dependent on-resistance of M_1, by clock feedthrough or by other sources are not canceled. Simulations show that the output SFDR of the differential S/H stage was above 30 dB which is more than sufficient for GPS.

The spectrum of the signal $V_{S/H}$ across capacitance C_1 contains undesired RF components, which are amplified by the subsequent VGA. To filter out the undesired RF content the signal across capacitor C_1 is buffered by transistor M_3 and a second S/H stage made of transistor M_5 and capacitor C_2 samples the signal buffered by transistor M_3 during the hold phase of M_1. The resulting signal is buffered by transistor M_4. The output signal V_{OUT} is plotted into Figure 4.15 which is perfectly zero-order hold with no RF components in its spectrum. Thus, the second stage effectively acts as filter for RF components that are present in $V_{S/H}$.

4.6   Variable Gain Amplifier

The signal after the sample and hold stage is still too small for quantization. If a multi-bit ADC is used, the signal has to be amplified to cover the full scale range of the ADC. This is important in the presence of changing atmospheric conditions that cause variations of the GPS signal strength at ground level. In case of a 1-bit ADC (a simple comparator) the amplified signal needs to be significantly larger that the offset
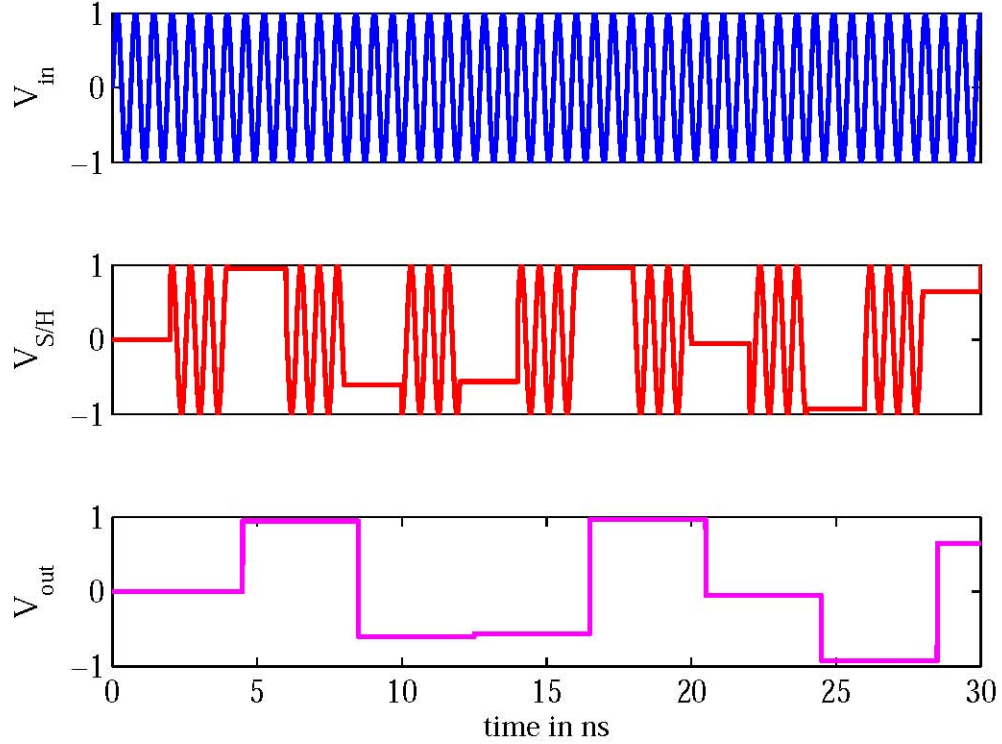
Figure 4.15: Input and output signals of the S/H stage from Figure 4.13.

of the comparator. In contrast to the multi-bit ADC solutions, a fixed amount of gain can be used for 1-bit quantization. Since only the zero crossings of the differential signal are detected, the signal can be amplified to the point where clipping occurs. Thus, the VGA can be regarded as limiting amplifier for the 1-bit case.

The VGA is comprised of four cascaded amplifier stages, each amplifier stage is based on the differential folded cascode architecture depicted in Figure 4.16. Transistors pair M_3 comprises the differential input, while M_5 to M_8 form the cascode stage. Since the amplifier is fully differential, the common-mode output voltage is set by negative feedback. This is accomplished by a differential pair made of transistors pair M_9. Through negative feedback, the common-mode output voltage is forced to be equal to half the supply voltage set by the divider R_3 and R_4. The gain of the VGA is controlled by M_4 which is driven into the linear region. The gain can be set

by the gate source voltage of M_4 and can be controlled from off-chip. Small signal analysis reveals that the gain of the VGA is given by

$$G \approx \frac{g_{\mathrm{m3}} r_{\mathrm{ds4(on)}}}{g_{\mathrm{m7}} r_{\mathrm{ds4(on)}} + 1} g_{\mathrm{m7}} r_{\mathrm{out}} \tag{4.29}$$

where $r_{\mathrm{ds4(on)}}$ is the drain source resistance of M_4 driven into the linear region and r_{out} is the output resistance of the folded cascode. Although not explicitly derived, r_{out} is comprised of the output resistances of M_5 to M_8 as well as R_1 and R_2. g_{m3} and g_{m7} are the transconductances of M_3 and M_7. As it can be seen, the gain depends on $r_{\mathrm{ds4(on)}}$ which can be modulated by the gate voltage of M_4. The VGA provides additional 30 – 60 dB of gain and has a 3 dB frequency of 20 MHz with a roll-off of -80 dB/decade, enough to accommodate the IF signal at 15 MHz.
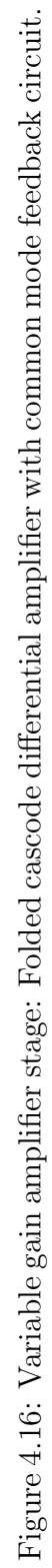
4.7   Buffer Stage and Clocking Circuit

Not covered in the previous chapters is the buffer stage and the clocking circuitry. The buffer stage is made of an AC coupled bipolar emitter follower. The output impedance of the buffer stage is 50 Ω to provide matching between the high impedance node at the output of the RF filter and the test and measurement equipment. It should be noted that the buffer has a voltage gain of -20 dB when connected to a 50 Ω load.

Another circuit not covered so far is the clock buffer, which is made of a series of inverters, NANDs and delay lines with capacitive loading. This circuit provides the three clock signals p_1, p_{1b} and p_{hold} needed in the S/H stage. These clock signals are derived from an external clock.

4.8   Filter Tuning

In the presence of mismatch and process variations, some postfabrication trimming of the RF filter is necessary before the operation of the circuit. To figure out, which elements of the filter need tuning, a qualitative sensitivity analysis is presented first.

Since $C_1 << C_2$ and $C_3 << C_4$ in Figure 4.12 and Figure 4.11, any mismatch of C_1

Figure 4.16: Variable gain amplifier stage: Folded cascode differential amplifier with common mode feedback circuit.

and C_3 will hardly affect the center frequency of the filter as it can be seen from (4.10), (4.23), (4.9) and (4.22). It will slightly move the zero and pole in Figure 4.10, altering the filter roll-off slightly, which can be tolerated for the subsampling application. Even if C_1 or C_3 are off by a significant percentage from its desired nominal value the conditions $C_1 << C_2$ and $C_3 << C_4$ ensure that the location of the zeros and poles are hardly affected. Since C_2 is approximately equal to C_4, a small capacitance can be added to a capacitance of the size of C_2 to create C_4, relying on matching properties for the larger capacitances. However, the absolute value of C_2 or C_4 is affected by process variations which requires a tuning step to properly set the center frequency of the RF filter.

To ensure that the cross-coupled differential pairs in the Q-enhanced resonators provides the desired amount of negative resistance, tuning of the Q-factor of the filter becomes necessary, too. This is accomplished by varying the currents I_{gm} and I_{gm2} in Figure 4.12 and Figure 4.11 and thus the tail current sources of the cross coupled pairs. Again, it can be relied on matching properties between the two cross coupled pairs in Figure 4.12 and Figure 4.11 so that only one current has to be tuned. The other current can be set equal. Overall, the number of tuning steps is limited to two, one to tune the center frequency of the filter by changing C_2 or C_4, and one to tune the Q-factor by altering I_{gm} or I_{gm2}.

Several options to accomplish postfabrication trimming are reported in the literature. Examples are electrically programmable metal or poly fuses [*Gebreselasie et al.*, 2007], [*Clein*, 2000], zener zapping or oxide zapping [*Teichmann et al.*, 2003] and the use of programmable ROM. Automated tuning schemes can be applied that run in the background and measure the signal path and adjust the zeros and poles of the filter. In [*DeVries and Mason*, 2002], the tuning scheme measures the magnitude response of the filter by applying white noise at the input of the filter. Then, the filter parameters are set by digital signal processing. Another option is reported in [*Liu and Karsilayan*, 2002] and [*Wiser*, 2008], where the magnitude response of the filter is measured at different frequency points which is then used to extract and correct the Q and the center frequency of the filter. In [*Nakaska*, 2007], an automated tuning scheme is proposed driving the Q-enhanced resonators into oscillation by increasing

the absolute value of the negative resistance. The oscillator frequency is then tuned to the correct location and the absolute value of the negative resistance is reduced until the oscillation disappears.

For simplicity and proof of concept of the subsampling receiver, an off-chip tuning scheme based on the approach reported in [*Liu and Karsilayan*, 2002] and [*Wiser*, 2008] was performed. In this implementation, C_2 and C_4 are varactors that can be tuned by an external voltage and I_{gm} and I_{gm2} by an external current. The magnitude response of the RF filter is measured at different frequency points. This information is then used to correct the center frequency and the Q-factor of the filter. An interesting observation was that postfabrication trimming had to be performed only once since the magnitude transfer characteristic remained stable over time.

4.9 Chip Layout

The subsampling GPS receiver chip was fabricated in a 130 nm BiCMOS process from National Semiconductor. A die photograph is shown in Figure 4.17. Only CMOS transistors are used in the chip except for the test buffers that match the high impedance at the output of the filter to the 50 Ω impedance that is required by most test equipment. The chip is organized so that the sensitive analog sections are physically separated from the clock circuitry and the digital parts. Several factors complicate the layout of the receiver chip. Parasitic capacitive coupling can create a signal path from the switched circuit parts to the LNA and other sensitive analog parts which can create harmonic distortion products. Another effect is the capacitive coupling of oscillator harmonics ending up at the output of the filter. These harmonics are sampled by the S/H stage ending up as DC offset in the IF spectrum. These effects can be countered by using near minimum signal trace width in several locations of the RF path after the LNA and the filter. This naturally increases the series resistance of the RF path but can be tolerated in most cases. The layout in the vicinity of the Q-enhanced spiral inductors is particularly critical. Since the Q-enhancement creates an oscillatory current in the LC resonant tank that is Q times higher than the current outside of the LC loop, the series resistance of the metal in the LC

resonant loop needs to be extraordinarily small. For that reason, a thick top metal layer provided by the process is used for the Q-enhanced sections. The substrate resistance of the non-epi process is relatively high so that substrate noise is of a lesser concern. Nevertheless, the sensitive analog parts were spaced as far away as possible from the digital circuitry. Noise effects were further countered by building a strictly differential architecture. The LNA at the input of the chip employs four spiral inductors as depicted Figure 4.17. Also, the six spiral inductors of the RF filter can be easily located in the picture.
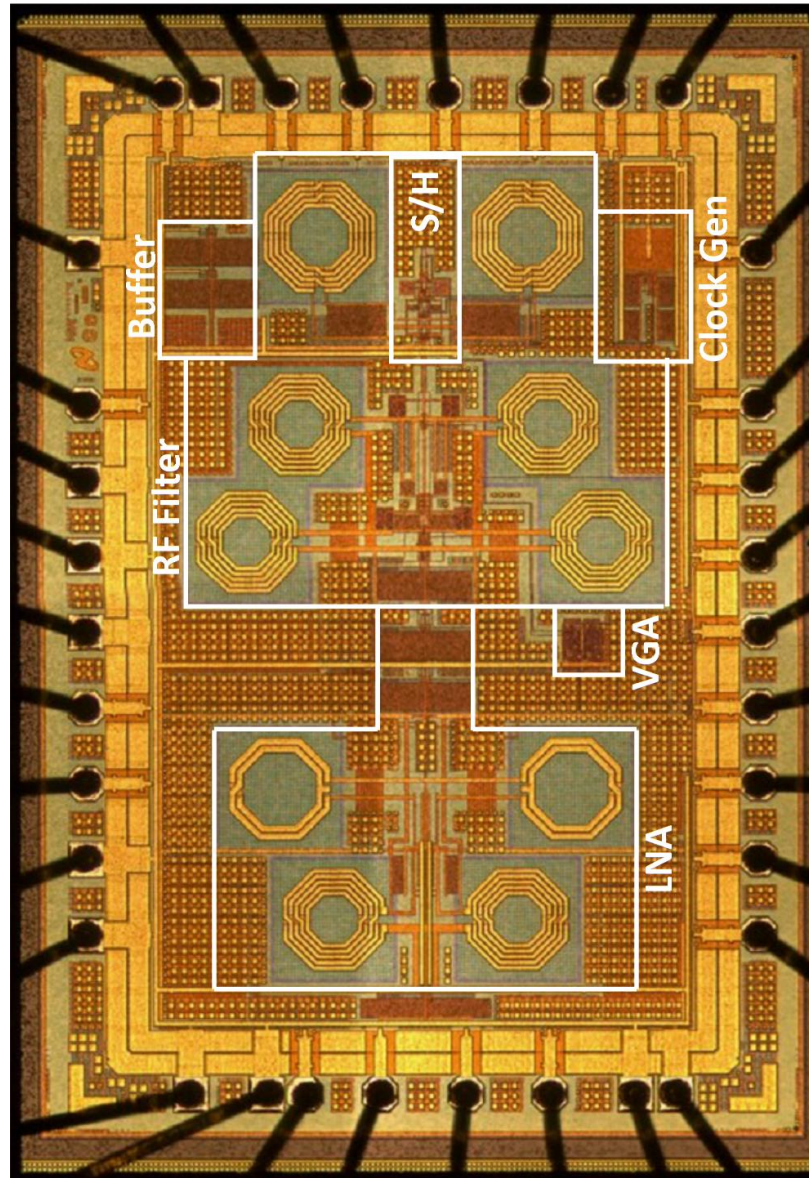
Figure 4.17: Die photograph of the subsampling GPS receiver front-end. The chip was fabricated in a 130 nm BiCMOS process from National Semiconductor

Chapter 5

Measurement Results

The GPS receiver was measured at a laboratory facility of National Semiconductor in Santa Clara, California. In this chapter, the measured figures of merit of the GPS receiver such as NF, S-parameters, total receiver gain, linearity, blocking performance and power consumption are presented.

The chapter begins with a brief discussion of the test setup and an overview of the test equipment. Several photographs of the measurement equipment and the laboratory environment are displayed in the first section. In the next section, the S-parameters of the RF filter are reported including the receiver input return loss. Then, the NF (one of the most important figures of a GPS receiver) is investigated. The NF directly affects the ranging precision of the GPS receiver and should be significantly below 5 dB. As discussed in Section 3.2, the NF of a subsampling receiver is computed crucially different from the NF of a heterodyne receiver. Due to the S/H operation, aliased out-of-band noise mostly from thermal noise sources can end up within the IF receiver bandwidth, which in turn can lead to higher receiver NFs. To investigate the effect of aliased out-of-band noise on the total receiver NF, measurements were taken before and after subsampling: The NF at the output of the RF filter is presented and compared against the total receiver NF measured at the receiver output. The difference between the two NFs can be attributed to thermal noise aliased to the IF receiver band. The discussion continues with the signal spectrum (the harmonic content of the signal) before and after subsampling. Then, the receiver linearity and

blocking performance is evaluated via the 1 dB compression point. Finally, the GPS receiver front-end is connected to a Matlab based GPS receiver back-end confirming that the implemented prototype is indeed capable of down-converting a real GPS L1 signal to IF.

5.1   Testsetup

The test setup is illustrated in Figure 5.1. Photographs of the measurement equipment are displayed in Figure 5.2 and Figure 5.3, respectively. A photograph of the board with the GPS receiver front-end chip as device under test (DUT) is shown in Figure 5.4. The board has a RF input, a RF testport and an IF output. As depicted in Figure 5.1 the RF testport at the output of the buffer allows for making S-parameter and NF measurements of the cascaded RF building blocks such as the LNA, the common source (CS) amplifier (the additional gain stage) and the RF filter. In some of the following measurements, two different boards with different DUTs are reported. The measurements are labeled "Board #1" and "Board #2" or "DUT #1" and "DUT #2".

The equipment consists of an Agilent N8973A NF meter with a 346A Noise Diode (6 dB excess noise ratio) capable of making NF measurements up to 3 GHz. The network analyzer HP 8753D has a frequency range from 30 kHz to 6 GHz, enough to cover all relevant GPS frequencies. The HP 8449B RF pre-amplifier provides up to 20 dB of gain and has a NF of 8.8 dB and is needed to overcome the instrumentation noise floor of the FSEK30 spectrum analyzer from Rohde and Schwarz.

The sampling clock is provided by the HP signal generator ESG3000A. Alternatively an external 60 MHz crystal oscillator from Abracon with less than 4 ps rms jitter can be connected to the clock input. Finally, the GPS test signal at the RF input is provided by the more sophisticated Vector Signal Generator E4438C from Agilent. The GPS test signal emulates the GPS L1 signal transmitted by space vehicle 1. To create the test signal, a carrier at 1575.42 MHz is modulated with the C/A code transmitted by space vehicle 1, transmitting a 1023 chips long pseudo random number sequence. The signal contains no GPS navigation message.
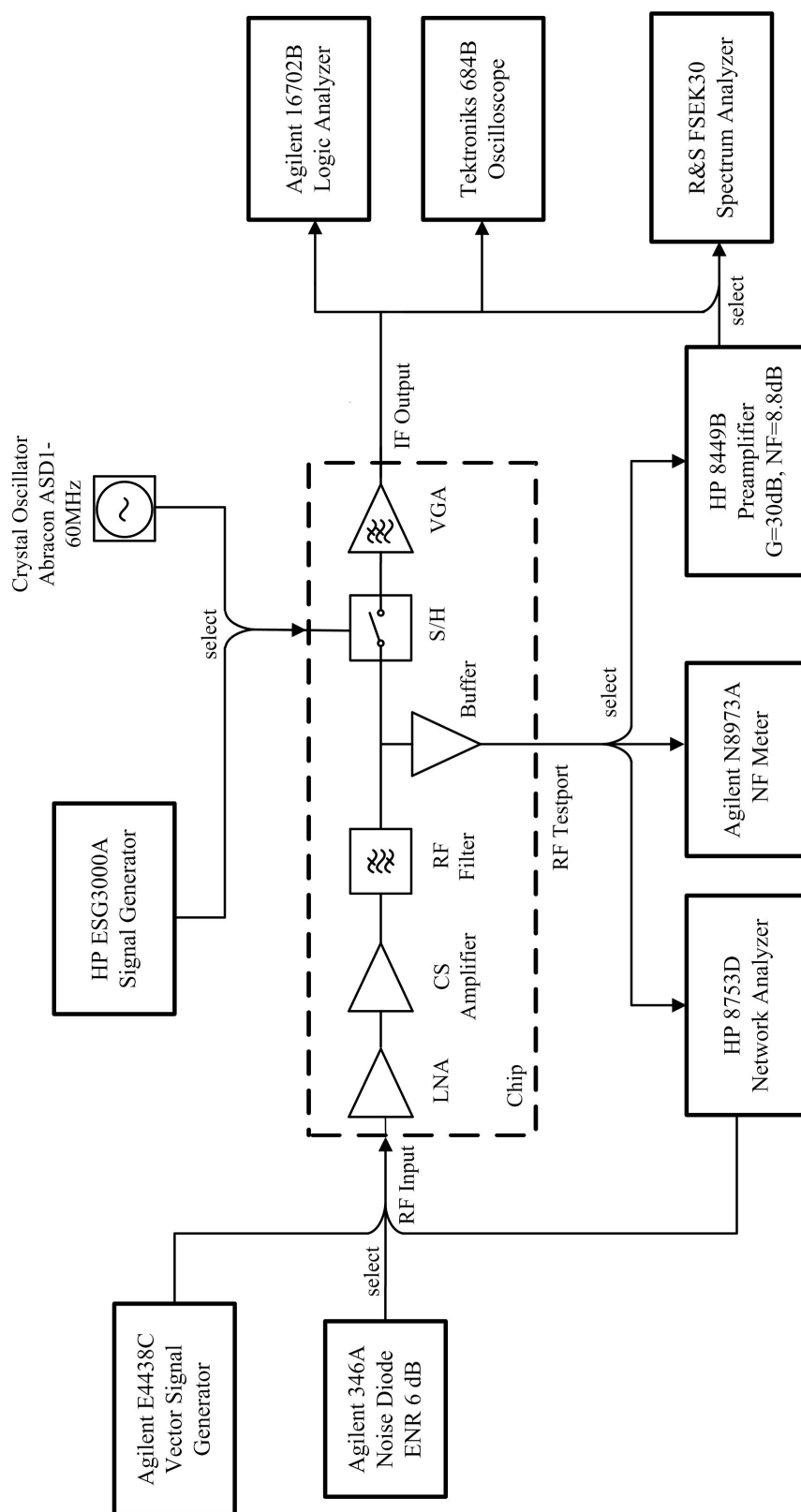
Figure 5.1: The laboratory test setup: A network analyzer, spectrum analyzer, NF meter and oscilloscope extract the discussed RF figures of merit. A logic analyzer forms the bridge between the RF front-end and the Matlab based GPS receiver back-end.
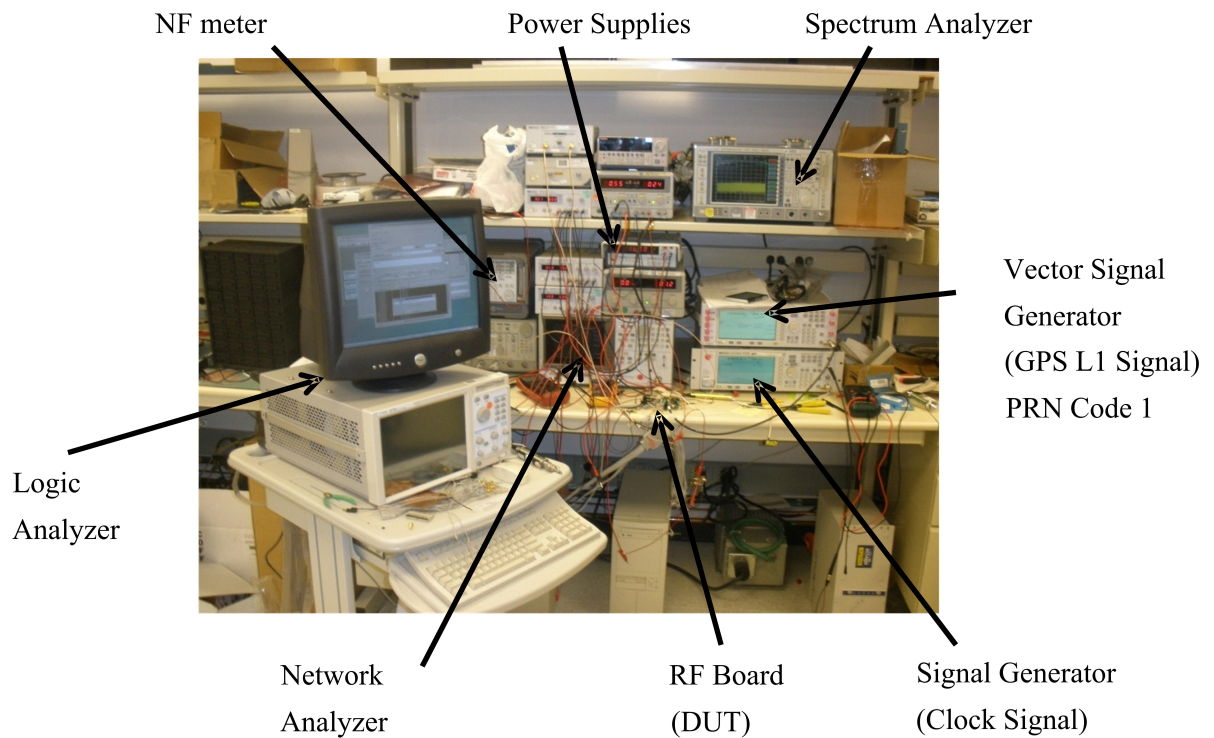
Figure 5.2: Laboratory photograph showing the measurement equipment and the DUT. A network analyzer, spectrum analyzer, NF meter and oscilloscope extract the discussed RF figures of merit. A conventional signal generator delivers the clock signal while a vector signal generator provides the PRN Code 1 modulated GPS L1 signal.

Logic Analyzer

Spectrum Analyzer
with GPS L1 C/A Code

Oscilloscope & NF meter   Network Analyzer   DUT
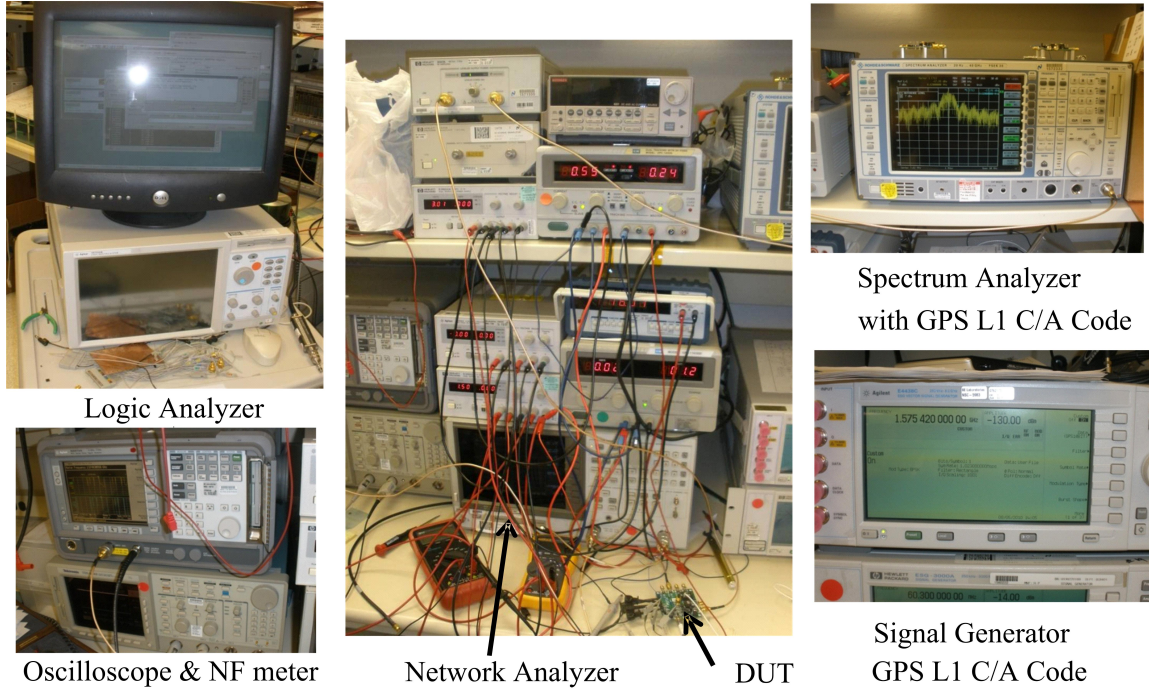
Signal Generator
GPS L1 C/A Code

Figure 5.3: Laboratory photograph showing the measurement equipment and the DUT.

Finally, the downconverted GPS IF signal is directly 1-bit quantized by the logic analyzer 16702B from Agilent and connected to the Matlab receiver back-end. Alternatively, to measure the harmonic content of the subsampled IF signal or to get a general impression of the signal, the IF output can be connected to a Tektronix oscilloscope or to the FSEK30 spectrum analyzer.

5.2   S-Parameter Measurements

As illustrated in Figure 5.1, the S-parameters of the three cascaded RF building blocks – namely the LNA, the CS amplifier and the RF filter – were measured by the network analyzer connected to the RF input and RF testport. The output instrumentation power from the network analyzer is set to the lowest possible power level ensuring that the RF filter is still operating in the linear region.
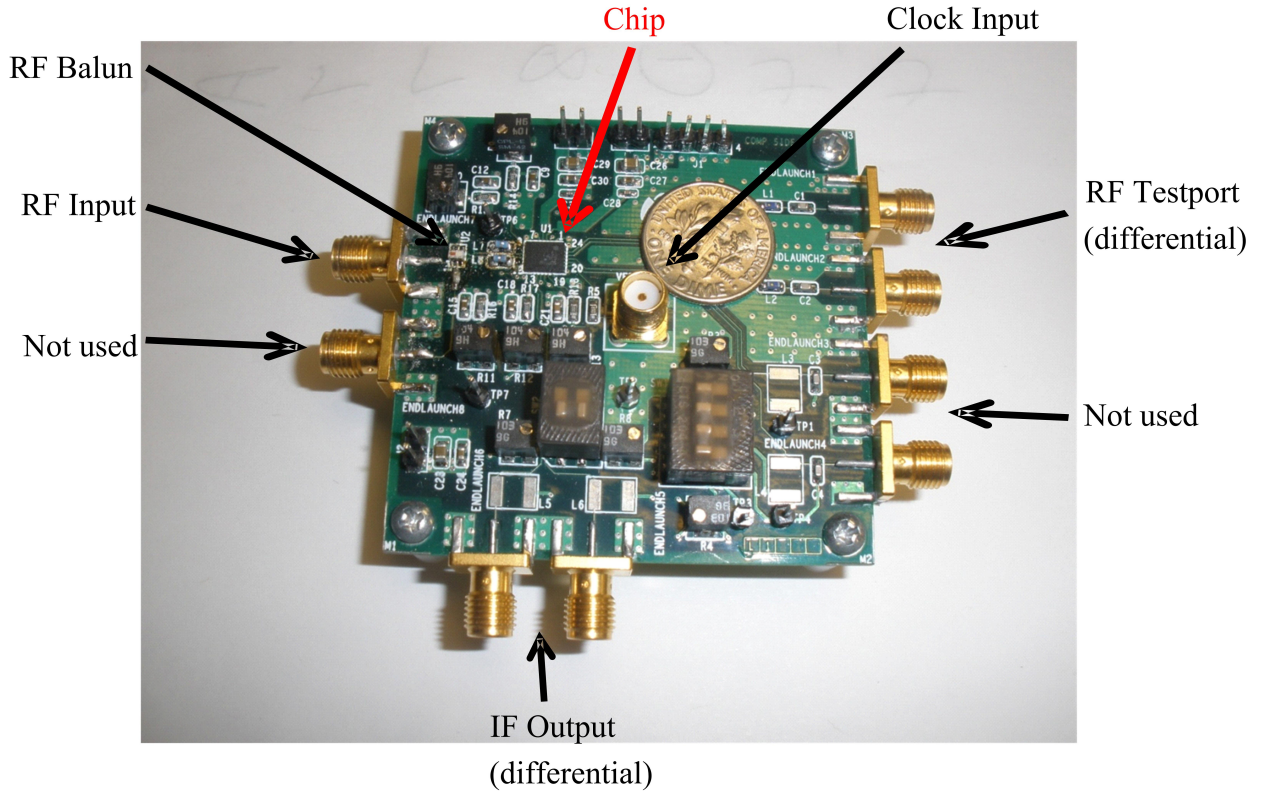
Figure 5.4: RF board with RF and IF ports and clock input.

The magnitude response of S_{21} is dominated by the narrowband RF filter characteristic and plotted into Figure 5.5 from 1325 MHz to 1825 MHz. The bandwidth of the magnitude response of DUT #1 and DUT #2 is 11 MHz corresponding to a Q-factor of roughly 130. The notch filter zeros are located at 1540 MHz and 1610 MHz; the double pole at the center frequency of 1575 MHz.

DUT #2 shows a power gain of 30 dB between the RF input and the RF testport while DUT #1 shows a power gain of only 26 dB. Note that the power gain measured at the 50 Ω RF testport is different from the simulated on-chip voltage gain reported in Figure 4.1. The RF filter output can be regarded as high impedance node at the RF center frequency. Hence, only little power is available from this node but the voltage can still be significant. The magnitude response of DUT #1 and DUT #2 is plotted into Figure 5.7 over an extended frequency range from 0.5 GHz to 3 GHz. The contours of the magnitude response of the LNA can be seen from Figure 5.7 above
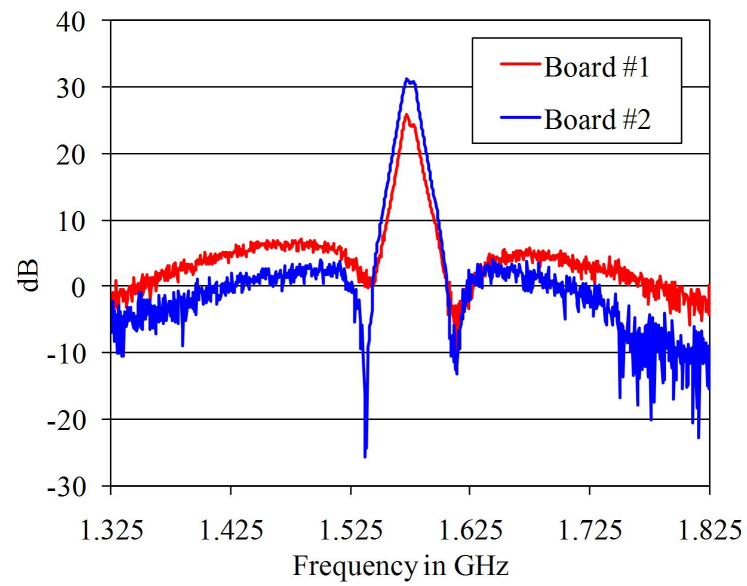
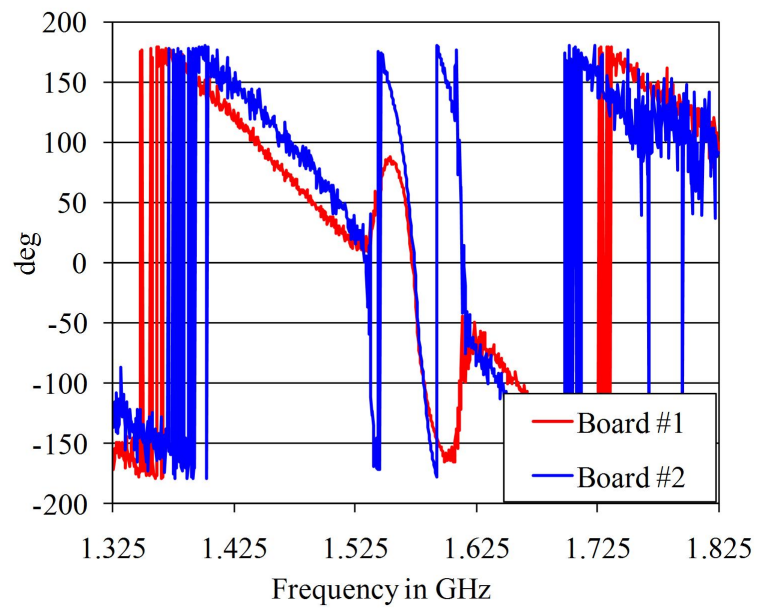Figure 5.5: Magnitude response of the RF filter
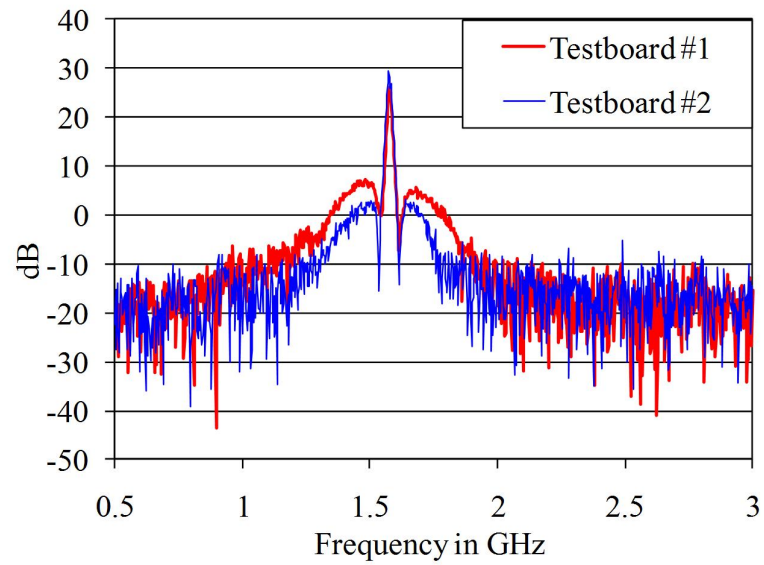

Figure 5.6: Phase response of the RF filter

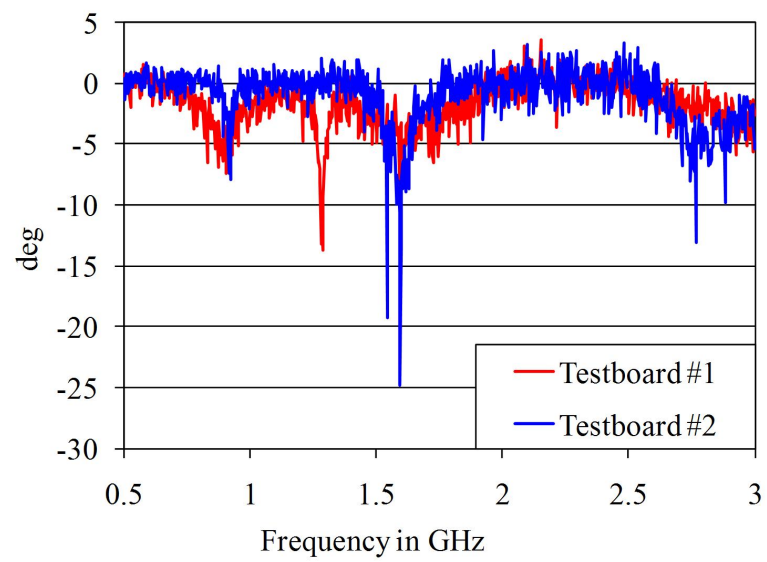Figure 5.7: Magnitude response of the RF filter over extended frequency range

Figure 5.8: Reflection coefficient of the RF filter

and below the notch frequencies of the RF filter characteristic. Above approximately 1.8 GHz and below approximately 1.2 GHz, the measured signal vanishes below the instrumentation noise floor.

The phase of S_{21} is plotted into Figure 5.6. The phase at 1575 MHz is sufficiently linear with a group delay variation of less than 4ns within the C/A code bandwidth. This is comparable to the group delay of SAW filters placed at the input of commercial GPS receivers [*Muller*, 1998]. The magnitude of S_{11} of the LNA is plotted into Figure 5.8: DUT #2 is well matched to 50 Ω showing an in-band return loss above 10 dB while DUT #1 is less well matched with an in-band return loss of 4 dB. This difference stems most likely from different board parasitics.

5.3   Noise Figure Measurements

The cascaded NF of the LNA, the CS amplifier and the RF filter was measured at the RF testport using the NF meter from Agilent. The NF is not affected by the RF buffer since enough gain is provided in the RF signal path. The NF is measured before the S/H stage and does not include any aliased noise from out-of-band noise sources. For comparison, the NF was also measured using the FSEK30 spectrum analyzer showing good agreement with the NF meter. Note, that the NFs in Section 5.3 and Section 5.4 do not include the 0.7 dB insertion loss of the external RF balun on the board in Figure 5.4.

The NF measured by the NF meter is plotted into Figure 5.9 versus frequency from 1.55 GHz to 1.60 GHz. The in-band NF of DUT #1 is about 3.2 dB while the in-band NF of DUT #2 is about 4.6 dB. The NF of DUT #1 is lower than the NF of DUT #2 even though the gain of the RF filter on DUT #2 is 4 dB higher. Obviously, the input impedance of DUT #1 is closer to the optimum noise impedance discussed by *Shaeffer and Lee*, [1997] than the input impedance of DUT #2.
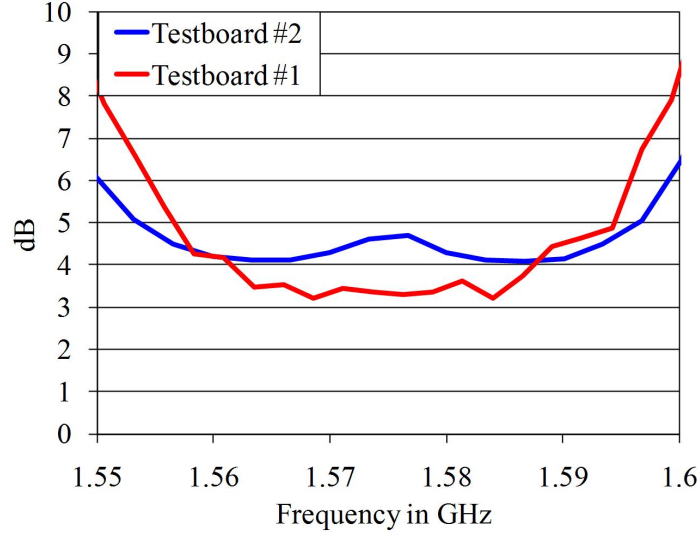
Figure 5.9: Cascaded NF of the LNA, the CS amplifier and the RF filter measured at the RF testport

5.4 Total Receiver Noise Figure

In this section, the total receiver NF at the output of the front-end is presented. Only the NF of DUT #1 is reported. The total receiver NF is measured after subsampling at the IF output of the receiver. The difference between the total receiver NF and the NF reported in Section 5.3 can be regarded as the increase in SNR due to aliasing from the S/H operation and ultimately, as the NF of the subsampling mixer.

Applying a 1575.42 GHz sinusoidal tone (GPS L1 frequency) to the RF input and the 60 MHz sinusoidal tone to the clock input, the SNR at the RF input can be measured by the spectrum analyzer and compared with the SNR of the 15.42 MHz tone at the IF output of the receiver. The ratio is the total receiver NF, which is plotted into Figure 5.10 as "NF at IF (after subsampling)". For comparison, the NF at the RF filter output from Section 5.3 (also measured by the spectrum analyzer) is plotted into Figure 5.10 as "NF at RF (before subsampling)". The RF and corresponding IF share the same value on the X-axis. For example, the GPS L1 signal located at a RF of 1575.42 MHz is downconverted to an IF of 15.42 MHz. The blue numbers on the
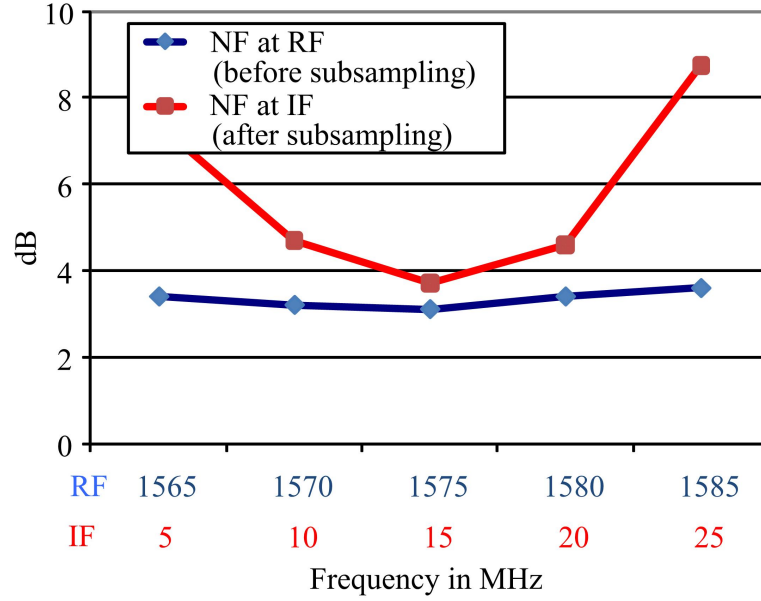
Figure 5.10: NF measured by a spectrum analyzer before subsampling at RF (blue curve and blue number on X-axis) and after subsampling at IF (red curve and red numbers on X-axis).

X-axis and blue curve in Figure 5.10 correspond to the RF while the red numbers and red curve correspond to the IF.

The total receiver NF after subsampling is 3.8 dB, about 0.6 dB higher than the NF at the output of the RF filter. Hence, the noise penalty from subsampling is less than 0.6 dB. This number can also be regarded as the NF of the subsampling mixer. The NF measurements were performed using both the HP ESG3000A signal generator and the crystal oscillator from Abracon as clock input. The measurements show good agreement. In fact, the NF measured using the crystal oscillator is less than 0.1 dB higher than the NF measured using the signal generator. The result hints that the aperture noise introduced by the crystal oscillator barely affects the receiver NF as predicted in Section 3.3.

5.5 Harmonics in the Signal Spectrum

In this section, the signal spectrum before and after subsampling is discussed. Again, a sinusoidal tone located at 1575 MHz is applied to the RF input and a 60 MHz sinusoidal signal to the clock input. The harmonic content of the RF and IF signal before and after the S/H stage is plotted into Figure 5.11 from 1525 MHz to 1625 MHz and from 1 MHz to 200 MHz. The RF signal and the corresponding downconverted IF signal are marked with an orange arrow. Aliases are marked with a turquoise arrow and clock harmonics with a green arrow.

The RF is 1575 MHz and the IF is 15 MHz. As expected, aliases can be found only in the IF output spectrum. Aliases are spaced $f_S/2 = 30$ MHz apart. Clock harmonics can be found both in the IF and RF spectrum. Clock harmonics in the RF spectrum arise from clock feedthrough into the RF signal path. Clock harmonics in the RF signal path end up as DC offset after aliasing and are not problematic for low IF architectures. The VGA made of AC coupled amplifier stages will cancel any DC offset from aliased clock harmonics. Figure 5.11 indicates how the NF measurements at the RF and IF are performed with the spectrum analyzer.

5.6 Receiver Linearity

The 1 dB compression point is plotted into Figure 5.12. The in-band 1 dB compression point is about -80 dBm at 1575 MHz. The out-of-band 1 dB compression point at 1400 MHz is about -30 dBm. Reduced in-band linearity can be tolerated for a GPS receiver with low bit quantization since jamming of the receiver back-end occurs at an in-band interference level as low as -110 dBm. Thus, the receiver is jammed already at signal levels significantly below the in-band compression. The out-of-band linearity is limited by the common source amplifier and could likely be improved.
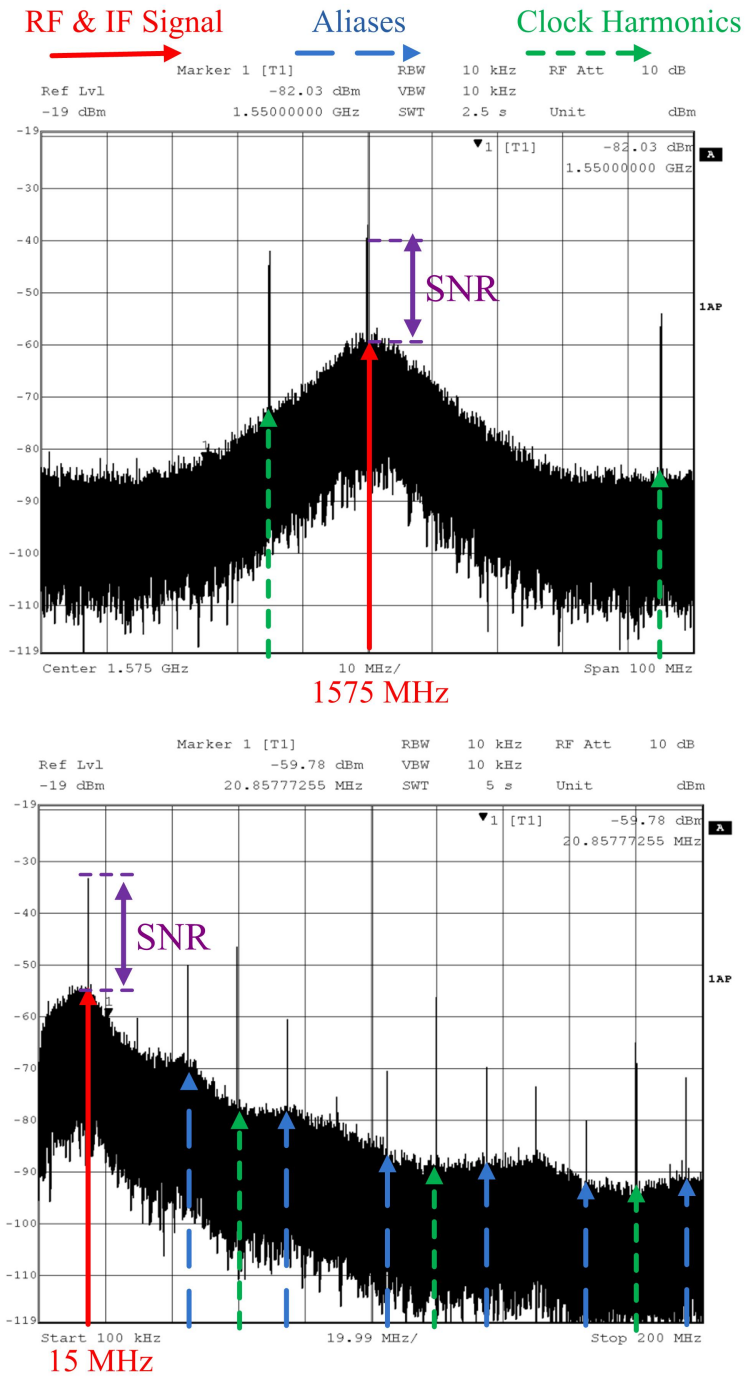
Figure 5.11: Spectral content at the buffer output before subsampling (top figure) and spectral content after subsampling at the IF output (bottom figure).
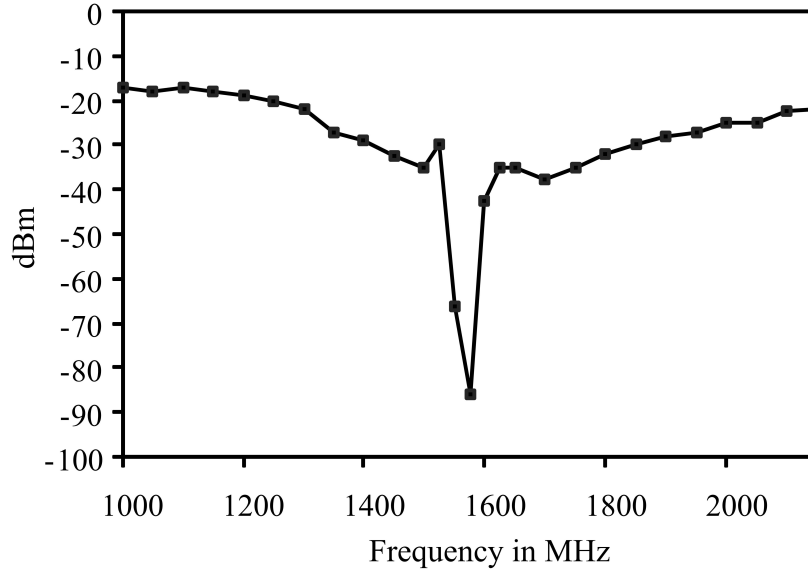
Figure 5.12: Receiver 1 dB compression point

5.7   Matlab GPS Receiver Back-end Results

The Matlab back-end GPS receiver was developed by *DeLorenzo*, [2005]. The back-end primarily extracts the navigation message modulated on the C/A code necessary for accurate computation of position and time. The GPS back-end receiver performs two signal processing steps: First, an acquisition step which determines whether the received 1-bit quantized data contains a valid GPS signal. Second, after successful acquisition of a valid signal the receiver switches into continuous tracking mode. During the acquisition phase, the software correlates the received data with the PRN sequences transmitted by different space vehicles. If a valid correlation is found, the received data contains a valid GPS signal and the software receiver switches into continuous signal tracking mode and extracts the navigation message modulated on the signal and the carrier-to-noise ratio C/N_0. As discussed in Section 2.3, the C/N_0 ratio is closely related to the SNR and defined as carrier power C divided by the noise power spectral density $N_0 = kT = -174$ dBm/Hz at ambient temperature. An

extensive review of the acquisition and tracking phase of a GPS back-end is beyond the scope of this dissertation.

To test the functionality of the front-end receiver, a valid GPS L1 signal generated with the Vector Signal Generator from Agilent is applied to the RF input. The signal generator modulates the GPS L1 carrier with the 1023 chips long PRN #1 code sequence (emitted by space vehicle 1). The signal contains no navigation message and the signal power is set to -130 dBm. This signal is downconverted to an IF of 15.42 MHz with the GPS receiver front-end using the 60 MHz clock. The signal at the IF output is 1-bit quantized by the logic analyzer 16702B from Agilent. The quantized data is fed into the Matlab back-end where it is correlated with different PRN sequences. As expected, a correlation match was found for PRN #1 code but not for any other PRN code during the acquisition phase.

After successful acquisition of PRN #1 code, the receiver went into tracking mode extracting the navigation message and the carrier to noise ratio C/N_0. The C/N_0 measured by the software receiver is 34.7 dBm/Hz. This number can be related to the NF measured in Section 5.4 in the following fashion. Since the signal input power is -130 dBm and $N_0 = kT = -174$ dBm/Hz, the carrier C/N_0 at the input of the receiver is 44 dBm/Hz. Hence, the C/N_0 measured by the receiver back-end is 9.3 dB lower. If corrected for the 2 dB degradation due to 1-bit quantization, the 0.7 dB from the external balun and 0.7 dB accounting for cable losses from the E4438C signal generator to the input of the receiver, the NF of the receiver front-end can be estimated to be 9.3 - 0.7 - 0.7 - 2 dB = 5.9 dB. This number is still 2 dB higher than the number measured in Section 5.4. This discrepancy was never successfully resolved. Possible explanations, however, include the non-ideal passband characteristics of the RF filter or the receiver transfer function resulting in additional correlation loss.

5.8 Summary

A performance summary with all relevant measured values of the GPS receiver front-end including power consumption and total receiver gain is given in Table 5.1.

Table 5.1: Performance summary of the GPS receiver

Supply Voltage	1.2 V
Total Power Consumption	9 mW
Power Consumption LNA	4.1 mW
Power Consumption Filter	1.6 mW
Noise Figure	3.8 dB
In-band input ref. 1dB Comp.	-80 dBm
Out-of-band input ref. 1dB Comp.	>-35 dBm
3 dB Frequency	12 MHz
Center Frequency	1575.42 MHz
Attenuation +/- 30 MHz from the Center Frequency	> 30 dB
Mid-band power gain	30 dB
Subsampling Frequency	60 MHz
Subsampling Ratio	26.25
Technology	130 nm BiCMOS
Die Area	1.9 mm^2

Chapter 6

Conclusion

This dissertation presented the development of an integrated subsampling GPS receiver front-end which was fabricated in a 130 nm BiCMOS process from National Semiconductor occupying 1x2 mm^2. Subsampling architectures historically suffer from high NFs, an obstacle that has limited their use to few applications. To achieve low NFs deemed suitable for GPS applications, a narrowband RF filter is implemented to filter out unwanted out-of-band noise, mostly from thermal sources.

The filter was designed using inductors with high quality factor Q available in National's BiCMOS process. The process enables high-Q inductors by the availability of two thick top metal layers. Using a patterned ground shield, the inductor Q can be as high as 20. Moderate Q-enhancement was applied to the inductors to achieve a RF filter with less than 20 MHz bandwidth at GHz frequencies. The RF filter uses a special LCC image rejection series parallel resonant tank. The input impedance of the LCC tank exhibits a closely spaced zero-pole doublet creating a steep transition region between the zero and the pole. In the presented RF filter, the LCC tank is applied to a differential cascode amplifier stage with inductive load. The resulting transfer function exhibits a notch at 1540 MHz and at 1610 MHz. The 3 dB bandwidth of the filter is less than 20 MHz. The center frequency is at the GPS L1 frequency of 1575.42 MHz. The notch at 1540 MHz and 1610 MHz attenuates noise and interference close to the center frequency which is not attenuated in conventional subsampling architectures, a main factor leading to historically elevated NFs.

A higher level of Q-enhancement leads to a reduced in-band linearity. Out-of-band linearity is barely affected by Q-enhancement. Reduced in-band linearity can be tolerated for a GPS receiver with low-bit quantization since jamming of the receiver back-end occurs at an in-band interference level as low as –110 dBm. Thus, the receiver is jammed already at signal levels significantly below the in-band compression. The out-of-band linearity is limited by the common source amplifier and could likely be improved in a future version of the IC.

The performance of the receiver is comparable to state-of-the-art GPS and direct RF subsampling receivers. The total power consumption is 9 mW, the supply voltage is 1.2 V. The NF before subsampling is 3.2 dB at the filter output. After subsampling, the total receiver NF is 3.8 dB, to our knowledge, the lowest ever reported NF for a subsampling architecture in an integrated circuit making it suitable for GPS applications.

6.1 Future Work

In the presence of mismatch and process variations, post-fabrication trimming of the LCC resonant tanks is necessary. A tuning step to properly set the center frequency of the RF filter is required and an additional tuning step is necessary to set the quality factor of the spiral inductors.

Overall, the number of tuning steps is limited to two. For simplicity and proof of concept of the subsampling receiver, an off-chip tuning scheme is applied to accurately set the RF filter response. In a future version of the IC, a digital signal processing unit could be integrated using an on-chip auto-tuning scheme to set the RF magnitude response. Such an approach would be especially tempting in a deep sub-micron process where a digital signal processing unit can be implemented at significantly reduced cost.

Appendix A

Modified Friis Equation

The analysis from Chapter 3.2 is extended to clarify on the mathematical derivation of the subsampling mixer. The noise factor F of a subsampling mixer can be calculated with the well-known formula:

$$F = \frac{\text{Total Output Noise Power}}{\text{Total Output Noise Power due to the Source}} = \frac{P_{\text{tot}}}{P_{\text{S,tot}}} \qquad \text{(A.1)}$$

The total available output noise power of the subsampling mixer, evaluated at IF, can be found by summing over all aliased noise components. As depicted in Figure A.1, let $S(f)$ be the available noise power spectral density at the input of the S/H stage, $S_{\text{Alias}}(f)$ the available noise power spectral density at the output of the S/H stage, and $S_{\text{s}}(f)$ the available noise power spectral density from the source at the input of the subsampling mixer. $S_q(f)$ is the available noise power spectral density *added* by the q-th filter stage. $G_q(f)$ the available power gain of the of the q-th filter stage. The S/H stage is assumed to be noiseless since all input referred noise of the S/H stage can be included in $S_N(f)$. According to Figure A.1, $S(f)$ can be found to be

$$S(f) = \prod_{k=1}^{N} G_k(f)S_{\text{S}}(f) + \prod_{k=2}^{N} G_k(f)S_1(f) + \dots$$
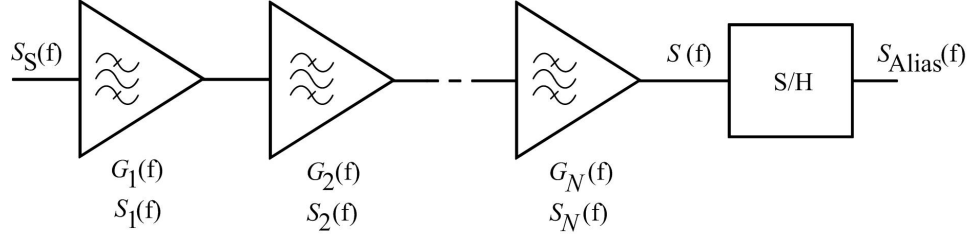
$$\text{(A.2)}$$

$$+ G_N(f)S_{N-1}(f) + S_N(f)$$

Figure A.1: Multistage subsampling mixer. The available noise power spectral densities are given by $S_S(f)$, $S_1(f)$, ... , $S_n(f)$, $S(f)$ and $S_{Alias}(f)$. The available power gain per stage is given by $G_1(f)$, ... , $G_N(f)$. The S/H stage assumed to be noiseless.

Using the same frequency definition as in Chapter 3.2, the available power spectral density $S_{Alias}(f_{IF})$ after sampling can be found by summing over all aliased noise components according to (3.2):

$$S_{Alias}(f_{IF}) \propto \sum_{m=0}^{\infty} S(f_m)df \tag{A.3}$$

Note, that the factor f_S in (3.2) was omitted in (A.3) as we are only interested in the noise factor ratio. In (A.3) ideal impulse sampling is assumed. If the S/H stage is zero-order hold, then a sinc-distortion term will have to be included in (A.3). The total output noise power P_{tot} at the output of the S/H stage within an IF signal bandwidth of $2B$ is given by

$$P_{tot} = \int_{f_{IF}-B}^{f_{IF}+B} S_{Alias}(f)df \propto \sum_{m=0}^{\infty} \int_{f_m-B}^{f_m+B} S(f)df \tag{A.4}$$

and includes aliased out-of-band noise. The output noise power due to the source within an IF bandwidth of $2B$ is given by

$$P_{S,tot} \propto \int_{f_{2n}-B}^{f_{2n}+B} \prod_{k=1}^{N} G_k(f)S_S(f)\,df \tag{A.5}$$

and does not include aliased out-of-band noise. The component $m = 2n$ in (A.4) represents the in-band noise, while the other values of m represent the aliased out-of-band noise. The noise factor F of the subsampling mixer can be computed by inserting (A.2), (A.4), (A.5) in (A.1). To simplify the mathematical derivation some definitions are necessary. First, the cascaded available gain $G_{pq}(f)$ from stage p to stage q, normalized by the available gain at frequency f_{2n}, is defined. $G_{pq}(f)$ is given by the relationship

$$G_{pq}(f) = \prod_{k=p}^{q} \frac{G_k(f)}{G_k} \qquad 1 \le p \le q \le N \tag{A.6}$$

$G_{pq}(f)$ can be regarded as the transfer function of the filter characteristic from stage q to p, normalized to 0 dB at the center frequency f_{2n}. The noise factor F of the subsampling mixer can be computed from (A.1), (A.2), (A.4) and (A.5)

$$F = \sum_{m=0}^{\infty} \frac{\int_{f_m-B}^{f_m+B} \prod_{k=1}^{N} G_k(f) S_\mathrm{S}(f) df}{\int_{f_{2n}-B}^{f_{2n}+B} \prod_{k=1}^{N} G_k(f)\, S_\mathrm{S}(f)\, df} + \sum_{m=0}^{\infty} \frac{\int_{f_m-B}^{f_m+B} \prod_{k=2}^{N} G_k(f) S_1(f) df}{\int_{f_{2n}-B}^{f_{2n}+B} \prod_{k=1}^{N} G_k(f)\, S_\mathrm{S}(f)\, df} + ..$$

$$+ \sum_{m=0}^{\infty} \frac{\int_{f_m-B}^{f_m+B} G_N(f) S_{N-1}(f) df}{\int_{f_{2n}-B}^{f_{2n}+B} \prod_{k=1}^{N} G_k(f)\, S_\mathrm{S}(f)\, df} + \sum_{m=0}^{\infty} \frac{\int_{f_m-B}^{f_m+B} S_N(f) df}{\int_{f_{2n}-B}^{f_{2n}+B} \prod_{k=1}^{N} G_k(f)\, S_\mathrm{S}(f)\, df} \tag{A.7}$$

which can be simplified using (A.6)

$$F = \sum_{m=0}^{\infty} \frac{\int_{f_m-B}^{f_m+B} G_{1N}(f) S_\mathrm{S}(f) df}{\int_{f_{2n}-B}^{f_{2n}+B} G_{1N}(f)\, S_\mathrm{S}(f)\, df} + \frac{1}{G_1} \sum_{m=0}^{\infty} \frac{\int_{f_m-B}^{f_m+B} G_{2N}(f) S_1(f) df}{\int_{f_{2n}-B}^{f_{2n}+B} G_{1N}(f)\, S_\mathrm{S}(f)\, df} + ..$$

$$+ \frac{1}{G_1 G_2 \cdot\cdot\, G_{N-1}} \sum_{m=0}^{\infty} \frac{\int_{f_m-B}^{f_m+B} G_{NN}(f) S_{N-1}(f) df}{\int_{f_{2n}-B}^{f_{2n}+B} G_{1N}(f)\, S_\mathrm{S}(f)\, df} \tag{A.8}$$

$$+ \frac{1}{G_1 G_2 \cdot\cdot\, G_{N-1} G_N} \sum_{m=0}^{\infty} \frac{\int_{f_m-B}^{f_m+B} S_N(f) df}{\int_{f_{2n}-B}^{f_{2n}+B} G_{1N}(f)\, S_\mathrm{S}(f)\, df}$$

The R-coefficients are defined as

$$R_{0N}^m = \frac{\int_{f_m-B}^{f_m+B} G_{1N}(f) \frac{S_S(f)}{S_S} df}{\int_{f_{2n}-B}^{f_{2n}+B} G_{1N}(f) \frac{S_S(f)}{S_S} df} \tag{A.9}$$

and

$$R_{qN}^m = \frac{\int_{f_m-B}^{f_m+B} G_{(q+1)N}(f) \frac{S_q(f)}{S_q} df}{\int_{f_{2n}-B}^{f_{2n}+B} G_{1N}(f) \frac{S_S(f)}{S_S} df}; \quad q = 1, ..., N-1 \tag{A.10}$$

and

$$R_{NN}^m = \frac{\int_{f_m-B}^{f_m+B} \frac{S_N(f)}{S_N} df}{\int_{f_{2n}-B}^{f_{2n}+B} G_{1N}(f) \frac{S_S(f)}{S_S} df} \tag{A.11}$$

Using (A.9), (A.10) and (A.11) the noise factor F can be significantly simplified

$$F = \sum_{m=0}^{\infty} R_{0N}^m + \frac{S_1}{G_1 S_S} \sum_{m=0}^{\infty} R_{1N}^m + \frac{S_2}{G_1 G_2 S_S} \sum_{m=0}^{\infty} R_{2N}^m + ...$$

$$+ \frac{S_{N-1}}{G_1 G_2 \cdots G_{N-1} S_S} \sum_{m=0}^{\infty} R_{N-1N}^m + \frac{S_N}{G_1 G_2 \cdots G_{N-1} G_N S_S} \sum_{m=0}^{\infty} R_{NN}^m \tag{A.12}$$

Finally, using (2.11) for the spot noise factor of the q-th stage

$$F_q = \frac{S_S G_q + S_q}{S_S G_q} \tag{A.13}$$

equation (A.12) can be rewritten as

$$F = S_{0N} + (F_1 - 1)S_{1N} + \frac{(F_2 - 1)}{G_1} S_{2N} + .. + \frac{(F_N - 1)}{\prod_{k=1}^{N-1} G_k} S_{NN} \tag{A.14}$$

where the aliasing coefficients S_{qN} are given by

$$S_{qN} = \sum_{m=0}^{\infty} R_{qN}^m \tag{A.15}$$

Bibliography

Ahmed, H., DeVries, C., Mason, R., RF, Q-enhanced band-pass filters in standard 0.18μm CMOS with direct digital tuning, *IEEE international symposium on circuits and systems*, vol. 1, pp. 25–28, May 2003.

Akos, D. M., Stockmaster, M., Tsui, J. B. Y., Caschera, J., Direct bandpass sampling of multiple distinct RF signals, *IEEE Transactions on Communications*, vol. 47, July 1999.

Akos, D., Tsui, J., Design and Implementation of a Direct Digitization GPS Receiver Front-End, *IEEE Transactions on Microwave Theory and Techniques*, vol. 44, pp. 2334–2339, Dec. 1996.

Akos, D., et al, A prototyping platform for Multi-Frequency GNSS receivers, *Institute of Navigation's GPS/GNSS Meeting*, Sep. 2003.

Arkesteijn, V. J., Klumperink, E. A. M., and Nauta, B., Jitter requirements of the sampling clock in software radio receivers, *IEEE Trans. Circuits Syst. II, Exp. Briefs*, vol. 53, pp. 90–94, Feb. 2006.

Behjou, N., Larsen, T., Hoegdal, M., Design of a Simultaneous Multi-Band RF Sub-Sampling Receiver, *IEEE MTT-S*, pp. 5–8, June 2008

Chang, H., Presampling Filtering, Sampling and Quantization Effects on Digital

Matched Filter Performance, *Proceedings of the International Telemetering Conference*, pp. 889–915, 1982

Cheng, K.W., Natarajan, K., Allstot, D., A 7.2mW Quadrature GPS Receiver in 0.13m CMOS, *ISSCC Dig. Tech. Papers*, pp. 422–423, Feb 2009.

Clein, D., Advanced Techniques for Building-Block Interconnect Layout Design, Chapter 6 in *CMOS IC Layout: Concepts, Methodologies and Tools*, 1st ed. Oxford: Elsevier, 2000.

DeVries, C. and Mason, R., A 0.18μm CMOS, high Q-enhanced bandpass filter with direct digital tuning, *IEEE Custom Integrated Circuits Conference*, pp. 279–282, May 2002.

De Lorenzo, D., GPS C/A-code Software Receiver in Matlab Signal Acquisition by FFT Processing, GPS Research Laboratory, Stanford, CA, Nov. 2005

DeVries., C., and Mason, R., A 0.18-μm CMOS 900-MHz Receiver front-end using RF Q-enhanced filters, *Int. Symp. Circuits Syst. (ISCAS)*, pp. IV-325–IV-328, 2004.

DeVries, C., Mason, R., Subsampling Architecture for Low Power Receivers, *IEEE Transactions on Circuits and Systems*, vol. 55, Apr. 2008.

Eichenberger, C., Guggenbuhl, W., Dummy transistor compensation of analog MOS switches, *IEEE Journal of Solid State Circuits*, vol. 24, no. 4, pp. 1143-1146, Aug. 1989.

Fontana, R. D., Cheung, W., Stansell, T. A., The New L2 Civil Signal, *Institute of Navigation GPS-2001*, Salt Lake City, UT, Sept 2001.

Friis, H. T., Noise Figures of Radio Receivers, *Proceedings of the Institute of Radio Engineers (IRE)*, vol. 32, no. 7, pp. 419–422, July, 1944. (Correction, vol. 32, no. 12, p. 729, December, 1944.)

Gebreselasie, E.G., et al., Electrically Programmable Fuses for Analog and Mixed Signal Applications in Silicon Germanium BiCMOS Technologies, *IEEE Bipolar/BiCMOS Circuits and Technology Meeting*, pp. 238–241, May 2007.

Georgescu, B., Finvers, I.G., Ghannouchi, F., 2 GHz Q-Enhanced Active Filter With Low Passband Distortion and High Dynamic Range, *IEEE Journal of Solid State Circuits*, vol. 41, no. 9, pp. 2029–2039, Sep. 2006.

Gonzalez, G., *Microwave Transistor Amplifiers*, 2nd ed., Prentice-Hall, Upper Saddle River, New Jersey, 1997.

Gramegna, G., et al., A 56-mW 23-mm^2 Single-Chip 180-nm CMOS GPS Receiver with 27.2mW 4.1mm^2 Radio, *IEEE J. Solid-State Circuits*, vol. 41, pp. 540–551, Mar. 2006.

IS-GPS-200D, Interface Specifications IS-GPS-200D, Revision D, *Navstar GPS Space Segment / Navigation User Interfaces*, Navstar GPS Joint Program Office, 2004

Issler, J-L, et al, Galileo Frequency and Signal Design, *GPS World*, June 2003.

Jakonis, D., Svensson, C., A 1.6 GHz Downconversion Sampling Mixer in CMOS, *International Symposium on Circuits and Systems*, vol. 1, pp. I-725–I-728, May 2003.

Johnson, J. B. , Thermal Agitation of Electricity in Conductors, Phys. Rev., v.32, July 1928, pp. 97–109.

Ko, J., Kim, J., Cho, S., Lee, K., A 19mW 2.6mm^2 L1/L2 dual-band CMOS GPS

Receiver, *IEEE J. Solid-State Circuits*, vol. 40, pp. 1414–1425, July 2005.

Kuhn, W. B., Yanduru, N. K. and Wyszynski, S., Q-enhanced LC bandpass filters for integrated wireless applications, *IEEE Trans. Microw. Theory Tech.*, vol. 46, pp. 2577–2586, Dec. 1998.

Lam, C.S., A Review of the Recent Development of MEMS and Crystal Oscillators and their Impacts on the Frequency Control Products Industry, *IEEE IUS Ultrasonics Symposium*, pp. 694–704, Nov. 2008.

Lee, T.H., *The Design of CMOS Radio-Frequency Integrated Circuits*, 2nd ed. New York: Cambridge University Press, 1998.

Liscidini, A., Mazzanti, A., Tonietto, R., Vandi, L., Andreani, P.; Castello, R., A 5.4mW GPS CMOS Quadrature Front-End Based on a Single-Stage LNA-Mixer-VCO, *ISSCC Dig. Tech. Papers*, pp. 472-473, Feb. 2006.

Liu, H., and Karsilayan, A.I., Frequency and Q tuning of active-LC filters, *Proceedings of the IEEE Midwest Symposium of Circuits and Systems*, vol. 2, Aug. 2002.

Misra, P., and Enge, P., *Global Positioning System: Signals, Measurements, and Performance*, 2nd ed., Ganga-Jamuna Press, 2006.

Muller, T., Performance Degradation in GPS-Receivers caused by Group Delay Variations of SAW-Filters, *IEEE MTT-S International* Microwave Symposium Digest, Baltimore, 7–12 Jun 1998

Nakaska, J.K. and Haslett, J.W., 2 GHz Automatically Tuned Q-Enhanced CMOS Bandpass Filter, *IEEE/MTT-S International Microwave Symposium*, pp. 1599 –1602, June 2007.

Parkinson, B.W., Spilker, J.J., Enge, P., Penina, A., *Global Positioning System: Theory and Applications*, 1st ed., Washington, DC, American Institute of Aeronautics and Astronautics, 1996.

Pekau, H. and Haslett, J.W., Cascaded noise figure calculations for radio receiver circuits with noise-aliasing properties, *IEE Proc.-Circuits Devices Syst.*, Vol. 153, Dec. 2006.

Pekau, H., and Haslett, J., A 2.4 GHz CMOS sub-sampling mixer with integrated filtering, *IEEE Journal of Solid State Circuits*, vol. 40, pp. 2159–2166, Nov. 2005.

Pekau, H., Haslett, J., A 0.18μm CMOS 2.1GHz Sub-sampling Receiver Front End with Fully Integrated Second- and Fourth-Order Q-Enhanced Filters, *IEEE International Symposium on Circuits and Systems (ISCAS)*, pp. 3103–3106, May 2007.

Pozar, D., *Microwave Engineering*, 2nd ed., Wiley, 1998.

Prades, C.F., Rubio, J.A.F., Multi-frequency GPS/Galileo receiver design using direct RF sampling and antenna arrays, *Sensor Array and Multichannel Signal Processing Workshop Proceedings*, pp. 475–479, 2004.

Psiaki, M. L., Akos, D. M., and Thor, J. A comparison of 'Direct RF Sampling' and 'Down-Covert and Sampling' GNSS receiver architectures, *ION GPS 2003 Proceedings*, pp. 1941–1952, Sept. 2003.

Psiaki, M. L., Powell, S. P., Jung, H., and Kintner, P. M., Design and Practical Implementation of Multi-frequency RF Front Ends Using Direct RF Sampling, *IEEE Trans. on Microwave Theory and Techniques*, vol. 53, pp. 3082–3089, Oct. 2005.

Ru, Z., Klumperink, E. A. M., Saavedra, C. E. and Nauta, B., A 300800 MHz tunable filter and linearized LNA applied in a low-noise harmonic- rejection RF-sampling

receiver, *IEEE J. Solid-State Circuits*, vol. 45, no. 5, pp. 967–978, May 2010.

Russo, A., *CGSIC International Subcommittee European Meeting*, Toulouse, France, May 2008.

Schottky, W.,Über spontane Stromschwankungen in verschiedenen Elektrizitätsleitern, *Annalen der Physik*, v.57, 1918, pp. 541–67.

Shaeffer, D., and Lee, T.H.,A 1.5-V, 1.5-GHz CMOS Low Noise Amplifier, *IEEE Journal Of Solid-State Circuits*, vol.32, pp. 745–759, May 1997.

Shaeffer, D.,K., The design and implementation of low-power CMOS radio receivers, Ph.D. Dissertation, Department of Electrical Engineering, Stanford University, Stanford, CA, 1999.

Shen, D., Hwang, C. and Lusignan, B., A 900-MHz RF front-end with integrated discrete-time filtering, *IEEE J. Solid-State Circuits*, vol. 31, pp. 1945–1954, Dec. 1996.

Staszewski, R.B., et al., A 24 mm^2 quad-band single-chip GSM radio with transmitter calibration in 90 nm digital CMOS, *ISSCC Dig. Tech. Papers*, pp. 208–607, Feb. 2008.

Teichmann, J., Burger, K., Hasche, W., Herrfurth, J., Tischner, G., One Time Programming (OTP) with Zener Diodes in CMOS Processes, *33rd Conference on European Solid-State Device Research, ESSDERC*, pp. 433–436, 2003.

Thor, J., Akos, D., A Direct RF Sampling Multifrequency GPS Receiver, *IEEE Position Location and Navigation Symposium*, April 2002.

Torre, V., Conta, M., Chokkalingam, R., Cusmai, G., Rossi, P., Svelto, R., A 20mw

3.24mm^2 Fully Integrated GPS Radio for Cell Phones, *ISSCC Dig. Tech. Papers*, pp. 474–475, Feb. 2006.

Tsui, J. B. Y., and Akos, D., Comparison of direct and downconverted digitization in GPS receiver front end designs, *IEEE MU-S Int. Microwave Symp.*, San Francisco, CA, June 1996.

Vallese, A. Bevilacqua, A., Sandner, C., Tiebout, M., Gerosa, A., Neviani, A. Analysis and Design of an Integrated Notch Filter for the Rejection of Interference in UWB Systems, *IEEE Journal of Solid State Circuits*, vol. 44, no. 2, pp. 331–343, Feb. 2009.

Van den Homberg, J. A. T. M., A Universal 0.03-mm^2 One-Pin Crystal Oscillator in CMOS, *IEEE Journal of Solid-State Circuits*, vol. 34, no. 7, July 1999.

Van Dierendonck, A. J., Hegarty, C., Scales, W., Ericson, S., Signal Specification for the Future GPS Civil Signal at L5, *International Association of Institutes of Navigation 25th World Congress*, San Diego, CA, June 2000.

Weaver, D.K., A Third Method of Generation and Detection of Single-Sideband Signals, *Proc. IRE*, Dec. 1956, pp.1703–1705

Wei, W., Huang, X., Tan, F., Rong, Q., Study and Estimation of Crystal Oscillator, *International Conference on Communications, Circuits and Systems Proceedings*, vol.1, pp. 289–292, 2006.

Wiser, R.,Tunable Bandpass RF Filters, Ph.D. Dissertation, Department of Electrical Engineering, Stanford University, Stanford, CA, 2008.

Yuce, M. R., and Liu, W., Design and implementation of a multirate subsampling front-end in software radio systems, *IEEE Radio and Wireless Conf.*, pp. 529–532, 2004.